# Developing Thermally Robust Aerogels for Next-Generation Linear Concentrated Receivers

by

Zachary Berquist

A dissertation submitted in partial fulfillment
of the requirement for the degree of
Doctor of Philosophy
(Chemical Engineering)
in the University of Michigan
2022

Doctoral Committee:

Associate Professor Andrej Lenert, Chair
Associate Professor Neil Dasgupta
Professor Nicholas Kotov
Professor Anish Tuteja

Zachary J. Berquist
zjber@umich.edu
ORCID iD: 0000-0002-4838-8644

© Zachary J. Berquist 2022

# Dedication

To my parents, Rebecca and James Berquist

To my siblings,

Rachel, Nicholas, Michael, and Melissa

# Acknowledgements

Pursuing a PhD has been the greatest decision I have ever made, but it was not possible without the support and presence of so many people in my life. I would like to recognize some of the most important people who have helped me complete my degree. I would not be in this position without contributions from them, and many others who are not listed here.

First and foremost, I would like to thank my advisor, Professor Andrej Lenert, who accepted me as a part of his second cohort in his lab. Andrej's mentorship is invaluable, and I know he enabled me to become the best researcher I can be. I cannot underestimate Andrej's constant availability, as he met with me every week throughout my entire PhD, and early on he would come down to the lab to provide feedback on experimental techniques. If I ever needed help, he was always available in his office. Lastly, Andrej's support of my career decisions has meant everything to me. I was able to take time away from my dissertation work to work three years as a part of the department's peer mentoring program, attend the UNFCCC conference in Spain, and intern at Sandia National Labs. His support and mentorship will guide how I approach the rest of my career.

Next, I would like to thank the first members of the Lenert Research Group: Hannah, Tobias, Alexander, and Sean. It was just us five for my first two years of working in the lab, and I will never forget how much fun it was to come into work. You all set such a great precedent for lab culture. I also want to thank Bosun who joined the lab during my third year. You fit in so well and brought such a positive energy to lab, and only enhanced our lab culture. In my last year, I was lucky enough to welcome Andrés, Areefa, and Carissa to the lab. The Lenert Lab only continued to thrive with your inclusion to the lab. The Lenert Lab family has grown and become a more enjoyable experience with every passing year, and I can't wait to see what everyone accomplishes in their journeys. Specifically, Andrés, who I have had the opportunity to mentor

in my last year, you have made tremendous strides, and I know the aerogel project is great hands. Lastly, thank you to all the undergraduate students I have had the pleasure of working with. I want to specifically thank Kevin and Sean. You both made such amazing contributions during your time. I'm excited to see how your research careers take off in graduate school.

In addition to the Lenert Research Group, I need to thank my collaborators in Mechanical Engineering: Andrew Gayle and Professor Neil Dasgupta. I could not have asked for better collaborators. To Andrew, you were always timely, productive, and insightful, and I will miss working together. I know you have and will accomplish amazing things in your career. And Neil, your mentorship has been vitally important to my growth as a researcher.

Finally, on a personal note, I would like to thank all my friends whose relationships helped me persevere through graduate school. I have met lots of amazing people, many of which are now lifetime friends. To Alex, Sean, Marshall, Patrick, Jacques, Connor, Emily, Alain, Mackenzie, Danielle, Anna, Rachel, Zixuan, Misché, Katey, and others – thank you for doing the impossible: making my time at Michigan even better than my time at Penn State. And of course, thank you to Chrissy, who has specifically made the last few years the best of my life. Thank you for being so supportive when I have needed it.

To my parents, Rebecca and James, thank you for providing me the opportunity to pursue my career goals. Your support is the main reason I was able to attend graduate school in the first place. Thank you for always trying to visit me and making it a priority to put family first. And of course, thank you to my brothers Michael and Nicholas, and especially my twin sister Rachel. It means so much to know I have had your support over the years.

# Contents

# List of Figures

# List of Tables

# Abstract

Concentrating solar thermal (CST) is a promising method to produce high temperature heat without the combustion of fossil fuels. The heat generated from concentrated sunlight can be used for several processes such as driving a thermal power cycle for electricity generation or providing heat for industrial processes. The solar receiver is one of the key components of the CST system. Its role is to convert incident sunlight into heat. A high performing solar receiver absorbs sunlight and limits thermal losses. One proposed solar receiver design is to use a transparent insulating material (TIM) which behaves in a way very similar to the way the greenhouse effect keeps the Earth warm. Sunlight transmits through the TIM and heats the absorber, but the insulative properties of the TIM keep the thermal losses low. The state-of-the-art TIMs are silica aerogels because of their high solar transmittance and high thermal resistance. Although high performing at low temperatures (<300°C), silica aerogels suffer from large radiative losses and thermal degradation at higher temperatures.

In this thesis, I address these issues by (i) incorporating selectively absorbing plasmonic nanoparticles into silica aerogels and (ii) demonstrating improved thermal stability through atomic layer deposition (ALD) surface modification. The incorporation of plasmonic nanoparticles, specifically indium tin oxide, reduces heat losses by half, while only reducing transmittance by ~20%. This increases the *spectral selectivity* of the aerogels, a primary figure of merit. Reducing the agglomeration of ITO nanoparticles within the aerogel matrix can improve selectivity further. Overall, this is a promising method to selectively increase the infrared absorption of silica aerogels and increase their performance at high temperatures. Second, the ALD surface modification increases the thermal stability of the silica aerogels by increasing the viscosity of the aerogel particles, which slows viscous sintering. Impressively, this ALD modification only reduces transparency by 1% due to the uniform and conformal nature of the coating. The resulting

refractory aerogel demonstrates a path forward for developing thermally stable, transparent aerogels for next-generation CST plants.

To address a knowledge gap regarding the performance of aerogels at high temperatures, I developed a comprehensive numerical heat-transfer model that simulates combined conductive and radiative heat transfer with varying pressure in a linear receiver. The findings from this modeling work suggest that despite the improvements from transparent conducting oxide nanoparticles, the performance of silica aerogels is lower than that of selective absorbers at lower temperatures. At 700°C, however, silica aerogels outperform selective absorbers. This work proposes methods to improve the performance of silica aerogels in high temperature linear receivers, such as developing selective absorbers that are designed for use with silica aerogels.

Lastly, this thesis describes efforts to develop a 1-m long linear receiver integrated with refractory aerogels. The results show that an aerogel-based receiver significantly reduces the heat losses, and a detailed technoeconomic analysis estimates the cost of CST plants using aerogel receivers. The results of the analysis show that the refractory aerogel receiver has the potential to deliver inexpensive carbon-neutral, high temperature heat compared to other approaches. The pathways highlighted throughout this thesis may enable aerogel receivers to surpass selective absorbers as the preferred linear receiver design.

# Chapter 1 : Introduction

Concentrating solar thermal (CST) is a promising solution to provide carbon-free baseload electricity generation and high-temperature process heat. Highly reflective mirrors focus sunlight onto a solar receiver which converts the sunlight into thermal energy. This heat can then be used to power a variety of processes including thermal power cycles, industrial processes, and water heating (Figure 1.1).[1] The receiver's performance is dependent on how much of the incident sunlight is converted into heat. As receivers get hotter, more of the absorbed sunlight is lost as heat due to thermal re-radiation. It is therefore critical for the receiver to maximize solar absorptance and minimize thermal radiative losses. The next generation of CST plants are expected to exceed 800°C for two reasons. The first is to power supercritical $CO_2$ power cycles which are potentially more efficient and cheaper than traditional steam Rankine cycles.[2] The second reason is such high temperatures can provide heat to energy-intensive processes used in the chemical industry.[3] At these temperatures, however, the thermal radiative losses from the receiver increase dramatically since radiative power increases with temperature to the fourth power ($Q_{rad} \propto T^4$).

There are two prominent designs for CST plants: solar power towers (SPTs) and parabolic trough collectors (PTCs). SPTs circumvent this issue of high thermal losses by using thousands of mirrors to focus sunlight onto a central receiver. By focusing so much sunlight onto a solar receiver, the thermal losses only constitute a small fraction of the incident sunlight. However, SPTs have significant capital costs and require large installations with power demands >10 MW. They also have low optical efficiencies because it is difficult to focus mirrors as far as a mile away onto a central receiver. PTCs, on the other hand, have a simpler, 1-dimensional design with relatively low solar concentration ratios. The lower concentration ratio makes it more difficult to reach higher temperatures, but they are more modular, capable of supplying powers as low as 100 kW, and have higher optical efficiencies as the solar receiver is only ~1 m from the

mirror. If PTCs can reduce thermal losses enough to efficiently convert low concentrations of sunlight into 700°C+ heat, they can provide modular and inexpensive heating demands for next-generation CST.

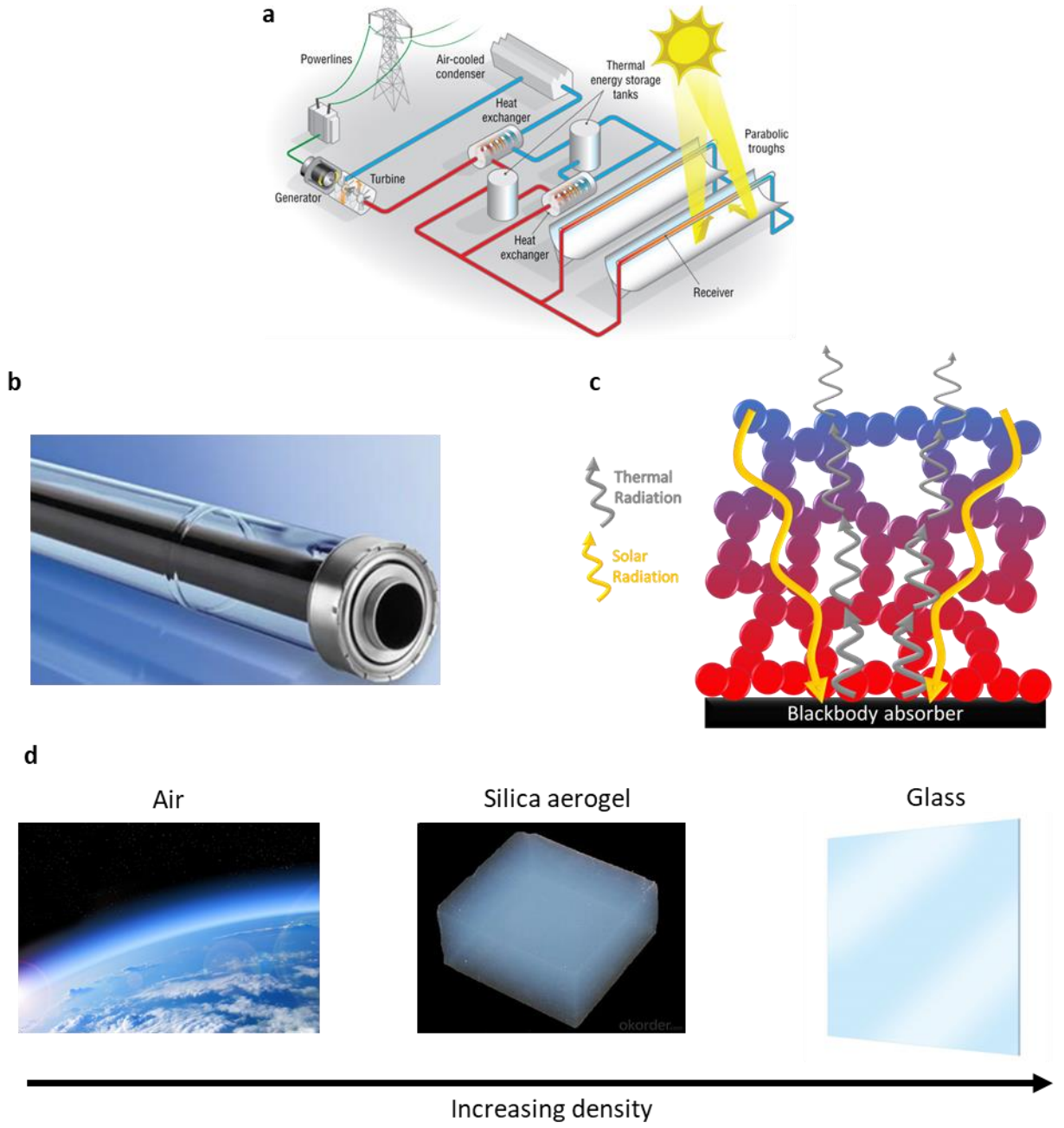


Figure 1.1. Overview of TIMs in concentrated solar thermal. (a) Diagram of a concentrated solar thermal plant. Concentrated sunlight heats up linear receivers, and the heat is stored in thermal batteries. The heat can be used to drive a power cycle or provide heat to industrial processes. (b) Traditional linear receivers are evacuated and use selective absorbers to reduce thermal radiative losses. (c) TIMs enable high temperature heat by mimicking the greenhouse effect. TIMs transmit sunlight and restrict heat losses by forcing thermal radiation to undergo absorption and re-emission numerous times. (d) TIMs can range anywhere from air to a transparent glass. Silica aerogels are an intermediate that maintains high transparency while also having the lowest conductivity of any known solid-state material.

Current PTC plants use evacuated receivers, which consist of a steel tube inside a glass tube. To reduce thermal losses, the steel tubes are coated with a solar selective surface, and it operates under high vacuum (< $10^{-5}$ bar) to eliminate losses from internal convection. Also known as selective absorbers (SAs), the steel coatings are designed to have high solar absorptance and low thermal emittance. Although this receiver design operates efficiently at moderate temperatures (< 500°C), the performance drops at temperatures > 600°C. As currently constructed, SAs are not an option in 3rd generation CST.

Table 1.1 Common nomenclature

| | | | |
|---|---|---|---|
| $C$ | Solar concentration ratio | $\eta$ | Efficiency |
| $c$ | Speed of light | $\lambda$ | Thermal conductivity (mW/m/K) |
| $F$ | Mean temperature adjustment factor | $\upsilon$ | Wavenumber ($m^{-1}$) |
| $G_s$ | AM1.5D incident solar power (1,000 $W/m^2$) | $\rho$ | Density ($kg/m^3$) |
| $h$ | Convective heat transfer coefficient ($W/m^2$) | $\sigma$ | Stefan-Boltzmann constant |
| $l$ | Thickness of aerogel (m) | $\tau$ | Transmittance |
| $k_B$ | Boltzmann constant | $\omega$ | Radial frequency of light |
| $n$ | Refractive index | $\Gamma$ | Greenhouse selectivity |
| $Q$ | Heat flux ($kW/m^2$) | **Subscripts** | |
| $W$ | Work ($kW/m^2$) | $abs$ | Absorber |
| **Greek letters** | | $e$ | Electron |
| $\alpha$ | Solar absorptance | $eff$ | Effective |
| $\beta$ | Thermal extinction coefficient ($m^{-1}$) | $loss$ | Thermal losses |
| $\gamma$ | Damping coefficient (s) | $max$ | Maximum |
| $\varepsilon$ | Emissivity | $p$ | Plasmon |
| $\epsilon$ | Permittivity | | |

A possible alternative to SAs is transparent insulating materials, or TIMs, which insulate solar receivers in a manner nearly identical to the greenhouse effect (Figure 1.1b). TIMs transmit sunlight to heat broadband absorbers which are much more stable than SAs. TIMs then limit thermal losses by forcing radiation emitted from the absorber to undergo numerous absorption and re-emission events that occur at progressively lower temperatures. Additionally, TIMs inherently have low thermal conductivities, which in theory allows them to operate efficiently at ambient pressure, which could further reduce the costs of the CST plant. The properties that dictate the heat losses through a TIM are its thermal conductivity, which should be as low as possible, and its infrared absorption, which should be as high as possible. Additionally,

TIMs must also remain highly transparent to sunlight to maintain intense heating of the solar absorber. This radiative selectivity – *i.e.*, transparent to sunlight but opaque to thermal radiation – defines the concept of *spectral selectivity*.

The requirements of a TIM limit the number of candidate materials. A TIM can be anything from a glass window to air (Figure 1.1c). In between these two extremes are silica aerogels, which are the most promising TIM to date. They maintain the high transparency of air and glass but have a thermal conductivity as low as still air. In addition, silica aerogels have high infrared absorption throughout the infrared, which reduces thermal radiative losses. The goal of this chapter is to provide a fundamental understanding of TIMs in solar receivers, which can then provide a basis for the necessary improvements in silica aerogels to enable an efficient, high-temperature PTC receiver.

## 1.1 Figure of Merit

There are two main energy pathways in a receiver that dictate its performance: the sunlight absorbed and the heat losses out. Receivers perform better when they capture more sunlight and lose less heat. Any figure of merit should incorporate these two phenomena. Since radiation is the dominant mode of energy transfer in a solar receiver, a common term for a performance metric is "spectral selectivity", which is effectively a ratio of a receiver's ability to absorb sunlight to its ability to suppress thermal losses. This metric has traditionally been used for selective absorbers, but it is easily applied to TIMs. First, this section provides a rationale for spectral selectivity as a figure of merit, and it then provides a new framework to predict receiver performance using the selectivity. Lastly, the chapter ends with a comprehensive discussion to estimate the apparent thermal emittance of a TIM using the Rosseland approximation.

## 1.2 Theoretical Efficiency Limit of a Solar Receiver

The useful work a solar receiver can provide is the difference between how much sunlight is absorbed and how much heat is lost back to the environment (Equation 1.1):

$$W = Q_{absorbed} - Q_{loss} \tag{1.1}$$

The amount of incident sunlight is a function of the solar concentration ratio, $C$, and the incident solar power, $G_s$, which is a standard set to the AM1.5D incident solar power of 1,000 W/m$^2$. Not all the incident

solar power is absorbed because of transmission losses from TIMs or imperfect absorption of the solar absorber. Therefore, the amount of work that is extracted from a solar receiver is defined in Equation 1.2:

$$W = \alpha\tau * CG_s - Q_{loss} \tag{1.2}$$

Lastly, the efficiency of a solar receiver is defined as the amount of work extracted divided by the total incident solar power, thus leading to the definition of receiver efficiency in Equation 1.3:

$$\eta = \alpha\tau - \frac{Q_{loss}}{CG_s} \tag{1.3}$$

If convective and conductive thermal losses are assumed to be negligible, then there is a radiative limit to the efficiency of a solar receiver defined here as the maximum radiative efficiency (MRE). The MRE is always less than unity because the solar and thermal emission spectra overlap. It is therefore impossible to have perfect solar collection and zero thermal radiative losses within the framework of a wavelength-selective receiver. A perfectly selective TIM or SA can maximize the receiver efficiency by choosing wavelengths to prioritize either solar collection or thermal resistance. For example, an ideal TIM paired with a blackbody absorber is perfectly transparent ($\tau$=1) for all wavelengths where the solar incident power exceeds the blackbody emission, and infinitely opaque ($\tau$=0) everywhere else (Figure 1.2). Analogously, an ideal SA is perfectly absorptive ($\varepsilon$=1) and reflective ($\varepsilon$=0), respectively. The locations of these selective regions depend on the temperature of the absorber and the concentration ratio since the solar spectrum is discontinuous.

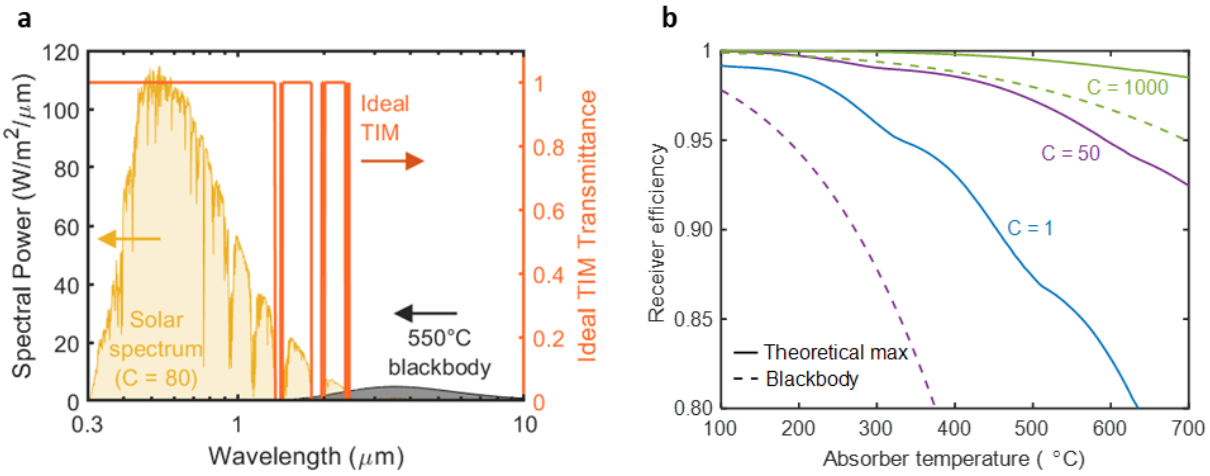


Figure 1.2. Performance of perfect TIMs. (a) The ideal transmittance spectrum of a TIM is equal to 1 whenever the solar intensity exceeds the blackbody emission, and equal to 0 (infinite absorptance) for the reverse case. (b) Maximum receiver efficiency in the radiative limit (i.e., ignoring conduction and convection).

Figure 1.2 shows the dependence of the MRE on the operating temperature and concentration ratio. As the concentration increases, the MRE approaches unity. It is important to note that there is a physical maximum to the concentration ratio of ~46,000 due to thermodynamic constraints.[4] Additionally, at lower operating temperatures, where there is less overlap between the solar and emission spectra, the solar receiver can achieve higher theoretical efficiencies.

## 1.3 Spectral Selectivity in the Radiative Limit

Researchers have long used a figure of merit called spectral selectivity which is the ratio of the solar absorptance to the weighted emissivity, $\varepsilon$, of an SA:[5,6]

$$\Gamma = \frac{\alpha}{\varepsilon} \tag{1.4}$$

Here $\Gamma$ is defined as *spectral selectivity*, and it is generalized to include TIMs. Unlike SAs, TIMs are defined by their solar transmittance and thermal losses. Therefore, for TIMs, $\alpha = \tau$, and the emissivity of the TIM is the *apparent* emissivity, $\varepsilon_{app}$. For simplicity, TIMs are assumed to be used with a blackbody absorber ($\alpha$=1) and SAs are assumed to have no transparent insulation ($\tau$=1), which makes the two properties analogous. The apparent emittance is the ratio of heat losses to the maximum heat losses for a blackbody at a given temperature:

$$\varepsilon_{app} = \frac{Q_{loss}}{\sigma(T^4 - T_\infty^4)} \tag{1.5}$$

where $\sigma$ is the Stefan-Boltzmann constant and $T_\infty$ is the ambient temperature. Equation 1.5 shows that heat losses through a TIM are directly proportional to its apparent emissivity. As discussed in the previous section, the high infrared absorption of a TIM drives the mechanism that lowers heat losses. The apparent emissivity is then inversely related to its infrared absorption, $\beta$ (see **1.4 Estimating the Thermal Resistance of Real TIMs**). Equation 1.6 also defines a relative temperature, $\Phi$:

$$\Phi = \frac{\sigma(T^4 - T_\infty^4)}{CG_s} \approx \frac{\sigma T^4}{CG_s} \tag{1.6}$$

The approximation above is valid for $T^4 \gg T_\infty^4$, which is common in CST. The following equations convert the definition of receiver efficiency into non-dimensional relationships:

$$\eta = \alpha - \varepsilon\Phi \tag{1.7a}$$

$$\eta = \alpha\left(1 - \frac{\Phi}{\Gamma}\right) \tag{1.7b}$$

Equation 1.7a shows that receiver efficiency decreases linearly with increasing emissivity of a TIM or SA. By factoring out $\varepsilon$, Equation 1.7b shows that the receiver efficiency is also a function of the spectral selectivity. Lastly, the maximum temperature of a receiver is the point at which the efficiency is equal to zero, which is also known as the stagnant fluid temperature or stagnation temperature. By setting $\eta = 0$, Equation 2.8 shows a simple relationship between the relative stagnation temperature and $\Gamma$:

$$\Phi_{max} = \Gamma \tag{1.8}$$

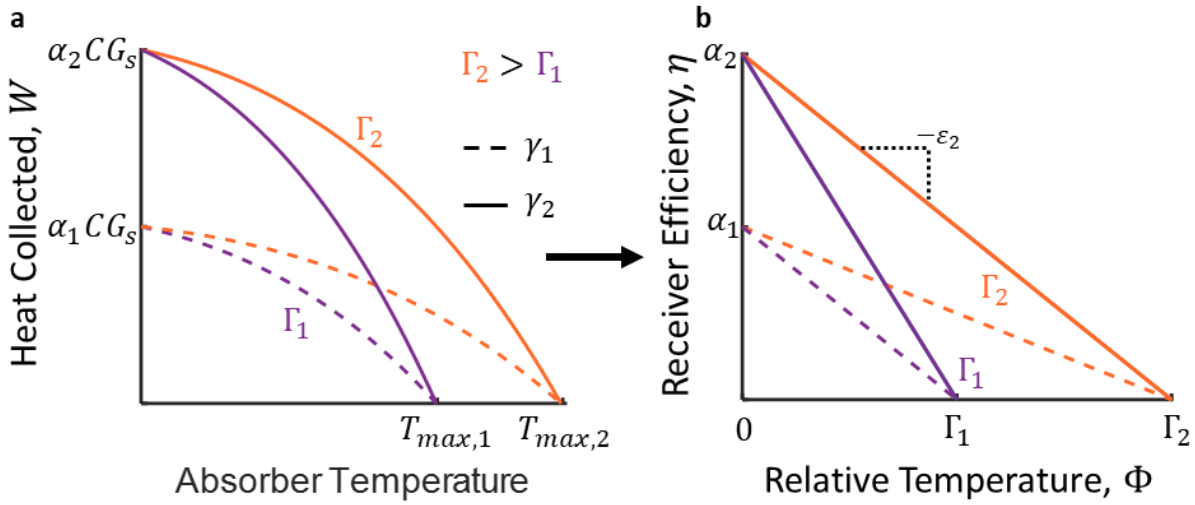


Figure 1.3. Utility of greenhouse selectivity. (a) Heat collected as a function of absorber surface temperature. The maximum heat collected occurs when the absorber temperature is equal to the ambient temperature, and the maximum achievable absorber temperature occurs when the efficiency of the receiver is equal to 0. (b) Receiver efficiency as a function of dimensionless temperature, $\boldsymbol{\Phi}$. Using greenhouse selectivity simplifies the relationship between performance and temperature because the dependence becomes linear. The maximum temperature in the radiative limit is simply the product of the solar concentration ratio and the greenhouse selectivity of the TIM, $\boldsymbol{\Gamma}$.

This framework simplifies the analysis of a material's efficiency at any condition. Typically, the relationship between heat collected and absorber temperature is a quartic relationship. Using this framework, the performance of a receiver is simplified to a linear relationship between the solar absorption and relative temperature (Figure 1.3). For example, the receiver efficiency reaches its maximum efficiency at ambient temperature where $\Phi$ is 0, but as the dimensionless temperature increases, the efficiency follows a straight line between $\alpha$ and $\Gamma$. Conveniently, the slope of this line is simply -$\varepsilon$ (see Equation 1.7a).

### 1.3.1 Designing More Selective TIMs

Equation 1.9 presents a slightly different parameter called the thermal resistance of a receiver, $R$:

$$R = 1 - \varepsilon \tag{1.9}$$

which creates a slightly different definition for the efficiency of a receiver:

$$\eta = \alpha - (1 - R)\Phi \tag{1.10}$$

To increase the efficiency of a receiver, it is critical to increase the thermal resistance without sacrificing solar absorption. Any methods to increase thermal resistance, such as increasing the thickness of an aerogel, will decrease $\alpha$. The exact value of this tradeoff (i.e., how much $\alpha$ can decrease per unit increase in $R$), changes based on the conditions per Equation 1.11:

$$\frac{\Delta R}{\Delta \alpha} \geq \frac{1}{\Phi} \tag{1.11}$$

where $\Delta R$ is the change in thermal resistance and $\Delta \alpha$ is the change in the solar absorption. Figure 1.3 shows this in more detail where contour lines of constant efficiency are plotted for varying values of $\alpha$ and $R$ at two different conditions. The equation for each of these lines is given by 1.10, or explicitly in the standard y=mx+b form as:

$$\alpha = -\Phi R + (\eta + \Phi) \tag{1.12}$$

The negative slope of the contour lines is thus equal to the relative temperature $\Phi$, meaning that at higher temperatures and lower concentration ratios, the slopes become steeper. For example, at a temperature of 700°C, the slope of the contour lines has a slope of -1 when the concentration ratio is 50, meaning that $R$ must increase more than $\alpha$ decreases to increase the efficiency of the receiver. Lastly, for reference, Figure 1.4 includes regions in the top right that are physically impossible to reach given the constraints discussed in **1.2 Theoretical Efficiency Limit of a Solar Receiver**.

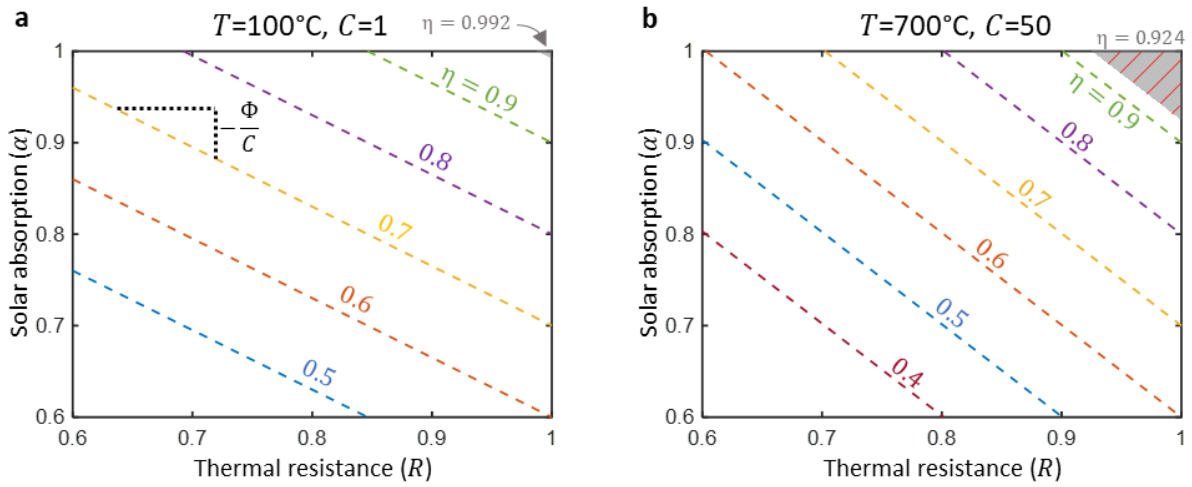


Figure 1.4. Efficiency contour lines for varying values of $\alpha$ and $R$. (a) $T_{abs}$ = 100°C and $C$ = 1. The slope of the contour lines is equal to $-\Phi$ (refer to Equation 2.10). (b) $T_{abs}$ = 700°C and $C$ = 50.

### 1.3.2. Measuring the Spectral Selectivity of TIMs

The term apparent emissivity describes a TIM because an SA with the same emissivity will have the same heat losses, which makes it a convenient method to compare the two technologies. Whereas the emissivity of SAs is commonly measured with Fourier transform infrared (FTIR) spectroscopy, the effective emissivity of a TIM is determined with a heat loss measurement (Equation 1.5). There are a few ways to measure or estimate the heat losses of an aerogel sample. The simplest is to use rigorous heat transfer modeling (Chapter 5). Experimentally, there are both dark (**3.2.2 Experimental Demonstration of *PEGS***) and on-sun measurements.[7,8] On-sun testing also enables a direct measurement of the selectivity of a TIM by measuring the maximum temperature the aerogel can reach. Otherwise, the transmittance of the TIM is simply measured using UV-Vis-NIR spectroscopy with an integrating sphere.

## 1.4 Estimating the Thermal Resistance of Real TIMs

As shown previously, an ideal TIM is one with infinite absorption in the infrared, but for real materials, it is impossible to achieve that. However, the absorption coefficients of real materials can be used to estimate the radiative heat losses through the TIM using the Rosseland Approximation:

$$Q_{loss}^{TIM} \cong Q_{Rosseland} = \frac{16\sigma \bar{T}_{eff}^3}{3\beta}\left(\frac{T_{abs} - T_\infty}{l}\right) \tag{1.13}$$

where $\bar{T}_{eff}$ is the mean temperature of the TIM, $\sigma$ is the Stefan-Boltzmann constant, $T_{abs}$ is the temperature of the absorber, $T_\infty$ is the temperature of the cold sink, $\beta$ is the thermal absorption coefficient (or Rosseland-mean extinction coefficient), and $l$ is the thickness of the TIM. Together, $\beta l$ forms the thermal opacity of a material.

There are two main challenges with the Rosseland Approximation. The first is determining the thermal opacity, $\beta l$, of a given material, and the second is that it is only accurate for large thermal opacities ($\beta l > 3$). For materials with relatively low thermal opacities, the Rosseland Approximation greatly overestimates heat losses because the Rosseland heat flux is inversely proportional to the thermal opacity (Equation 1.13). As the optical thickness approaches zero, the heat flux approaches infinity. This is further highlighted by the definition of the Rosseland-mean absorption coefficient in Equation 1.14:

$$\frac{1}{\beta_R} = \frac{\pi}{4\sigma T_{eff}^3}\int_0^\infty \frac{2h^2c^3\upsilon^4 \exp\left(\frac{hc\upsilon}{k_B T_{eff}}\right)}{\beta k_B T_{eff}^2 \left(\exp\left(\frac{hc\upsilon}{k_B T_{eff}}\right) - 1\right)^2} \tag{1.14}$$

where $h$ is the Planck constant, $c$ is the speed of light, $\upsilon$ is the wavenumber, $\beta$ is the spectral absorption coefficient, and $k_B$ is the Boltzmann constant. Similar to the calculation of the heat flux, the calculation here for $\beta_R$ is overly weighted by the optically thin regions of a material due to the inverse nature of the calculation. For silica aerogels, this places too much emphasis on the infrared transparency window (2 – 5 μm), and ultimately underestimates the mean absorption coefficient. For example, the Rosseland approximation predicts a heat flux of ~300 kW/m$^2$ for a 2 mm thick, 170 kg/m$^3$ dense aerogel on a 700°C absorber, which is impossible since that is 6x greater than the blackbody limit (50.8 kW/m$^2$). One option to address this issue was proposed by Tsakiris and Eidmann.[9] They suggest using the Planck-mean

absorption coefficient for optically-thin materials, but they do not identify when it is accurate to do so. Furthermore, while the Rosseland-mean absorption coefficient overly emphasizes optically thin regions, the Planck-mean absorption coefficient overly emphasizes optically thick regions (Figure 1.5a). As a result, neither is an effective method to determine a spectrally-weighted absorption coefficient.

One promising method is to use an effective mean temperature that is a function of the thermal opacity of a material ($T_{eff} = f[\beta l]$):

$$T_{eff} = \frac{T_{abs} + T_{\infty}}{2} * F \tag{1.15}$$

where $F$ is dependent on the thermal opacity of the material. The primary limitation of this method is that there is no universal definition of $F$, but rather it is also a function of the hot and cold boundary conditions. As a test case, the following section analyzes a relevant situation for concentrated solar power which is a hot side absorber temperature of 700°C and an ambient cold temperature boundary of 25°C. To determine a relationship for $F$, an exact method, such as the radiative transfer equation (RTE), first determines the actual heat losses of gray materials with various optical thicknesses. Details about the RTE are provided in Michael Modest's *Radiative Heat Transfer* and in **5.3 Modeling Mesoporous Silica**.[10] Once the exact values of the heat fluxes are obtained, the effective temperature is back calculated using Equation 1.13. A best function for the best fit with respect to thermal opacity is provided in Figure 1.5b.

This method not only enables the use of the Rosseland Approximation for optical thicknesses that are below ~3, but it also enables a more accurate calculation of the Rosseland-weighted absorption coefficient by using the adjusted mean-temperature in Equation 1.14. An iterative process to find a more accurate Rosseland-weighted absorption coefficient is as follows:

1. Calculate the Rosseland-mean absorption coefficient with the arithmetic mean of the temperature of the two boundaries of interest.

2. Calculate a new effective mean temperature using a correlation, such as the one provided in Figure 1.5b.
3. Calculate a new Rosseland-mean absorption coefficient with the updated $T_{eff}$.
4. Repeat steps 2-3 until it converges (Figure 1.5c).
5. Determine the heat flux with the converged values of $F$ and $\beta l_{adjusted}$
6. Calculate $\beta l_{eff}$ by back-calculating for $\beta l$ and substituting the heat flux from step 5 and the arithmetic mean into Equation 4.

It is necessary to ultimately find the effective Rosseland thermal opacity by using the predicted heat flux and arithmetic mean temperature since Equation 1.13 is normalized by the arithmetic mean temperature. For example, Figure 1.5c shows that the adjusted Rosseland optical thickness for a 170 kg/m$^3$ dense, 5 mm thick silica aerogel is 0.84, but this value is only relevant if using the adjusted mean temperature (Figure 1.5d). Using the predicted heat flux value of 32.1 kW/m$^2$, the properties of the aerogel can be generalized by using the *effective* thermal opacity. This is done in Step 6, which back-calculates for $\beta l$ using the predicted heat flux from Step 5. Therefore, a more accurate, and universal mean-absorption coefficient of 1.63 is determined which can be used to estimate the heat fluxes more accurately for any absorber temperature. To finally calculate the greenhouse selectivity, the last property required is the solar-weighted transmittance which can be determined through experimental UV-Vis measurements or a variety of predictive methods.

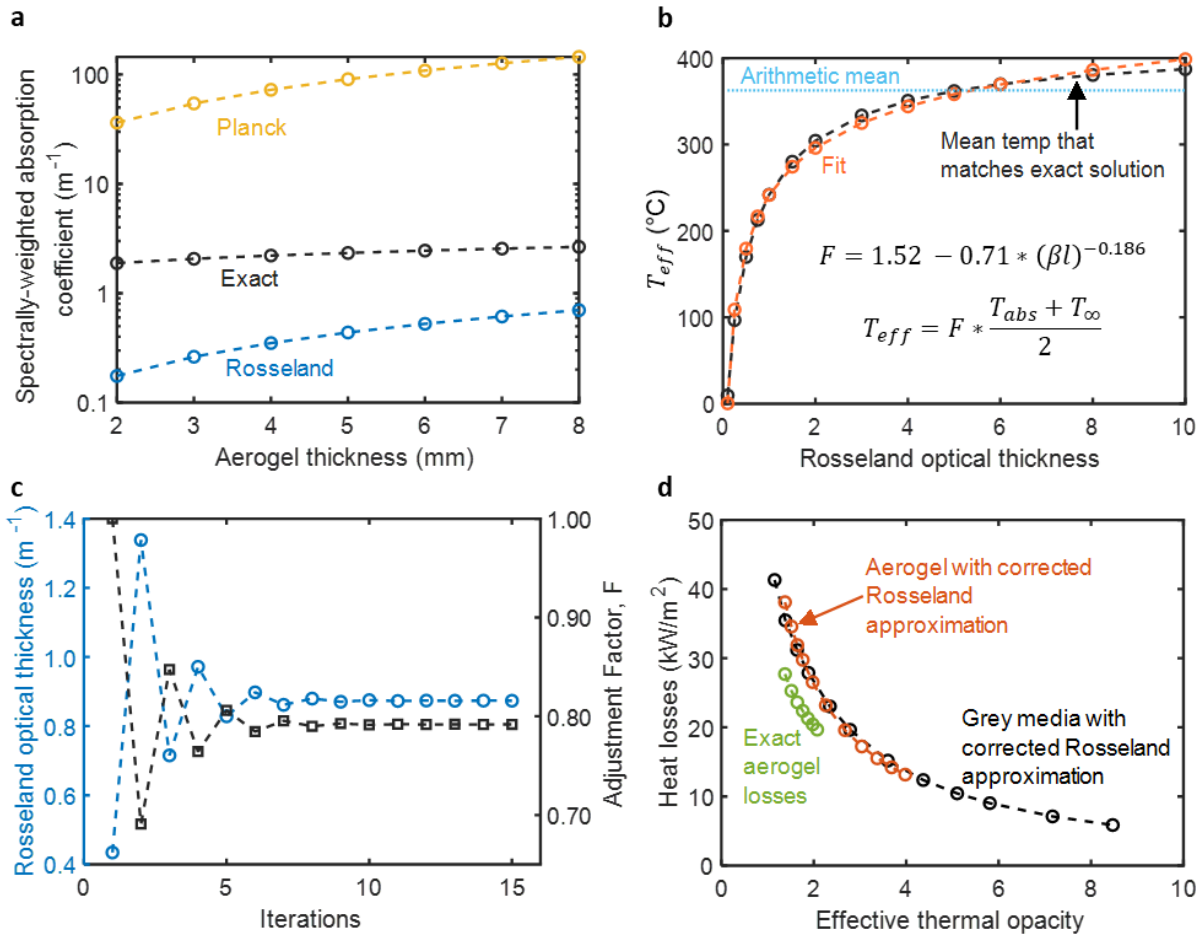


Figure 1.5. Modified Rosseland approximation. (a) Spectrally-weighted extinction coefficients for the Rosseland and Planck methods. The Exact spectrally-weighted extinction coefficient is the value that provides the exact heat losses for the Rosseland approximation. (b) Fitted relationship for adjusting the effective mean temperature to provide an accurate estimation of heat losses for the Rosseland approximation. For lower optical thicknesses, a lower mean temperature is necessary to offset the inverse relationship between heat flux and optical thickness. (c) Calculating the Rosseland optical thickness by updating the effective mean temperature with the relationship from (b) creates a more accurate optical thickness for the estimation of heat losses. (d) The heat losses with the modified Rosseland approximation enable a significantly more accurate estimation of heat losses. Even the modified procedure outlined here still carries a ~20% error. The extinction coefficients of real materials vary by orders of magnitude, and it is difficult to capture those effects in a single extinction coefficient.

Although this method significantly improves the utility of the selectivity, it does not perfectly estimate the heat losses of real materials. Figure 1.5d shows that the 'exact' heat losses of aerogels using methods such as the RTE are lower than the heat losses predicted by the adjusted Rosseland approximation by roughly 20%. This is due to the primary limitation of using a spectrally weighted absorption coefficient. Even with the steps taken here, a single absorption coefficient fails to accurately capture the effects of an absorption coefficient that changes by more than 4 orders of magnitude throughout the relevant radiation spectrum

(~1 – 100 μm). Therefore, this method can be used to roughly approximate the greenhouse selectivity of a medium, although additional experimental or rigorous computational methods are recommended.

## 1.5 Thesis Outline

This thesis begins with **Chapter 1** which reviews the fundamentals that determine the performance of TIMs in CST applications. The two defining properties of a TIM are its ability to (i) transmit sunlight and (ii) insulate the solar absorber. The selectivity of a TIM, $\Gamma$, is the figure of merit that is defined by the ratio of a TIM's transmittance to its apparent emissivity. A higher $\Gamma$ generally means a higher performing TIM.

**Chapter 2** reviews the spectral selectivity and thermal stability of silica aerogels and identifies opportunities for improvement. The selectivity of pure silica aerogels is too low for high temperature applications due to low infrared absorption within its infrared transparency window (3 – 5 μm). Silica aerogels also suffer from poor thermal stability at temperatures > 600°C due to viscous sintering. This degradation results in lower transparency and higher thermal losses.

The rest of the thesis details my efforts to improve the performance of silica aerogels for CST applications. **Chapter 3** covers the plasmon-enhanced greenhouse effect (PEGS) which improves the spectral selectivity of aerogels. Transparent plasmonic nanoparticles selectively increase absorption within the transparency window of silica aerogels and minimally affect the solar transmittance. This technique increases the selectivity and offers a pathway to enabling higher temperatures for linear solar receivers and increasing the efficiency of linear receivers in low concentration applications.

**Chapter 4** details the development of refractory aerogels, which are multicomponent aerogels fabricated by depositing a single cycle of alumina onto the silica backbone *via* atomic layer deposition (ALD). The refractory aerogels provide an order of magnitude improvement in thermal stability at 800°C compared to native silica aerogel.

**Chapter 5** presents the results of a modeling study that estimates the performance of silica aerogels in a proposed ambient pressure receiver and compares the performance to state-of-the-art selective surfaces. This study concludes that silica aerogels, in their native state, are likely less efficient than an ambient pressure receiver with selective absorbers. However, the introduction of ITO NPs, as discussed in **Chapter 3**, could elevate the performance of an aerogel-based receiver.

Lastly, **Chapter 6** builds upon the experimental work in **Chapter 4** by developing a refractory aerogel prototype linear receiver. The one-meter-long receiver tube is integrated with refractory aerogels. Heat loss measurements at high temperatures demonstrate the insulative properties of the refractory aerogels. This design is the first pilot-scale demonstration of a high temperature aerogel-based linear receiver.

# Chapter 2 : Review of Silica Aerogel Performance

## 2.1 Motivation

There are three properties that dictate the performance of a TIM: solar transmittance ($\tau$), thermal conductivity ($k$), and infrared absorption ($\beta$). The solar transparency enables greater absorption of incident sunlight while the latter two constitute the thermal losses ($Q_{loss}$) of the TIM (Figure 2.1). Silica aerogels are excellent candidate TIMs for CST applications because they exhibit high $\tau$, low $k$, and high $\beta$. For this reason, silica aerogels were identified as potential transparent insulators in 1989 when S. Svendson constructed a solar absorber constituting of two aerogels.[7]

Although aerogels are excellent candidates at room temperature, aerogels densify at elevated temperatures due to viscous sintering which is a densification mechanism in porous, glassy materials. Native silica aerogels tend to be metastable at temperatures less than ~550°C, but at higher temperatures, silica aerogels densify indefinitely. They are therefore unusable in CST applications above 600°C.

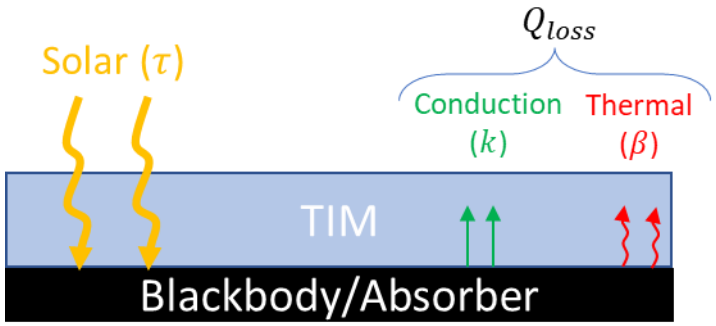


Figure 2.1. Important properties for TIMs in solar applications. The solar transmittance, thermal conductivity, and thermal opacity all dictate the performance of TIMs.

This chapter is primarily a review of the properties of silica aerogels, and it discusses the previous efforts of researchers to enhance the properties of aerogels. The first section briefly explains why aerogels are

transparent and what researchers have done to improve the transparency. The second section reviews methods that have improved the thermal insulating properties of aerogels, and why these techniques have failed. In the last section, I review the concept of viscous sintering and experiments that have resulted in improved thermal stability.

### 2.1.1 Current Performance of Real Materials

The selectivity of real materials is shown in Figure 2.2a.[8,11–17] We note that the plot only includes SAs and aerogels measured at temperature. The reflectance of most SAs is measured at room temperature with Fourier transform infrared (FTIR) spectroscopy, but this is known to greatly underestimate the emissivity at higher temperatures. Figure 2.2 shows that SAs tend to have better selectivity at lower temperatures (<500°C), but their performance degrades at higher temperatures, making aerogels the more promising choice for high temperature receivers. For reference, we also plot the ideal selectivity of a TIM or SA as a function of temperature at a concentration ratio of 50 suns. The non-monotonic behavior is due to the discontinuous nature of the solar spectrum. Figure 2.2a also shows that TIMs and SAs are far less selective than the theoretical limit. The $\Gamma$ of aerogels and SAs ranges from 2 – 5, while the theoretical limit is above 20 for all temperatures.

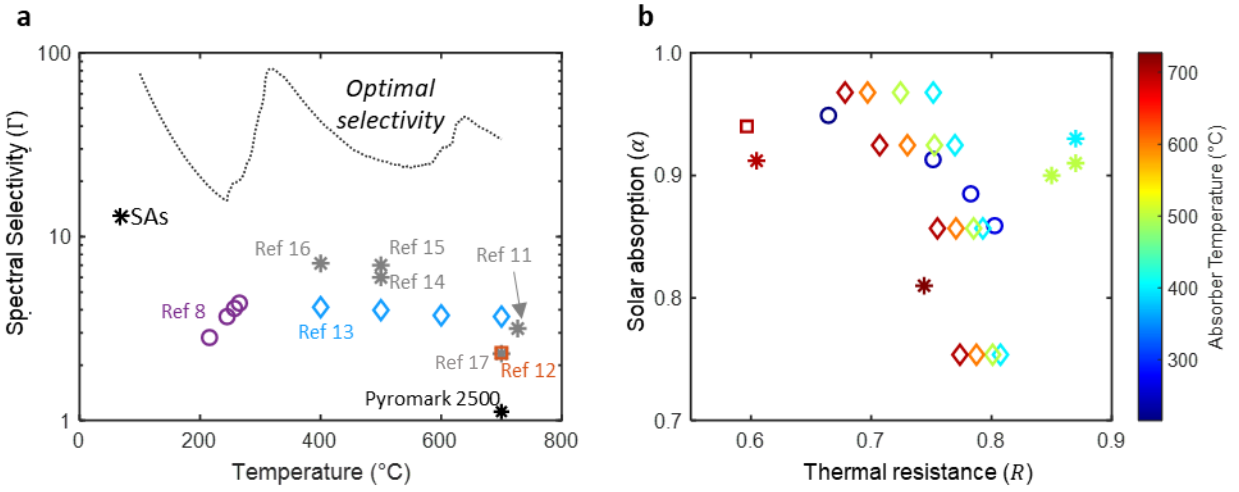


Figure 2.2. Spectral selectivity with respect to temperature. (a) Theoretically optimal spectral selectivity of a receiver with a concentration ratio of 50 suns *vs.* the experimental spectral selectivity of real SAs and aerogels. (b) Data from (a) replotted with respect to $\alpha$ and $R$.

Figure 2.2b replots the data from Figure 2.2a but breaks down the selectivity into the solar absorption ($\alpha$) and thermal resistance ($R$) of each material. The solar absorption of most aerogels and SAs is above 0.9, which means the selectivity can only increase by ~10% relative if solar absorption is optimized. The more important metric, rather, is the thermal resistance, which is generally below 0.8 ($\varepsilon$ > 0.2). Increasing $R$ from 0.8 to 0.9, without harming $\alpha$, doubles the spectral selectivity of the material since $\varepsilon$ decreases from 0.2 to 0.1. This again shows that it is critical to find methods to increase $R$ without sacrificing $\alpha$.

Another important property of real materials is that they have a temperature-dependent selectivity because as the temperature of the solar absorber increases, a larger fraction of its emission overlaps with the solar spectrum. The emissivity of real materials naturally increases as more thermal radiation is emitted where TIMs are transparent, or SAs are absorptive. This is evident in Figure 2.2 where the markers shift from a dark red in the lower left corner to light blue in the top right.

## 2.2 Solar Transmittance

There are three phenomena that affect solar transmittance – reflection, absorption, and scattering. Scattering is typically the most important loss mechanism in silica aerogels, typically responsible for over 60% of solar transmittance losses (Figure 2.3). Consequently, most research in improving the solar transmittance of aerogels has focused on the mitigation of scattering in aerogels. This section primarily focuses on the steps taken to minimize the scattering of aerogels, but it also covers the impact of specular reflectance and solar absorption.

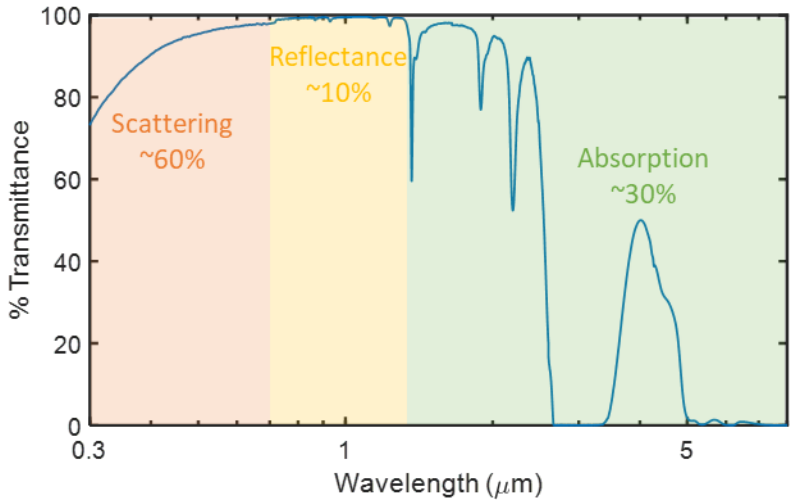


Figure 2.3. Regions where each transmittance loss mechanism dominates and their respective contributions to solar transmittance losses.

### 2.2.1 Scattering in Silica Aerogels

Scattering is the primary mechanism for solar attenuation in silica aerogels. Both the pores and the solid aerogel particles can scatter light since both result in a refractive index mismatch. There are two dominant scattering mechanisms within silica aerogels: Rayleigh scattering and Mie scattering. Each of these modes operates within a certain wavelength regime. Rayleigh scattering occurs when the wavelength of light is much larger than the size of the scattering particles or scattering pores ($\lambda \gg r_{pore}$), whereas Mie scattering occurs when the size of the particles or pores are comparable to the wavelength of light ($\lambda \approx r_{pore}$). Since the solar spectrum ranges from 350 – 2500 nm and the characteristic scattering radius of silica aerogels is <50 nm (Figure 2.4a), Rayleigh scattering is the dominant scattering mechanism. Figure 2.4b shows that Rayleigh scattering theory can predict the transmittance of aerogels.[18] One additional source of scattering loss occurs on the surface of aerogels. During the processing of aerogels, it is common that micron-sized silica particles or defects form on the outer surfaces of an aerogel, which lowers the transmittance of aerogels.[19,20] It broadly decreases the transmittance of aerogels, which makes the phenomenon look like reflectance losses. It is consequently important to ensure proper handling of aerogel samples to maintain clean outer surfaces to avoid this loss mechanism.

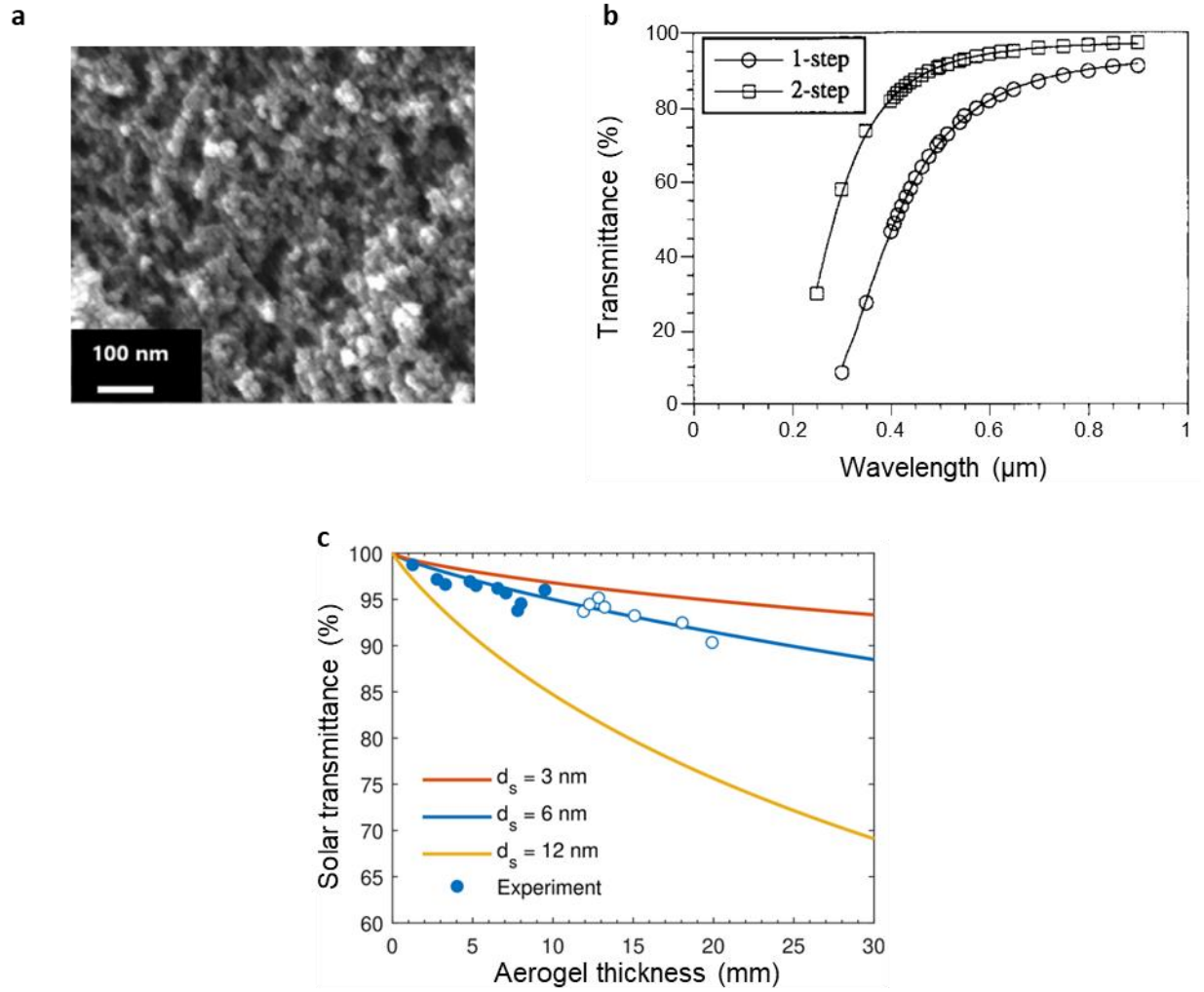


Figure 2.4. Scattering in silica aerogels. (a) A Rayleigh scattering fit agrees with the transmittance spectrum of silica aerogel, suggesting that Rayleigh scattering is the dominant scattering mechanism. (b) Experimental solar-weighted transmittances of aerogels synthesized with the "ultrafast hydrolysis condensation reaction." The solid lines are modeled transmittances using a specified size of scattering center (both pores and silica particles). Larger scattering centers increase the amount of scattering in aerogels so decreasing the size of the scattering centers is critical to increasing transmittance.

The method that produced the most transparent aerogels to date is a 1-pot base-catalyzed synthesis. Increasing transmittance with increasing base in a 1-pot synthesis was first observed by A. Emmerling *et al*.[20] Their findings appeared to initially disagree with other findings that showed base catalyzed, one-step syntheses had low transmittance, but these base-catalyzed samples contained impurity ions such as sodium or fluoride, whose impact on gelation is not well-known.[18,20,21] Only recently, Evelyn Wang's group at MIT developed an "ultrafast hydrolysis condensation reaction" which used concentrated ammonia as

the catalyst in a one-pot synthesis.[8] The high concentration of ammonia preferentially led to the bridging of silica particles rather than particle growth. The resulting silica aerogel particles are smaller and have more cross-linkage which leads to extremely small size features. The aerogels achieved record-high transparencies including a 9.5 mm thick aerogel with a solar-weighted transmittance of 96%.[8] This synthesis is the procedure that has been used in the aerogel syntheses in this thesis with only minor tuning of the ratios of reagents.

Besides tuning the amount of base catalyst in the reaction mixture, additional measures can be taken once the reaction mixture has gelated into a wet gel. E. Strobach *et al.* annealed aerogels after drying them supercritically and found that annealing aerogels at 400°C for 24h resulted in improved transmittance due to optimized restructuring of the aerogel network.[22] This technique, and others such as optimized aging time, are likely specific to specific synthesis, but the principles guide the development of better aerogels. For this thesis, all aerogels underwent a post supercritical drying anneal at 400°C for 24 hours specific metrics are likely unique to each aerogel synthesis and depend on the reaction and environmental conditions (temperature, humidity, *etc.*), but can be used as a guideline when designing an aerogel synthesis.

### 2.2.2 Reflectance

Aerogels naturally have low specular reflectance because their index of refraction is nearly 1. The low density of aerogels means the refractive index is closer to that of air (1) than the solid backbone (~1.5). This small index of refraction mismatch means that aerogels will always have a small specular reflectance.

The reflectance of an aerogel is directly related to its refractive index per the Fresnel equations, and the refractive index of aerogels is directly related to the density. Henning and Svensson first derived a relationship by assuming the refractive index of the aerogel was simply weighted by the volume and refractive indices of the constitutive components (Equation 4.1)[23]:

$$n_{aerogel} = n_{SiO2} v_{SiO2} + n_{air}(1 - v_{SiO2}) \quad (4.1)$$

where $n_{SiO2}$ and $n_{air}$ are the refractive indices of amorphous silica and air, and $v_{SiO2}$ is the volume fraction of silica in the aerogel. Ignoring the contribution of air, the density of the aerogel, $\rho_{aerogel}$, is:

$$\rho_{aerogel} = \rho_{SiO2} v_{SiO2} \tag{4.2}$$

Henning and Svensson assigned $n_{SiO2}$ = 1.45, $n_{air}$ = 1, and $\rho_{SiO2}$=2.2 g/cm$^3$, and then substituted Equation 2.2 into Equation 2.1 to come to the following relationship between the refractive index and density of an aerogel in units of kg/m$^3$:

$$n_{aerogel} = 1 + 0.21\rho_{aerogel} \tag{4.3}$$

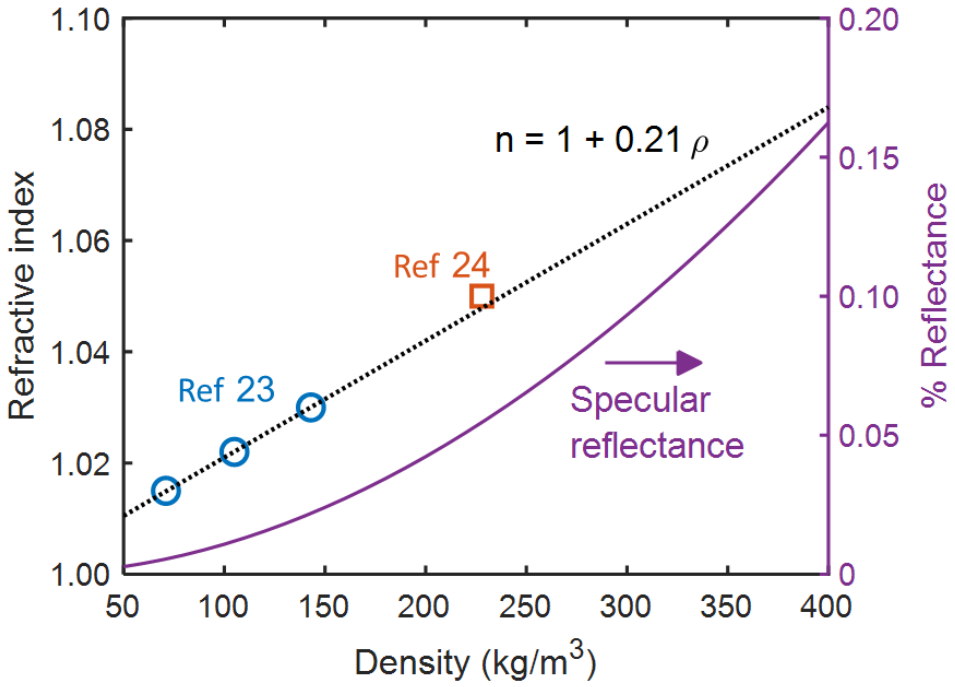


Figure 2.5. Refractive index and specular reflectance of aerogels. The refractive index of aerogels increases with increasing density as the aerogel approaches its bulk state. Even for relatively dense aerogels (400 kg/m$^3$), the reflectance of the aerogel is still very low (< 0.20%).

Figure 2.5 shows that this relationship accurately describes the refractive index of silica aerogels.[23,24] Figure 2.5 also shows that reflectance is a minor transmittance loss mechanism for all densities. Even a relatively dense aerogel of 400 kg/m$^3$ reflects very little incident light (< 0.20%).

### 2.2.3 Solar Absorption in Silica Aerogels

The primary absorbing species within the solar spectrum (300 – 2,500 nm) are water or derivatives of water such as silanol (Figure 2.6). The low atomic mass of hydrogen results in vibrational modes that occur at such short wavelengths (high frequencies). Silanol is a naturally occurring surface species for silica aerogels. Surface silanol groups adsorb atmospheric water *via* hydrogen bonding, and thus make aerogels naturally hydrophilic.

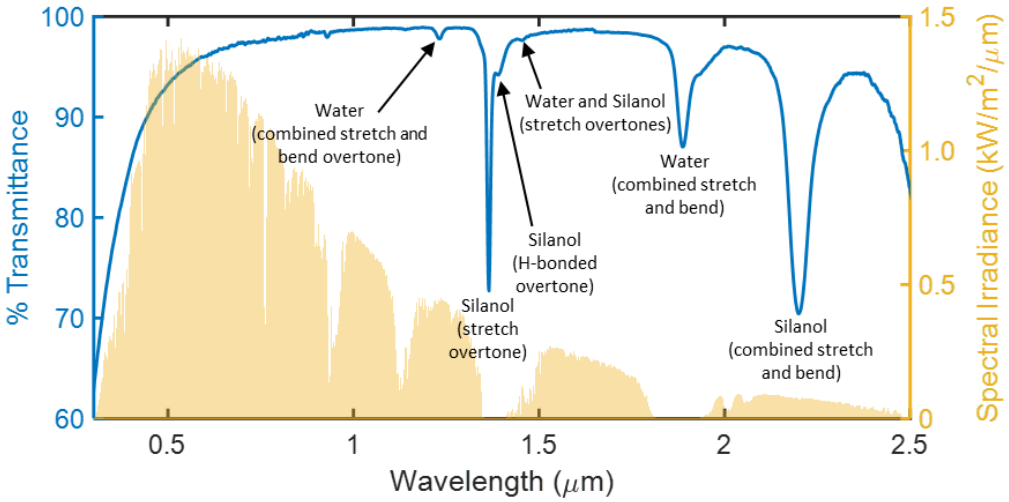


Figure 2.6. Solar absorption peaks in silica aerogels. All the solar absorption peaks are from silanol and water. Fortunate for CSP applications, most of the absorption peaks align with the absorption of atmospheric water, so their effect is small.

Although water and silanol have a significant number of absorption bands below 3 µm, their absorption has a small impact on solar transmittance because the peaks tend to align with the atmospheric absorption of water. Therefore, the hydrophilic nature of aerogels is not necessarily a detriment to the solar-weighted transmittance of silica aerogels. For example, the silica aerogel absorption peaks at 1.4 and 1.8 µm are caused by various overtone modes of water and silanol, but there is also no solar intensity in these regions due to the absorption of atmospheric water. Therefore, these absorption peaks are not considered parasitic. Other peaks such as the water peak at 1.25 µm and the silanol peak at 2.2 µm are

considered parasitic. Not all water absorption peaks on silica aerogels align with the atmospheric absorption of water since the overtone modes of liquid water are different from the overtone modes of water vapor, primarily due to coordinated hydrogen bonds.[25,26] The strengths of the short-wavelength peaks are relatively small, and the solar intensity is small for the 2.2 μm silanol absorption peak. Therefore, although parasitic, the impact of these absorption peaks is minor. Most of the research in the development of hydrophobic aerogels is done to enable ambient pressure drying[27–30] or to make flexible aerogels,[31,32] not to maximize the solar transmittance.

There are two primary methods to remove the surface silanol from aerogels: wet gel surface modification and post-drying annealing. For the former, silica precursors that contain methyl capping groups can prevent the formation of silanol groups during the gelation process. Known as silylating agents, common examples are dimethyldimethoxysilane (DMDMS) and trimethylmethoxysilane (TMMS). More information about this technique can be found in Chapter 3 of the *Aerogels Handbook*.[33] There are two main issues with silylating silica aerogels. The first is that it can be difficult to tune the resulting nanostructure of the aerogel. A. Günay *et al.* synthesized a hydrophilic aerogel with a density of only 30 kg/m$^3$, but when a silylating agent was added, the density increased to 147 kg/m$^3$. The two aerogels had significantly different solar transparencies (76% and 88%, respectively), but this is primarily a factor of the different nanostructure rather than a difference in hydrophobicity. The second issue is that the hydrophobic capping agents, silane groups (Si – $CH_3$), are unstable at elevated temperatures and will burn off under standard CST conditions.[34,35] A more effective strategy for removing parasitic absorption groups is to use post-drying annealing. E. Strobach *et al.* showed that annealing aerogels at 400°C causes only minor changes to the nanostructure of aerogels while inducing irreversible hydrophobic changes to the surface of the aerogel.[22] A later study showed that aggressive aging, such as 400°C – 600°C for ~100 days can nearly remove all traces of water, although the nanostructure is substantially changed.[36]

### 2.2.4 Summary of Aerogel Solar Transmittance

The predominant source of solar transmission loss in aerogels is the scattering of short-wavelength radiation. The current best method to produce high transmittance, low-scattering aerogels, is to use the

1-pot “ultrafast hydrolysis condensation reaction” developed by L. Zhao *et al.*[8] Otherwise, solar absorption in aerogels plays a relatively minor role due to overlap with atmospheric absorption bands. Specular reflection is typically under 1%. An area for future research is to continue to shrink the pore and particle sizes of aerogels to further increase the transparency by using stronger bases than ammonia or adjusting 2-step syntheses. This would incorporate lessons learned from the ultrafast hydrolysis condensation reaction.

## 2.3 Thermal Conductivity

Silica aerogels are one of the most insulating solid-state materials with measured thermal conductivities (at ambient pressure) around 20 mW/m/K. The low conductivity is a result of the extremely small pore and particle sizes of aerogels (both <50 nm). The internal gas molecules are in the Knudsen regime which prevents internal convection within the pores. Additionally, the small silica particles scatter and attenuate atomic vibrations that carry heat through amorphous materials.

In recent years, researchers have started to develop models that decouple the three different contributions to conductivity: solid, gaseous, and radiation. A model developed by S.Q. Zeng *et al.* uses various repeating geometric structures to mimic the structure of the silica aerogel network and estimate the contributions of the three heat transfer modes.[37] Various improvements to this type of model have been developed, including using a more descriptive spherical hollow cube model based on the structure of real aerogels.[38–40] In 2015, there were reviews of aerogel conductivity models, one by Y. He and T. Xie and one by G.H. Tang *et al.* They each provide an exhaustive summary of different models that researchers have used over the years to estimate the thermal conductivity of silica aerogels through experiments and simulations. The details of these models are outside the scope of this review, but below I highlight a few key conclusions from prior studies.

The first key takeaway is that the gas diffusion of aerogels constitutes a large fraction of the total thermal conductivity at room temperature – approximately 70% for a 114 kg/m$^3$ dense aerogel. **Error! Reference s ource not found.** uses the model developed by D. Dan *et al.*[40] and specifically shows how density impacts

the effect of gaseous and solid conduction. The relative contribution of gaseous conduction naturally decreases with density as there is less volume for gas.

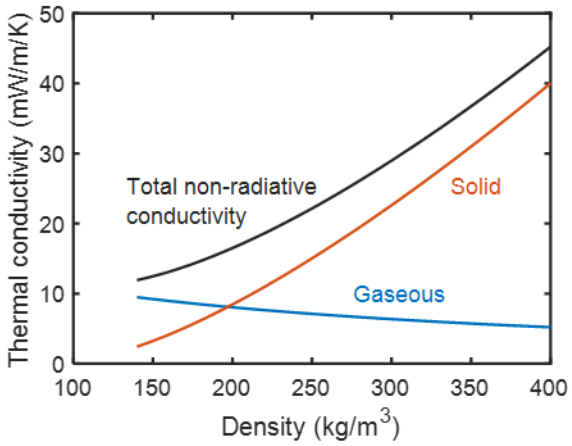


Figure 2.7. Reproduced results from the conductivity model developed by D. Dan *et al.*

A second key takeaway is that there is little experimental evidence that specific nanoscale features of an aerogel have a substantial effect on the thermal conductivity. Interestingly though, for the few modeling studies that account for nanoscale features, they find that large differences in the nanostructure are capable of very different thermal conductivities.[41,42] For example, a model by C. Bi and G.H. Tang predicts that the thermal conductivity of the aerogel backbone is highly dependent on the contact diameter of the aerogel particles. Specifically, the solid conductivity increases ~10x when the contact diameter increases from 0.1 to 0.7. However, when used for calculations, one value is usually chosen to fit the model to experiments. A recent model developed by C. Zhu and Z. Li.[42] found that a contact radius ratio of 0.25 provided an accurate value for all experimental values. Although the nanostructure affects the conductivity of aerogels in theory, there is little experimental evidence to support this. Rather, the density of the aerogel is the primary indicator of the solid conductivity of the aerogel. J. Fricke *et al.* found that the solid conductivity is proportional to the density of the aerogel raised to the 1.5 power (i.e., $\lambda_s = \rho_{aerogel}^{1.5}$).[43]

Lastly, there is little dependence on the non-radiative conductivity of aerogels with temperature. Recent modeling by Y. Dai *et al.* shows that the gaseous and solid conductivities remain mostly the same from 300 – 900K.[44] In fact, the authors predict that the gaseous conductivity decreases at higher temperatures, primarily due to the decreased density of gas with increasing temperature and constant pressure. T. Xie *et al.* also found the same conclusion in their work.[45] These conclusions enable the use of temperature-independent non-radiative thermal conductivities when estimating the heat losses through aerogels.

The literature on silica aerogel conductivity shows that tuning the nanostructure of the aerogel has a small impact on conductivity. Furthermore, as will be shown in **Chapter 5**, the non-radiative conductivity of aerogels has minimal impact on the overall heat losses in high-temperature aerogel-based receivers.

## 2.4 Thermal Opacity

Silica aerogels are very absorptive at wavelengths longer than 5 µm (Figure 2.8). At shorter wavelengths, silica aerogels are relatively transparent except for absorption by surface-bound groups (*i.e.*, hydrogen bonded) and surface-adsorbed species such as water. For this reason, the term "infrared transparency window" has been commonly associated with the region 3 - 5 µm. Increasing the absorption within this region is critical to improving the insulation properties of aerogels, especially at higher temperatures where the peak of the blackbody emission curve shifts to shorter wavelengths. This section covers methods to increase the thermal opacity of aerogels to reduce these thermal radiative losses.

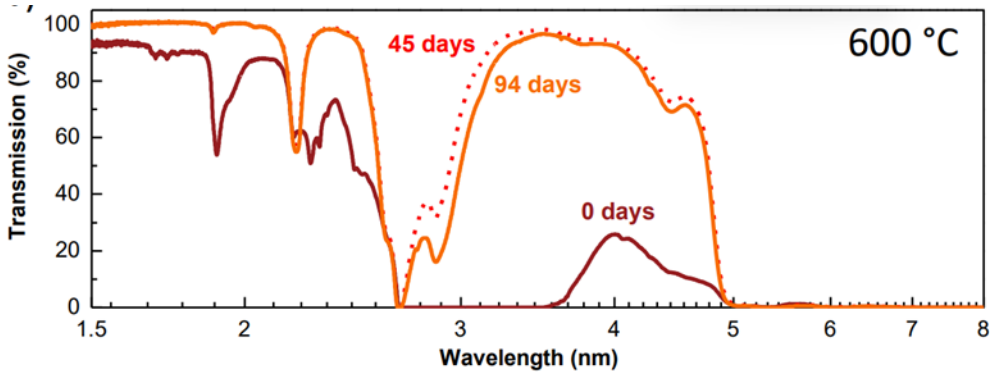


Figure 2.8. Infrared transmission spectra of aerogels post-annealing at 600°C. Exposure to high temperatures removes water and silanol absorption peaks that are useful in suppressing heat losses in solar thermal applications.

### 2.4.1 Role of Water and Silanol

As covered in **2.2.3 Solar Absorption in Silica Aerogels**, water and silanol groups are the primary species that absorb radiation below 5 μm in silica aerogels. At high temperatures, however, water desorbs from the aerogels and surface silanol groups undergo a condensation reaction, which ultimately leads to a hydrophobic aerogel (Figure 2.8). Coordinated silanol groups (H-bonded) are largely removed and the only remaining species are isolated (free) silanols. With less water and silanol to absorb infrared radiation, the infrared transparency window of aerogels increases to the point where the aerogel is transparent below 5 μm, except for the two peaks at 2.2 and 2.7 μm. As a result, silica aerogels are increasingly poor insulators as the temperature of the absorber increases.

Nonetheless, even for absorber temperatures as high as 700°C, the cold regions in the aerogel could retain some water and silanols. Temperature-dependent FTIR measurements by L. Zhao *et al.* on native silica aerogels found that water accounted for over 5% of the aerogel weight at 200°C – enough to suppress heat losses in that region.[8] The same work shows that the transmittance of an aerogel at 200°C is ~0.2 at 4 μm, far lower than the near 100% transmittance after exposure to 600°C. Therefore, methods to further increase the hydrophilicity of aerogels and maintain higher water adsorption at higher temperatures show potential.

### 2.4.2 Broadband, Non-selective Opacifiers

The Rosseland approximation (**1.4 Estimating the Thermal Resistance of Real TIMs**) models a diffusive process of radiative transfer, so it effectively treats absorption and scattering as the same phenomenon. The benefit of scattering radiation is that any material can be used since scattering is mostly size-dependent, which enables a large class of minerals and stable oxides as candidate materials for scattering opacifiers. For these reasons, earlier studies investigated the use of thermally stable fibers, such as titania and iron oxide, to reduce the radiative conductivity at high temperatures.[46–48] The problem with scattering opacifiers for solar uses is that scattering is typically non-selective. Selectively scattering infrared radiation at ~3 μm without also scattering solar radiation has not been achieved.

Broadband absorbing opacifiers such as carbon also received interest early on.[49–52] Although carbon-opacified aerogels can decrease the effective thermal conductivity by over an order of magnitude at higher temperatures, carbon absorbs sunlight, rendering this opacifier poorly suited for solar applications.

### 2.4.3 Future Directions of Selective Opacifiers

Previous methods to thermally opacify aerogels have also opacified the solar transmittance, but there are a few possible solutions that may solve this problem. The first is the use of selectively transparent materials, such as transparent conducting oxides (TCOs). This class of materials is mostly transparent to sunlight while also exhibiting the ability to strongly absorb thermal radiation. Localized surface plasmon resonances result in strong absorption peaks in the infrared. Since TCOs can also be tuned with different doping levels, the strength and location of the LSPR peak can also be tuned. Alternatively, functionalizing the surface with infrared absorbing species, such as carbonates, could selectively increase infrared absorption without affecting the solar transmittance. The only downside of this technique is that most organic functional groups are not thermally stable. Carbonate, for example, degrades to carbon dioxide at high temperatures, but this brings up a third possible solution. If silica aerogels are filled with greenhouse gases, rather than air (mostly oxygen and nitrogen), thermal radiative losses can be suppressed in the same way greenhouse gases are warming the planet. Greenhouse gases are nonabsorptive in the solar region, providing another way to preferentially increase infrared absorption.

## 2.5 Thermal Stability of Aerogels

The thermal stability of silica aerogels is critical to their use in solar receivers since the lifetime of CSP plants is ~25 years. The most commonly measured property for degradation is the volumetric shrinkage of aerogels. The associated densification impacts many of the desirable properties of aerogels including their high transmittance and low thermal conductivity. Further, densified aerogels may expose the solar absorber, potentially leading to high thermal losses. Work by E. Strobach *et al.* studied the impact of long-term isothermal exposure on the performance of silica aerogels (Figure 2.9a).[36] The study showed that the thermal conductivity and the solar transmittance (Figure 2.9b) of the aerogels degrade as a result of the densification. Additionally, at all temperatures, densification is initially rapid and severe. This process slows down if the aerogels are annealed at temperatures < 600°C. At 600°C and above, however, the

aerogels are unstable, and their volume shrinks continuously over the course of the 150-day experiment, though the effect is far more pronounced for the 800°C anneal.

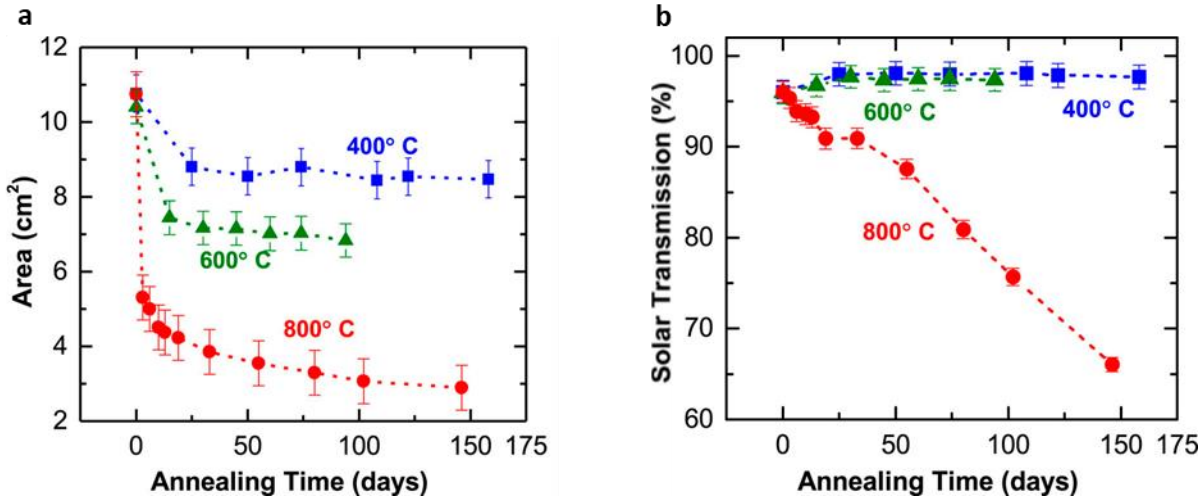


Figure 2.9. Densification of silica aerogels at high temperatures. (a) Projected area shrinkage and (b) solar-weighted transmittance of silica aerogels with respect to annealing conditions.

These results show there are two regimes of aerogel densification: (i) an initial rapid densification, (ii) and a longer-term asymptotic densification. Early work on the mechanism of densification in aerogels shows that aerogels densify through viscous sintering, which is the rearrangement and sintering of particles to minimize their surface energies. The predominant property that defines viscous flow is the viscosity. For common materials, the viscosity tends to decrease by an order of magnitude every 20-40°C, which explains the rapidly increasing densification kinetics with temperature.[53] Most theories are based off of a viscous flow model for cylindrical particles, such as the one developed by Scherer.[54] The issue though, is that the model tends to break down at longer times scales (i.e., the asymptotic regime) because the properties change, such as an increasing viscosity.[55] A more fundamental review of the mechanism and models of viscous sintering for porous materials can be found in Chapter 11 of *Sol-gel Science* by C. Jeffrey Brinker and George W. Scherer.[53]

### 2.5.1 Multicomponent Aerogels

Naturally, the best method to stabilize silica aerogels is to introduce a secondary component that increases the viscosity of the aerogel particles which would then slow down the degradation rate. This is a common theme in the field of ceramics where compounds such as alumina, zirconia, and magnesium

oxide have been used as secondary components in aerogels.[56] Mullite has been the most researched multicomponent gel for its creep resistance, chemical stability, thermal stability, and low thermal-expansion coefficient.[57] This was first noticed – albeit unintentionally – by S. Komarneni *et al.* in 1986.[58] They synthesized mullite *via* a sol-gel process with the intention of sintering it to make a fully homogenous glass, but noticed the poor "sinterability" of the mullite gels. The first observation of using mullite to slow the degradation of an aerogel was by F. Cluzel *et al.* in 1991.[59] They developed mullite aerogels and noticed that stark improvements in the thermal stability occurred when the alumina-silica composite gels formed certain phases, such as the pseudo-boehmite–γ-alumina phase. After this, multiple researchers investigated multicomponent gels for the purposes of thermal stability.[60–64]

The primary limitation of most of these methods is that there is limited control of the nanostructure of the resulting gels. Multicomponent aerogels were synthesized *via* sol-gel processes that combined metal alkoxide precursors, such as aluminum tributoxide, with more traditional silica precursors. However, the kinetics and selectivity of the reactants can vary widely, which complicates the tunability of the resulting nanostructure. Up until 2010, the purpose of the multicomponent aerogels was for high temperature insulation in industrial processes or catalytic supports.[65] The transmittance of the multicomponent aerogels was largely ignored.

Recently, there have been advancements in the development of multicomponent aerogels for solar thermal applications. Since maintaining high transmittance is critical, any introduction of additional components should aim to preserve the nanostructure of the aerogel. Atomic layer deposition (ALD) is a deposition process with tunability down to the monolayer, so it is an extremely promising technique to produce transparent multicomponent aerogels. S.O. Kucheyev *et al.* first attempted to modify the surface of silica aerogel monoliths *via* atomic layer deposition (ALD) in 2005 when they coated aerogels with ~2 nm of zinc oxide.[66] After this, numerous researchers investigated ALD on aerogels,[67–70] including the development of refractory aerogels for high temperature use.[71] The primary issue in the early days of ALD on aerogels is poor transmittance of the resulting multicomponent. T.W. Hamann *et al.* noticed in their

deposition of $TiO_2$ that while the uncoated silica films are transparent, they became “opaque-white due to scattering” of $TiO_2$.

## 2.6 Summary and Outlook

There is a pathway to making high performing silica aerogels for next-generation linear receivers. The first step is to synthesize aerogels with as high solar transmittance as possible, which is done by using the framework established by L. Zhao *et al.*[8] To address the thermal insulating properties, some infrared absorbing components are required to improve the performance. Lastly, thermal stability should be addressed by adding a refractory oxide without affecting the aerogel nanostructure. The next two chapters of this thesis take the lessons learned from this literature review.

# Chapter 3 : Plasmon-Enhanced Greenhouse Effect for High Temperature Solar Energy Conversion

*The contents of this chapter are based on published work reported in ACS Nano in 2020.*[13]

## 3.1 Motivation

Greenhouse gases absorb and re-emit thermal radiation hundreds of times as heat from the Earth's surface gradually diffuses through the atmosphere and escapes to Space. This slow diffusive loss of energy from the Earth coupled with the ballistic transmission of sunlight through the atmosphere leads to the well-known greenhouse effect, which was proposed by Fourier and later modeled by Arrhenius.[42–44] Without the greenhouse effect, the surface temperature on Earth would be ~33°C cooler, and thus uninhabitable. However, the atmospheric buildup of greenhouse gases has escalated the effect to the point that global warming is threatening the existence of many living species.[45]

In a similar fashion, transparent aerogels suppress re-radiation losses from solar absorbers by leveraging the greenhouse effect (Figure 3.1). Sunlight is transmitted to an underlying black absorber surface or cavity, while thermal radiation is forced to undergo many absorption and re-emission events before escaping. To accomplish this task, the thermal absorption coefficient must be large in the spectral range where blackbody radiation peaks. Unfortunately, to date, the absorption coefficients of transparent aerogels are too low to achieve very high efficiency at 600°C and above. Silica aerogels, despite their high solar transparency and low thermal conductivity,[34,47–49] suffer from large radiative losses at high temperatures. These losses are mainly due to desorption of water and dehydroxylation of surface silanol groups at higher temperatures,[50] resulting in low absorption below 5 μm. Transmission through this spectral range is important because it overlaps a significant fraction of Planck's blackbody distribution. Even at the upper bound of practical aerogel thicknesses, losses through this transmission window persist.

Previous work on improving the spectral selectivity of silica aerogels has largely focused on improving solar transmission.[5,50–52] Methods to increase the thermal opacity of silica aerogels have been explored for use as advanced thermal insulation, but no work to date has demonstrated increased infrared attenuation in aerogels while maintaining high solar transmission.[53,54] For example, Kuhn *et al.* used micron-sized titania and alumina particles to scatter thermal radiation,[39] while Lee *et al.* used carbon (a broadband absorber) to increase infrared absorption;[38] however, both modifications resulted in loss of solar transparency.

This chapter introduces and experimentally demonstrates the concept of using infrared plasmon resonances to selectively enhance the thermal absorption coefficient of TIMs and strongly suppress thermal radiative losses at high temperatures. This phenomenon is called the plasmon-enhanced greenhouse selectivity (*PEGS*). Unlike silica aerogels, where much of the IR absorption is lost at high temperatures, local surface plasmon resonances (LSPRs) in doped oxide nanoparticles overlap a significant portion of the blackbody spectrum and are maintained at high temperatures. Within the aerogel transparency window (3 – 5 µm), these plasmonic aerogels have significantly higher absorption than state-of-the-art silica aerogels.[4] The increase in infrared absorption nearly halves the heat loss at 700°C. Overall, this chapter demonstrates that *PEGS* is strong enough to overcome other parasitic modes of heat loss, such as conduction, to significantly improve spectral selectivity in next-generation high-temperature solar energy systems.

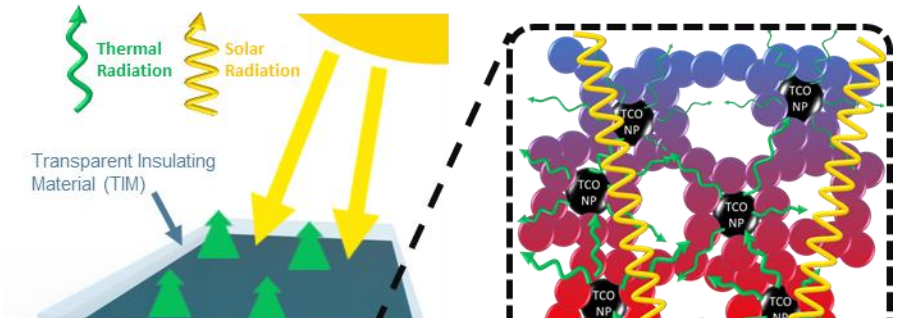


Figure 3.1. Solar thermal energy conversion using greenhouse selective materials. Schematic of a receiver configuration where a transparent insulating material (TIM) is in thermal contact with a blackbody absorbing surface on one side and exposed to the surroundings on the other. Zoomed in schematic shows how resonant absorption inside the TIM can force thermal photons to undergo absorption and emission prior to escaping. The mean free path of thermal photons is proportional to the radiative heat losses out of a thermally opaque TIM.

## 3.2 Results and Discussion

### 3.2.1 Theoretical Description of *PEGS* in the Radiative Limit

To demonstrate that infrared LSPRs can theoretically enhance selectivity (Γ), I first model the optical properties of a 5 mm thick, 160 kg $m^{-3}$ dense silica aerogel with dispersed transparent conducting oxide (TCO) nanoparticles (NPs). TCO NPs were chosen because of their known ability to transmit sunlight and absorb strongly in the infrared.[46,47] The permittivity of the TCO NPs is assumed to be well described by a Drude model given by:

$$\epsilon = \epsilon_\infty - \frac{\omega_p^2}{\omega^2 - \omega\gamma i} \tag{3.1}$$

where $\epsilon$ is the permittivity, $\epsilon_\infty$ is the core dielectric constant, $\omega$ is the radial frequency of light, $\omega_p$ is the plasma frequency, and γ is the damping coefficient. We chose parameters for the Drude model that are representative of bulk TCOs (specifically ITO).[39] To account for the size effects of using nanoparticles, a simple dependence model is used:

$$\gamma = \gamma_{bulk} - \frac{A\upsilon_f}{R} \tag{3.2}$$

where, $A$ is a material and shape-dependent coefficient, $\upsilon_f$ is the Fermi velocity of the electrons, and $R$ is the radius of the particle. $A = 1$ is chosen to be consistent with literature.[48] The Fermi velocity is defined by Equation 3.3 where $E_f$ is the Fermi energy and $m_e$ is the mass of the electron. The Fermi energy is calculated from Equation 3.4 where $\hbar$ is the reduced Planck's constant and $N$ is the free electron density in the TCO. Given the plasma frequency, the free electron density, $N$, is calculated using Equation 3.5 where $\epsilon_o$ is the permittivity of free space and $e$ is the charge of the electron.

$$\upsilon_f = \sqrt{\frac{2E_f}{m_e}} \tag{3.3}$$

$$E_f = \frac{\hbar^2}{2m_e} * (3\pi^2 N)^{\frac{2}{3}} \tag{3.4}$$

$$N = \frac{\omega_p^2 \epsilon_o m_e}{e^2} \tag{3.5}$$

On their own, TCO NPs show relatively low solar attenuation and an infrared absorption peak around 4.5 μm due to the LSPR based on a Rayleigh description of absorption. This peak aligns well with the transparency window of silica aerogels (Figure 3.2a).

Using the modeled TCO NP extinction coefficients and the previously reported extinction coefficients of unaltered silica aerogels (near room temperature),[4,49] Figure 3.2a shows the modeled solar transmission and infrared extinction of a silica aerogel with TCO NPs dispersed at a volume fraction of 0.02%. The results show that solar transmission is slightly reduced due to Rayleigh scattering at short wavelengths, as well as absorption from the LSPR tail in the near-IR. Meanwhile, at the peak of the LSPR, the absorption coefficient increases 22-fold for the TCO NP aerogel. This significant absorption within the aerogel infrared transparency window increases the Rosseland absorption coefficient from 2.0 $cm^{-1}$ for the silica aerogel to 7.5 $cm^{-1}$ for the TCO aerogel.

Figure 3.2b shows the theoretical improvement in receiver efficiency (in the radiative limit) at elevated temperatures due to the addition of TCO NPs. The curvature in this plot is due to a temperature dependence of $\beta$ (See subchapter 1.4). In the radiative limit, $T_{max}$ increases from 526°C to 668°C under 10 suns ($\Phi_{max}$ increases from 25 to 46). This modeling shows that plasmonic nanoparticles can significantly increase $\Gamma$ and allow solar collectors to achieve higher maximum temperatures and efficiencies.

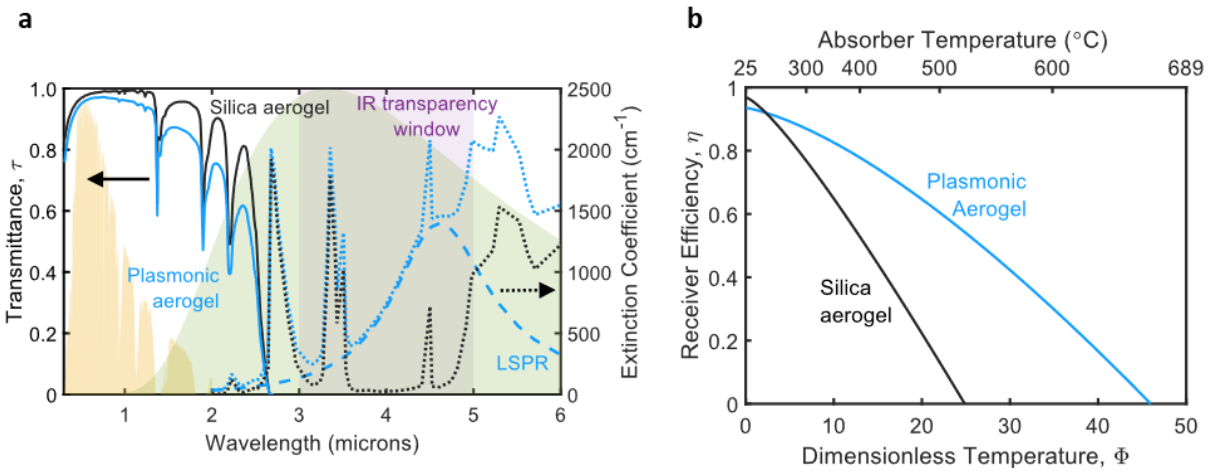


Figure 3.2. Plasmon-enhanced greenhouse selectivity in the radiative limit. (a) Modeled optical transmittance and infrared absorption coefficient of silica aerogel with and without TCO NPs. Unaltered silica aerogels have a low extinction coefficient in their infrared transparency window (purple region) which is enhanced by the LSPR (dashed line). Solar and 600°C blackbody spectra are shown for reference. (b) Modeled dependence of the receiver efficiency, $\boldsymbol{\eta}$, in the radiative limit on the dimensionless temperature, $\boldsymbol{\Phi}$, under 10 suns of solar irradiance. The plasmonic aerogel greatly outperforms the silica aerogel at elevated temperatures because of its increased infrared absorption.

### 3.2.2 Experimental Demonstration of *PEGS*

To experimentally demonstrate the proposed *PEGS* mechanism, plasmonic aerogels (PAs) were synthesized by incorporating indium tin oxide (ITO) NPs into a silica aerogel (Figure 3.3). Aerogels were synthesized *via* a sol-gel polymerization of tetramethylorthosilicate (TMOS, 218472, Sigma-Aldrich) with DI water and ammonia ($NH_3$, 341428, 2.0M in methanol, Sigma-Aldrich) as the catalyst. Two different solutions are first prepared. TMOS is diluted in methanol (MeOH, 322415, Sigma-Aldrich), and ammonia solution is added to DI water. The two solutions are then mixed in plastic syringes where gelation is allowed to proceed. For the PAs, drops of disbursed ITO NPs in ethanol (US7656, US Research Nanomaterials, Inc) were added to the water-ammonia solution before mixing. Once the wet gels formed, they were aged for 1 week with daily ethanol washes to remove contaminants and water. The aerogels were then dried using $CO_2$ critical point drying (CPD, model 915B, Tousimis). Upon drying, the aerogels were annealed at 400°C for 24 hours in a Vulcan oven to remove any organic contaminants or surfactants.

The resulting aerogels are 3.5 mm thick with varying volume fractions of NPs (up to 0.024%). The addition of the NPs has a negligible effect on the density and thermal conductivity of the aerogels which are

approximately 160 kg $m^{-3}$ and ~20 $Wm^{-1}K^{-1}$, respectively. The thermal conductivity of the aerogels was measured using the transient plane source (TPS) method (Hot Disk TPS 2500 S) and Kapton sensors (Hot Disk Kapton 5465) with a heating power of 5 mW for a duration of 40 seconds. Similar to the TCO NPs modeled above, the ITO NPs have an LSPR at approximately 5 μm (Figure 3.3c). UV-vis and FTIR transmission spectroscopy was used to obtain the spectra in Figure 3.3c. A UV-Vis-NIR spectrophotometer (Shimadzu UV-3600 Plus) with an integrating sphere attachment (Shimadzu, ISR-603) was used for wavelengths <2.6 μm, and the infrared transmission measurements were obtained with a Fourier transform infrared (FTIR) spectrophotometer (Fisher Scientific Nicolet iS50). No integrating sphere is needed since scattering is negligible in the infrared.

Notably, the highest volume fraction of TCO NPs eliminates the undesirable mid-IR transparency window. By adding the measured extinction coefficient of the ITO NPs (Figure 3.3c) to literature silica aerogel extinction coefficients,[49] $\beta$ increases from 7.2 to 18.2 $cm^{-1}$ at 700°C. Meanwhile, the measured solar weighted transmittance decreases from 0.95 (without NPs) to 0.70 at the highest volume fraction. The increase in infrared absorption from the ITO NPs outweighs the decrease in solar transmittance, resulting in higher $\Gamma$. In the radiative limit, the model shows that the addition of plasmonic nanoparticles increases the greenhouse selectivity of the aerogel from 2.3 to 4.5 which translates to an increase in $T_{max}$ from 506°C to 661°C under 10 suns (Figure 3.3d). This calculation assumes negligible conduction and that the radiative properties of the aerogel and NPs are independent of temperature.

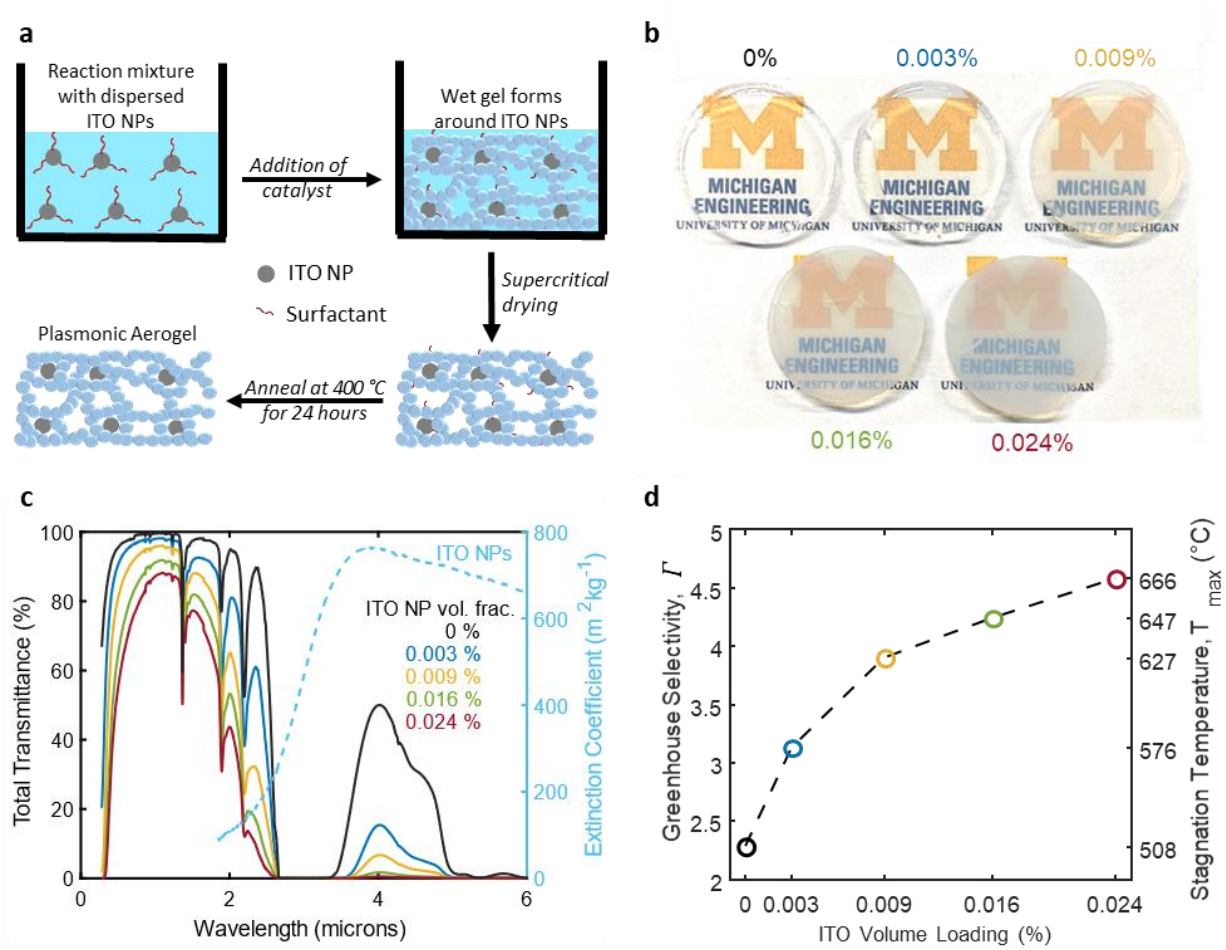


Figure 3.3. Radiative properties of synthesized plasmonic aerogels. (a) Process of fabricating plasmonic aerogels (PAs): ITO NPs are mixed into the aerogel reaction mixture; upon addition of the sol-gel catalyst, the aerogel backbone forms around the particles; critical point drying and annealing removes the surfactant. (b) Photograph of the plasmonic aerogels. (c) Measured total transmittance of the PAs (solid lines) and infrared absorption of the ITO NPs (dotted line). The presence of the ITO increases the infrared absorption by eliminating the infrared transparency window of silica aerogels. The peak of the ITO absorption aligns well with the infrared transparency window of silica aerogels. (d) Greenhouse selectivity of the PAs at their stagnation temperature. The increase in greenhouse selectivity enables higher temperatures.

To experimentally determine the effective selectivity of the PAs, which accounts for conduction through the solid phase and the temperature-dependence of the thermal absorption coefficient, I used an in-house experimental heat flux technique that measured the heat flux through the aerogels (Figure 3.4a). The aerogels are placed between a variable-temperature hot stage (Instec Inc.) and a heat flux sensor (XP 26 9C, greenTEG AG) that is grounded to a cold plate (copper) maintained at ~30°C and covered by a reference blackbody surface (Metal Velvet, Acktar). Figure 3.4b shows how the measured heat flux

increases with hot-stage temperature. It is important to note that the aerogel samples were stable at 700°C for the duration of the experiment.

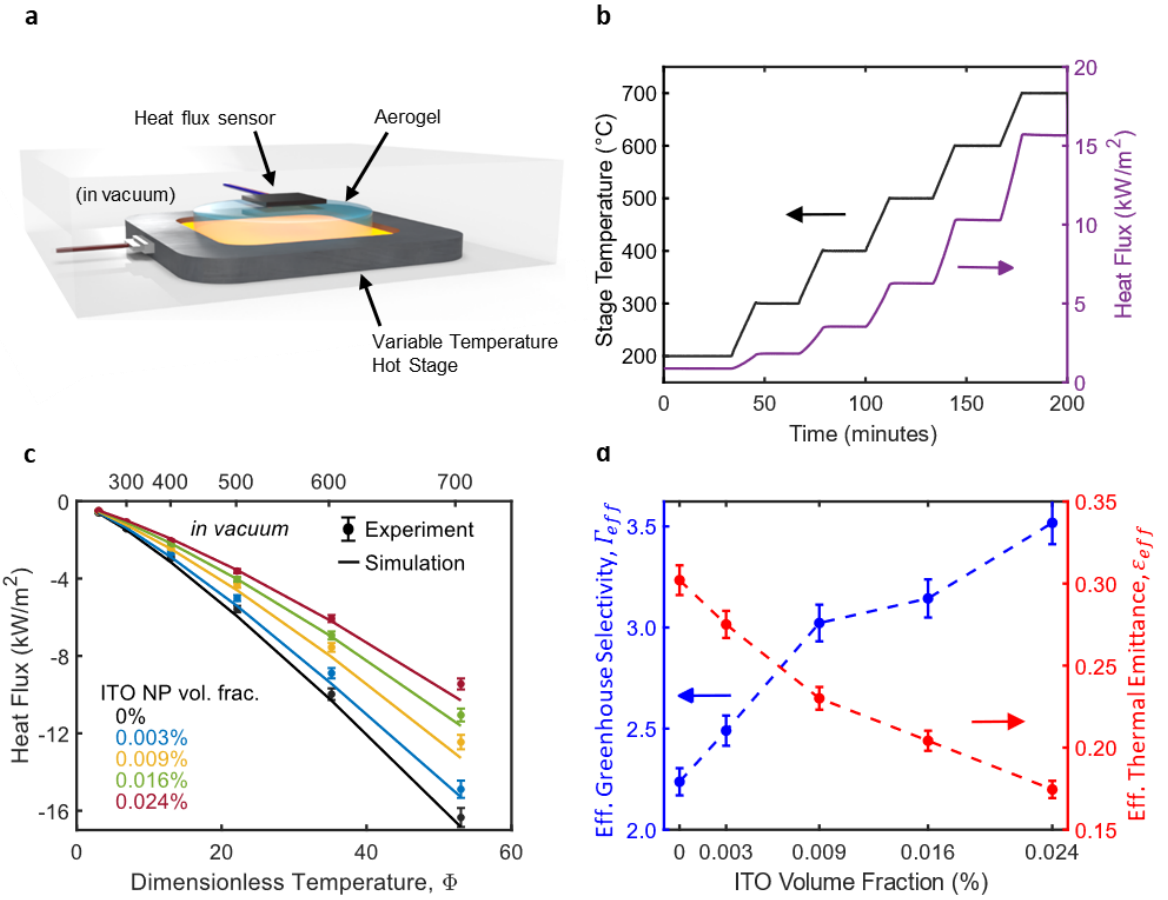


Figure 3.4. Experimental demonstration of PEGS. (a) The experimental setup used to measure the heat flux through the PAs under dark, vacuum conditions. A heat flux sensor with blackbody tape measures heat loss from the aerogel *versus* varying absorber surface temperature. (b) Example time-series data of the measured heat flux *versus* the stage temperature setpoint. (c) Experimental (points) and simulated (solid lines) temperature-dependent heat losses with increasing ITO loading. (d) Effective greenhouse selectivity (blue) and effective thermal emittance (red) of the PAs at 700°C.

Fig. 3.4c shows the reduction in heat losses with increasing ITO volume fraction. Notably, a nearly 50% reduction in heat losses (at 700°C) is observed for the highest ITO volume loading relative to the silica aerogel. The decrease in the heat flux is attributed to the plasmon-enhanced suppression of radiative transfer resulting from the increased infrared absorption and consequently decreased mean free path of thermal radiation. These measurements provide validation that radiative losses are indeed significant at elevated temperatures in our PAs and can be significantly suppressed *via PEGS*. Furthermore, the experimental data shows good agreement with our numerical heat transfer model (Chapter 2).

The apparent selectivity, $\Gamma_{app}$, is calculated using the measured heat losses (Figure 3.4c) and solar-weighted transmittances (Figure 3.3c) according to Equations 2.4 and 2.5. The selectivity increases from 2.2 to 3.5 with increasing ITO volume loading. The results are similar to Figure 3.3d, although the selectivity gains are less pronounced due to the presence of conduction. While the 0.024% sample produces the highest stagnation temperature (largest $\Gamma_{app}$), it may not be the optimal volume fraction once a performance or cost optimization of the entire CST system is considered. Nevertheless, these experimental measurements demonstrate that *PEGS* is strong enough to overcome parasitic conduction in evacuated aerogels.

Lastly, Figure 3.4d compares the performance of PAs to reported selective surfaces based on effective thermal emittance ($\varepsilon_{app}$) which is calculated using measured heat losses according to Equation 2.5. Figure 3.4d shows $\varepsilon_{app}$ at 700°C as a function of ITO fraction. For the aerogel without NPs, which is representative of the state-of-the-art, $\varepsilon_{app}$ is 0.30 ± 0.02 at 700°C. In contrast, the addition of ITO NPs decreases $\varepsilon_{app}$ to 0.17 ± 0.01 – a record-low among selective surfaces or transparent insulating materials at such high temperatures.[8,50–52] This work thus demonstrates that the *PEGS* mechanism is strong enough to significantly suppress thermal losses and increase the greenhouse selectivity of TIM-based solar thermal receivers. More broadly, it shows that plasmonic resonances can be used to tune the spectral selectivity of mesoporous media, such as silica aerogels.

## 3.3 Conclusions

This chapter shows the incorporation of 0.024% ITO nanoparticles (by volume) into a silica aerogel reduces heat losses by ~42% under evacuated conditions. This corresponds to an experimentally measured effective thermal emittance of ~0.17 at 700°C, which is the lowest reported across selective solar absorbers and transparent insulating materials at such high temperatures. These large reductions in heat loss outweigh the ~25% parasitic loss in solar transmittance. Overall, the apparent selectivity increases from 2.2 to 3.5, demonstrating the mechanism of plasmon-enhanced greenhouse selectivity (*PEGS*). This study establishes a method for leveraging *PEGS* in high-temperature solar energy systems, which are

important for the necessary transition to renewable energy and consequent reduction in atmospheric greenhouse gases.

## 3.4 Future Directions

Although this study demonstrated the potential for the *PEGS* mechanism, there is still substantial room for improvement due to the lower-than-expected solar transparency (Figure 3.5). Aggregation of ITO NPs is largely responsible for this observed decrease in transparency. The scattering and absorption properties of the ITO NPs were measured by both UV-Vis-NIR spectroscopy and Fourier transform infrared (FTIR) spectroscopy. For the former, we measured the transmittance of the particles in a diluted solution (Figure 3.5a). The results show that the particles have low attenuation throughout most of the solar spectrum but absorb in the infrared. We also determined the scattering properties of the ITO NPs by fitting a Rayleigh scattering model to the extinction coefficient at short wavelengths (Figure 3.5b). The slope of the Rayleigh prediction agrees with the data between 300-450 nm, consistent with the spherical geometry of the ITO NPs (Figure 3.5c,d) and the particle size (~18 nm), which is smaller than the wavelength of interest.

Figure 3.5e shows the actual and expected transmission spectra (using the Rayleigh model from Figure 3.5b). The experimental transmission spectra are lower than predicted by simulation, likely due to aggregation of ITO NPs during synthesis, resulting in effectively larger particles that produce scattering at longer wavelengths. NP aggregation is also observed in the TEM images of the ITO NPs in the silica matrix (Figure 3.5d). In particular, some of the ITO NPs are aggregated without being encapsulated by the aerogel matrix.

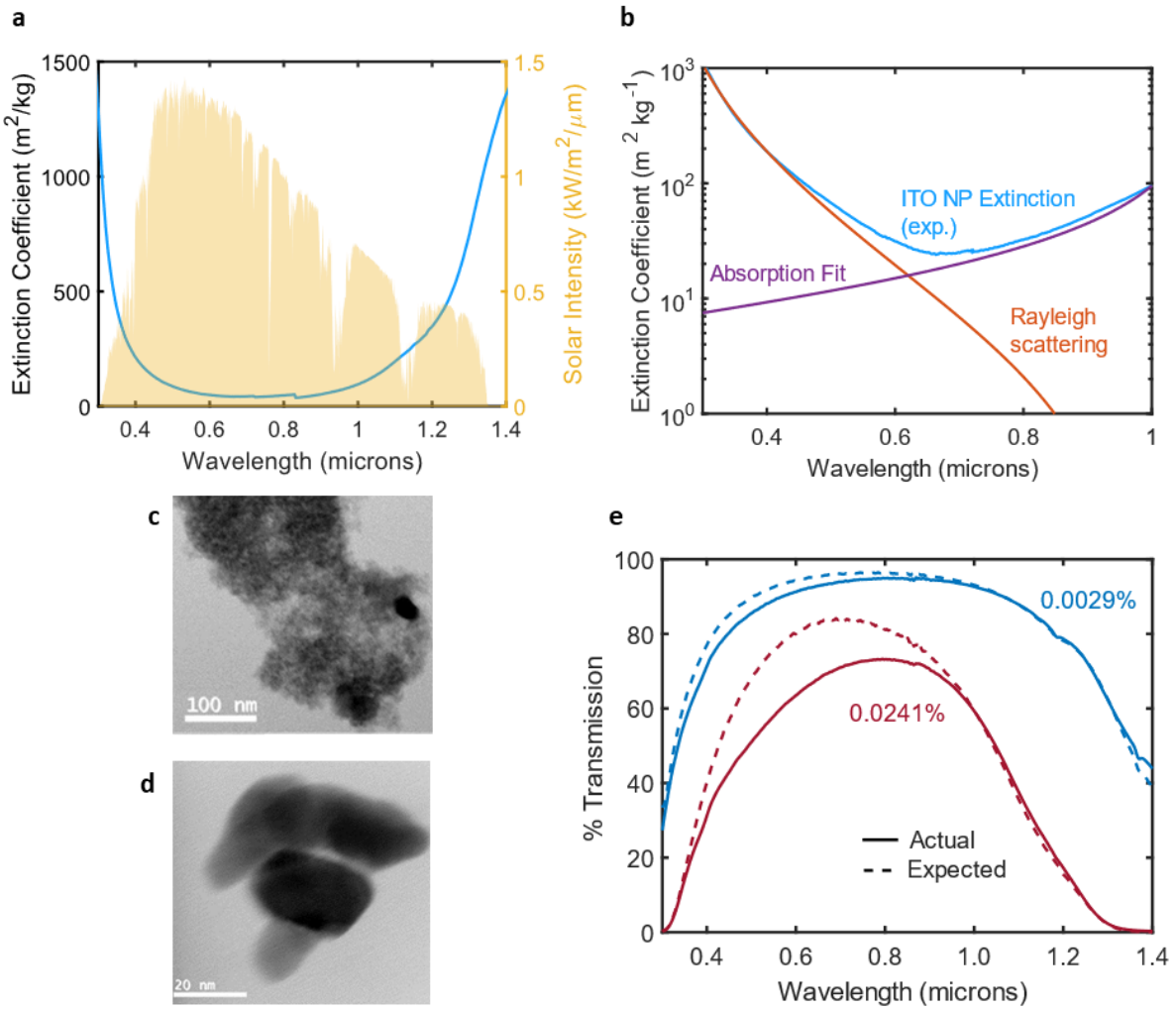


Figure 3.5. Scattering and absorption properties of the ITO NPs. (a) UV-Vis spectra of the ITO NPs dispersed in ethanol. (b) Rayleigh scattering model agrees with measured extinction at short wavelengths. The remaining extinction is attributed to absorption. (c) Transmission spectra of unannealed plasmonic aerogels showing lower transmission than predicted by the Rayleigh model, likely due to increased scattering resulting from NP aggregation. (d) TEM images of ITO NPs (0.024% by volume) in silica aerogel showing evidence of aggregation.

# Chapter 4 : Transparent Refractory Aerogels for Efficient Spectral Control in High-Temperature Solar Power Generation

*The contents of this chapter are based on published work reported in Advanced Functional Materials in 2022.*[12] *The ALD process was developed by collaborators in the Department of Mechanical Engineering, specifically, Andrew J. Gayle and Professor Neil P. Dasgupta.*

## 4.1 Motivation

As discussed in **2.5 Thermal Stability of Aerogels**, silica aerogels undergo sintering and densification at elevated temperatures which degrades their solar transmittance and thermal conductivity.[36,72] The use of a glass envelope in the receiver design mitigates potential issues associated with moisture, ultraviolet (UV) light exposure, and periodic cleaning, leaving thermal stability as a key factor determining the lifetime of the aerogel. A long-term study of more than 150 days examined the degradation of silica aerogels at 600°C and 800°C and considered how degradation affects the receiver efficiency.[36] Based on the rate of degradation, this study concluded that silica aerogels are currently unsuitable for long-term use at these temperatures. Past efforts to stabilize or reinforce the mesoporous structure of transparent aerogels have resulted in significant compromises in transmittance or thermal resistance.[31,63,73] Overcoming this challenge would unlock the full potential of moderate-concentration CST configurations and ultimately lead to large improvements in cost and reliability.

This chapter demonstrates a refractory aerogel that overcomes the thermal stability limitations of silica aerogels while preserving their key functional properties, namely high solar transmittance, and high thermal resistance (Figure 4.1). The aerogels were modified using a recently developed ALD process pioneered by my collaborators in the mechanical engineering department, Andrew J. Gayle and Professor Neil P. Dasgupta.[74] The ALD process deposits a conformal, single-cycle atomic layer deposition (ALD) layer within the high-aspect-ratio pores (>60,000:1) of silica aerogels. The ALD process results in the formation of a refractory aluminum silicate phase which lowers the linear shrinkage rate at 800°C by an order of magnitude compared to the baseline silica aerogel. This thesis thus refers to the modified aerogels as

"refractory", in line with the ASTM definition, which specifies that refractory materials are suitable for applications that are exposed to environments above 538°C, and consistent with previous uses of the term in plasmonics.[75,76] Notably, owing to the large surface area of aerogels, the ALD process introduces a large fraction of aluminum and significantly alters the overall chemical composition of the material, resulting in a Si/Al ratio ~ 3:1. Furthermore, based on direct heat loss measurements at 700°C using the same technique described in **subchapter 3.2.2 Experimental Demonstration of *PEGS***, these aerogels enable the highest solar-to-thermal receiver efficiency at 700°C and 50-100 suns compared to existing solar-selective approaches that have been directly evaluated at ≥700°C. As a result of the improvements enabled by the ALD modification, this material has the potential to serve as an important component in next-generation CST plants.

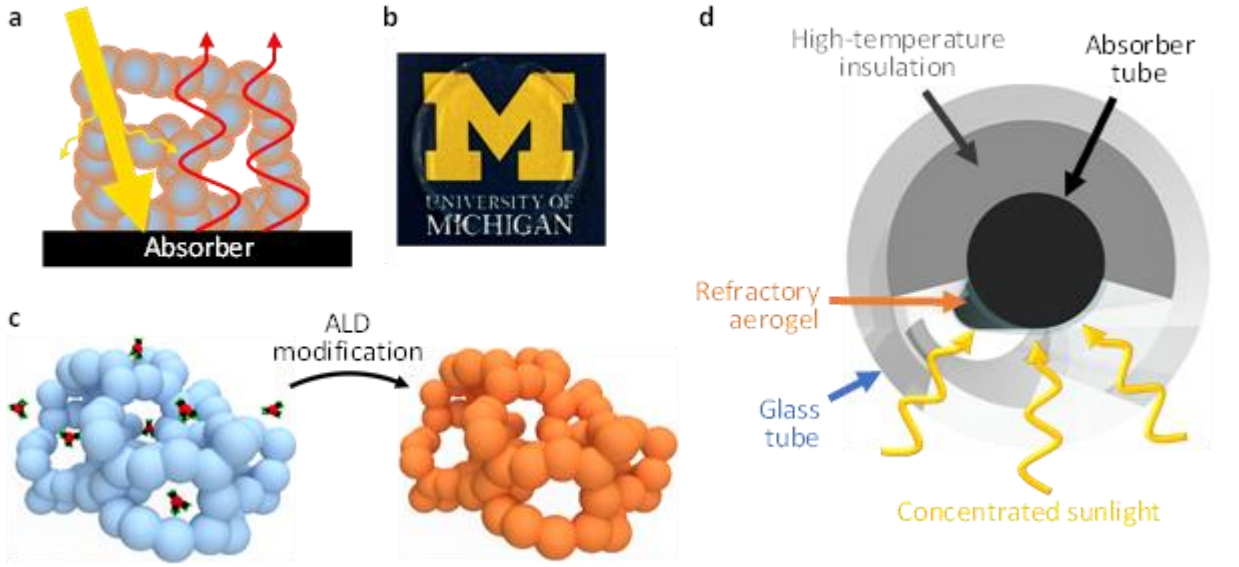


Figure 4.1. Transparent refractory aerogels for solar thermal technologies. (a) A transparent insulating material (TIM) relies on its solar transmittance, thermal opacity, and low thermal conductivity to convert solar radiation into high-temperature heat. (b) Photograph of the refractory aerogel synthesized in this work after aggressive aging (14 days, 800ºC, in air). The "M" is ~1.4 cm. (c) Schematic of the single-cycle ALD modification of a silica aerogel, resulting in the formation of a refractory aerogel. (d) A parabolic trough collector with aerogel insulation covering the solar-incident areas of the black absorber tube.

## 4.2 Results & Discussion

### 4.2.1 Refractory Aerogel Composition

Silica aerogels are first fabricated by the same procedure in **3.2.2 Experimental Demonstration of *PEGS***.

The surface of the aerogels is then modified with a single cycle of ALD, using trimethylaluminum (TMA)

and deionized (DI) water as precursors (Figure 4.1c). The ALD modification was performed in a custom hot-walled, cross-flow ALD reactor.[77] Trimethylaluminum (TMA, 663301, Sigma-Aldrich) and DI water were used as precursors. Both precursors were kept at 37°C, and the deposition temperature was 150°C. Purging was performed using Ultra High Purity Ar (99.999%). A multidose-quasi-static-mode approach was used.[74] The exposure time was 400 s, followed by a purge time of 800 s. TMA was dosed 45 times, followed by 45 DI water doses. One cycle of ALD was performed in each deposition. Before performing ALD, the aerogels were held at a vacuum pressure of ~600 mTorr under constant Ar purging for at least 1 hour at 150°C to ensure the removal of excess water and other adsorbed species. This was followed by 5 DI doses to ensure hydroxyl termination of the aerogel surface.

Although ALD is generally considered to be a powerful method to coat porous materials,[68] it is challenging to uniformly coat aerogel monoliths because of their high surface area and tortuous, long, narrow pores. Furthermore, it is critical to deposit a conformal coating because superficial coatings onto the outer edges of the aerogel result in significant decreases in transmittance.[78] A recent development by my research team addresses these concerns through a multidose-quasi-static-mode ALD process that enables conformal modification of ultra-high-aspect ratio pores (>60,000:1) with excellent precursor utilization.[74] This technique is able to conformally deposit a single cycle (~1-2 Å) of ALD on monolithic silica aerogel discs that are ~27 mm in diameter and ~3 mm in thickness. The ALD process substantially alters the physical and chemical properties of the aerogels, largely due to their high surface area and small characteristic particle size. Following the ALD process, the aerogel density increases from ~175 kg/m$^3$ to ~230 kg/m$^3$, which represents a ~30% mass gain – consistent with the expected growth per cycle for TMA and water on -OH terminated silica.[74]

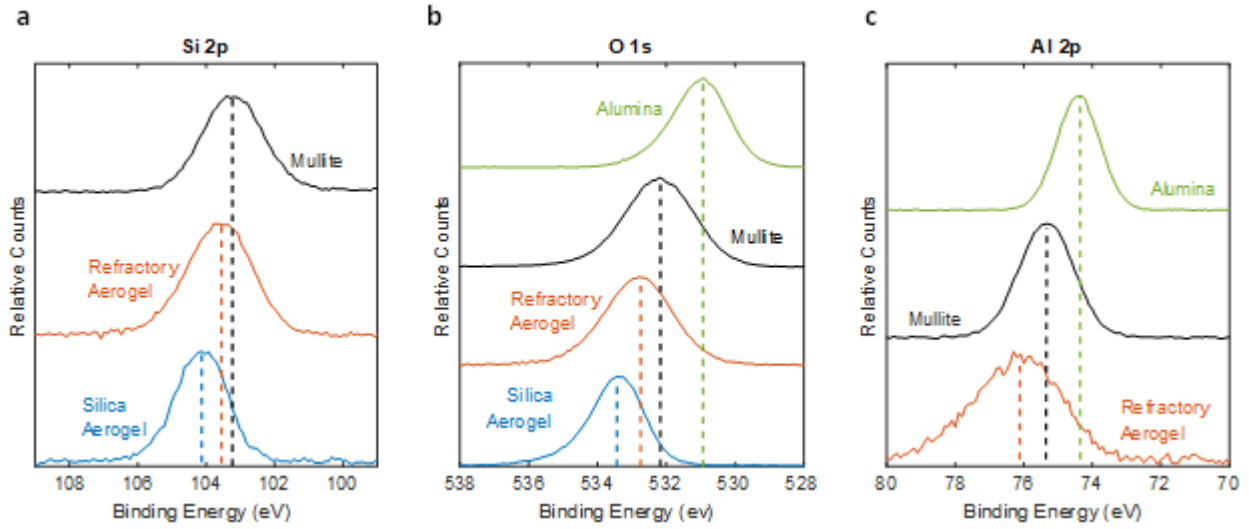


Figure 4.2. Formation of an aluminum silicate aerogel chemistry. XPS characterization of (a) Si 2p, (b) O 1s, and (c) Al 2p orbitals of the aerogels and standard references showing the formation of an aluminum silicate chemistry within the ALD-modified (refractory) aerogel.

X-ray photoelectron spectroscopy (XPS) analysis was performed after the ALD process to investigate changes in binding environment. Although XPS is typically used to measure surface chemistry, the characteristic particle size (~6 nm) of the aerogels in this work is approximately twice the escape depth of photoelectrons in this material system (~2-3.5 nm). Therefore, XPS measurements can probe the overall aerogel chemistry, including bonding environments within the particle interior. To prepare samples for x-ray photoelectron spectroscopy (XPS), the aerogels were crushed using a mortar and pestle to create a powder. A mullite reference powder (2288122, Alpha Aesar) was also analyzed. A bulk ALD $Al_2O_3$ control was prepared on a planar Si substrate. A constant-flow mode was used. The pulse times for TMA and DI water were 0.05 and 0.1 s, respectively, and the purge time was 30 s. 150 cycles were performed, resulting in a film thickness of ~21 nm. Measurements were performed using a Kratos Axis Ultra XPS with a monochromated Al Kα x-ray source (10 mA, 12 kV). The spot size was 700 µm x 300 µm. An electron gun was used to maintain charge neutrality on the surface of each sample. Survey scans (pass energy: 160 eV) were used to quantify the atomic composition of the various samples. Core scans (pass energy: 20 eV) were used to investigate the binding environment of elements in each sample. The binding energies are calibrated to that of adventitious surface carbon (284.8 eV).

Figure 4.2 shows the measured Si 2p, O 1s, and Al 2p binding energies. XPS was also performed on reference mullite ($3Al_2O_3 \cdot 2SiO_2$) powder and bulk ALD alumina ($Al_2O_3$) samples. Figure 4.2a shows that the Si 2p peak of the refractory aerogel is in between that of mullite and the original silica aerogel. The shift of the Si 2p peak to a lower binding energy, as a result of the ALD modification, is consistent with previously reported shifts for increasing Al content in aluminum silicate compounds.[79] Similarly, the O 1s peak of refractory aerogel shifts to a lower binding energy (Figure 4.2b). Notably, the refractory aerogel O 1s peak is differentiated from the alumina peak and cannot be explained by a deconvolution of the spectrum into silica and alumina components. This differentiation relative to bulk alumina is also confirmed by the Al 2p peaks shown in Figure 4.2c.

These XPS data indicate that the ALD process results in the formation of a significant number of Al-O-Si moieties as opposed to the Al-O-Al moieties found in bulk alumina. This highlights a unique aspect of single-cycle ALD modification of an ultra-high surface area aerogel: these Al-O-Si linkages, which are the expected product species for a self-terminating reaction of TMA with hydroxylated amorphous silica,[80] significantly modify the overall composition of the aerogel because of their very high specific area (Table 4.1). Further studies are needed to determine the specific chemical coordination present; nonetheless, these data suggest that the binding environment at the outer surface of the refractory aerogel particles is analogous to that of known aluminum silicates.

### 4.2.2 Improved Thermal Stability

Table 4.1 summarizes the improved thermal stability of the refractory aerogels by highlighting the physical properties of the aerogels before and after aging at 800°C for 14 days. The aerogels were annealed in a tube furnace (MTI Corporation) with a 2°C/min ramp rate in ambient conditions. The holding times for each temperature exclude the time to ramp up and down. The samples were aged under two different conditions. For the first, the aerogels were annealed at 700°C for 24h, followed by two 7 day anneals at 800°C. The aerogels were cycled down to room temperature after each anneal. For the second test, the

samples were aged at 700°C with cycling down to room temperature after 1, 2, 4, 7, and 10 days. This process was repeated at 800°C for a total of 20 days.

Notably, after aging, the refractory aerogel has a larger specific surface area compared to its silica counterpart despite an initial decrease following ALD modification. Surface area was measured using a Micromeritics ASAP 2020 Surface Area and Porosity analyzer. Prior to analysis, the aerogel samples were degassed at 350 ˚C (achieved by a ramp of 20˚C/min) for 8 hours. Brunauer–Emmett–Teller (BET) surface area analysis was conducted at 77 K using the amount of nitrogen adsorbed at various relative vapor pressures between $0.05 < P/P_0 < 0.3$. Total pore volume measurements were taken at a relative vapor pressure, $P/P_0$, of 0.995. The molecular cross-sectional area of nitrogen for the analysis was assumed to be 0.1620 $nm^2$. Similarly, the aged refractory aerogel is less dense and has a higher porosity than its silica counterpart. These data indicate that the ALD modification stabilizes the highly mesoporous structure of the refractory aerogel. This improved structural stability results in a lower room-temperature thermal conductivity (by ~30%) in the aged refractory aerogel compared to its silica counterpart.

In addition to the discrete data points before and after 14 days of aggressive thermal aging, Figure 4.3a shows the linear shrinkage of the aerogels ($\Delta d/d$ where $d$ is the diameter of the aerogel disc) as a function of aging time at two different temperatures. At 700°C, both aerogels experience fast shrinkage within the first ~2 days, followed by slow shrinkage during days 2–10. Previous work using in-situ electron microscopy showed that particle agglomeration is dominant during the first few hours at a given temperature before achieving relative stability.[81] After ~10 days at 700°C, the linear shrinkage is only 8.6% for the refractory aerogel, compared to 16.9% for the silica aerogel. At 800°C, the linear shrinkage for the refractory aerogel increases to 9.0% after one day, likely due to additional particle agglomeration, but it eventually stabilizes to a rate of 0.03%/day between days 17-20. In contrast, the silica aerogel's shrinkage jumps to 18.4% after one day, and it continues to sinter at 800°C with a rate of 0.29%/day (days 17-20). A comparison of the rates obtained during this period indicates that refractory aerogel has superior long-term stability and is likely suitable for operation at temperatures up to 800°C.

**Table 4.1. Physical properties of aerogels before and after aggressive aging.**

| Sample | Density (kg/m$^3$) | Porosity (%) | Surface area (m$^2$/g) | Thermal conductivity (mW/m/K) |
|---|---|---|---|---|
| Refractory, Initial | 230.5 ± 3.2 | 90.0 ± 1.2 | 662 | 18.6 ± 0.9 |
| Refractory, Aged | 333.0 ± 9.0 | 85.7 ± 2.3 | 503 | 30.6 ± 1.5 |
| Silica, Initial | 174.6 ± 2.4 | 92.1 ± 1.3 | 716 | 15.3 ± 0.8 |
| Silica, Aged | 387.6 ± 4.5 | 82.4 ± 1.0 | 481 | 41.4 ± 2.1 |

The improved thermal stability resulting from the ALD modification can be attributed to several possible factors including kinetic, thermodynamic, and mechanical effects. Other studies on alumina-silica aerogels have reported less shrinkage during drying and improved sintering resistance compared to silica aerogels.[63,64,82] Mechanisms proposed to explain the stability include surface modifications inhibiting crystal growth and phase transitions of the aerogel core.[82] However, there are notable differences at a molecular scale relative to the present work. Specifically, Aravind *et al.* synthesized a homogenous alumina-silica aerogel *via* a sol-gel synthesis,[64] whereas the aerogels in this work were surface-modified. Sintering in silica aerogels is commonly attributed to a decrease in viscosity of the solid network at high temperatures which allows for structural relaxation and surface diffusion.[83] Within that theoretical framework, the formation of the aluminum silicate near the surface likely suppresses movement of the underlying silica. Analogous behavior has been observed in heterogeneous catalysis studies where thermally stable ALD "overcoats" slow down diffusion pathways that result in sintering of catalytic nanoparticles.[84] Nonetheless, further investigation is needed to identify the dominant mechanism leading to the observed high-temperature stability behavior in refractory aerogels.

The improvement in thermal stability is also reflected in solar-weighted transmittance measurements (Figure 4.3b). The variation in the transmission data for the refractory aerogel is due to differences in relative humidity during measurements (Figure 4.3c). After annealing at 700°C for 4 days, the transmittance of both aerogel samples increases slightly. Following this initial period, the refractory aerogel maintains a relatively constant solar-weighted transmittance. In contrast, the transmittance of

the silica aerogel decreases as a result of sintering and the formation of larger particles and pores, which leads to increased light scattering.[36] While the difference in solar weighted transmittance is initially ~3%, the gap decreases to <1% by the end of the aging process despite the refractory aerogel being ~8% thicker as measured by multiple caliper measurements. Overall, this time-resolved aging study confirms that the refractory aerogel maintains the high optical transmittance necessary for long-term use in CST applications.

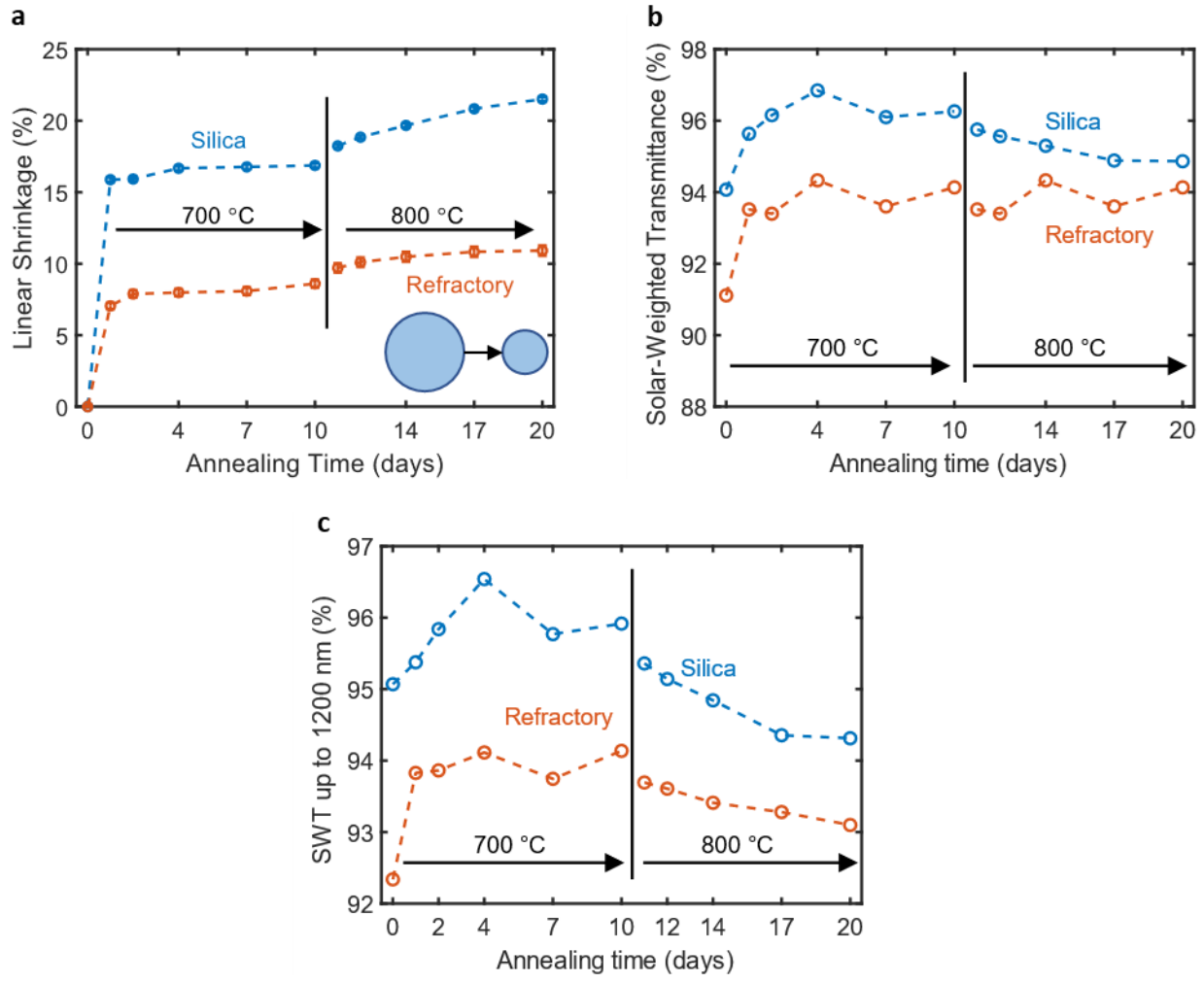


Figure 4.3. Thermal stability of aerogels. (a) Linear shrinkage as a function of aging time demonstrating that the refractory aerogel is stable at 800ºC, while the silica aerogel continues to densify. (b) Solar-weighted transmittance as a function of aging time, showing that while the refractory aerogel has a lower initial transmittance by ~3%, the difference decreases to <1% by the end of the aggressive aging process. (c) Solar-weighted hemispherical transmittance aerogels below 1200 nm.

### 4.2.3 Optical and Heat-Insulating Properties of Aged Refractory Aerogels

With the thermal stability of the refractory aerogels established above, we focus on the optical and thermal properties after aggressive aging and during operation at 700°C, as these characteristics dictate the performance of the aerogels in CST applications. The spectral transmittance of the aged aerogels is shown in Figure 4.4a, and uses the same procedure described in **3.2.2 Experimental Demonstration of *PEGS***. The aged silica and refractory aerogels have nearly identical solar-weighted transmittances of 95% and 94%, respectively. The small decrease in transmittance in the refractory aerogel is mainly due to increased water absorption in the infrared and increased scattering at wavelengths <1 μm associated with a higher refractive index of the solid.

The same heat flux measurement technique discussed in **3.2.2 Experimental Demonstration of *PEGS*** assessed the thermal insulating performance of the aged refractory aerogel by measuring the overall heat loss rate ($Q_{loss}$) as a function of absorber temperature in an evacuated environment. The aerogel is placed on a relatively high emissivity silicon carbide surface, designated as the solar absorber. The heat flux reaching a black sensor in proximity of the cold side of the aerogel is measured as the temperature of the absorber is gradually increased.

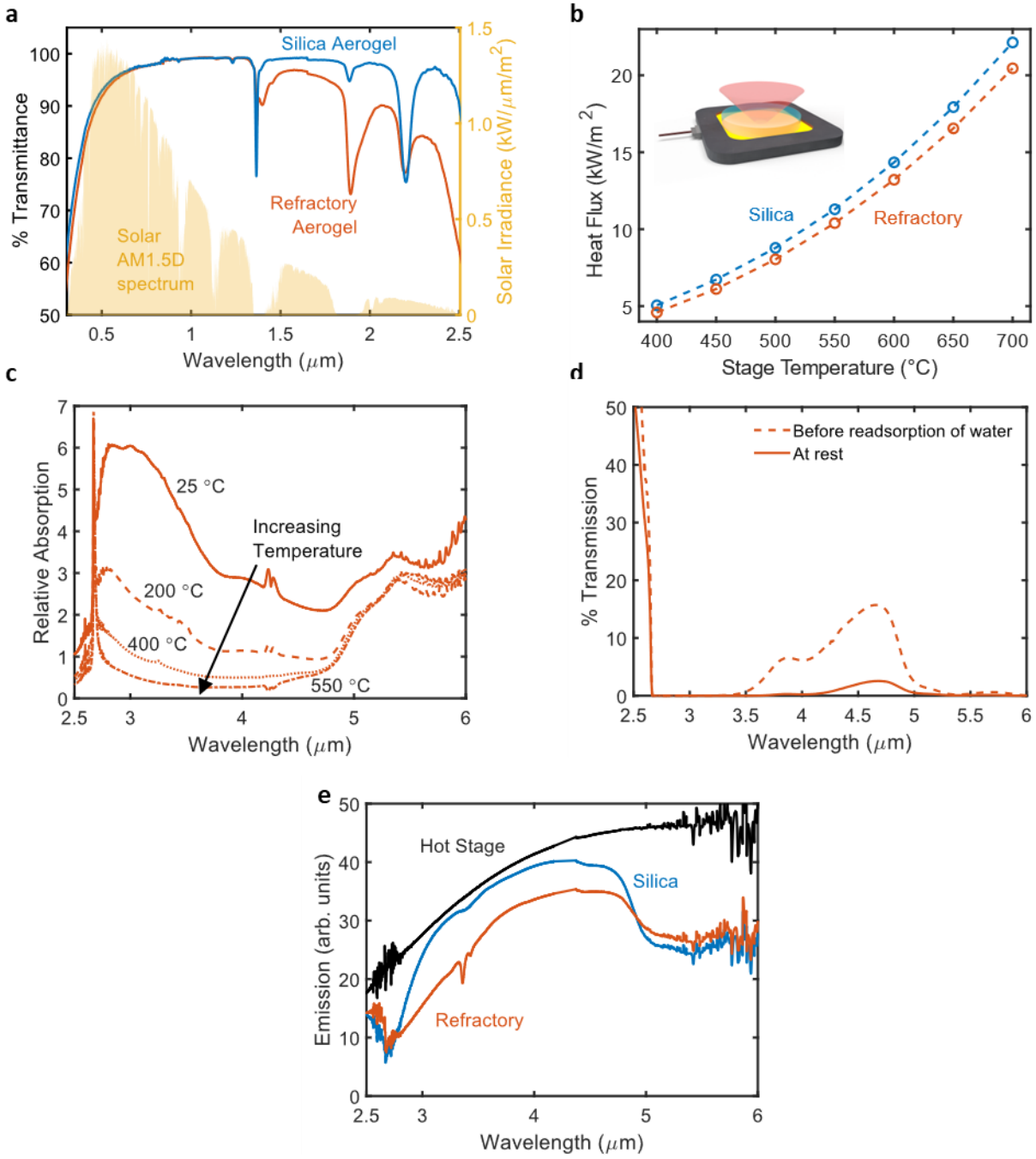


Figure 4.4. Spectral optical and heat transfer properties of aged refractory aerogels. (a) Hemispherical transmittance data of aged aerogels. (b) Measured heat losses from the aerogel-covered SiC heater (*i.e.*, absorber) as a function of stage temperature. Error bars are omitted for clarity as they are all within 3% of the measured values. Inset: schematic showing emission from the hot stage before reaching the heat flux sensor or FTIR detector. The heat flux sensor or FTIR detector are not shown, but are above the silica aerogel. (c) Temperature-dependent DRIFTS showing the effects of adsorbed water on thermal opacity of refractory aerogels as a function of temperature. (d) Relative emission measurements for a 650°C absorber surface temperature in a nitrogen atmosphere. The refractory aerogel suppresses thermal radiation within the IR transparency window of the silica aerogel (3-5 μm).

Figure 4.4b shows that the aged refractory aerogel suppresses heat losses more effectively than its silica counterpart. The effective thermal emittance, $\varepsilon_{app}$ (defined as the ratio of heat losses to the blackbody emissive power at the absorber temperature), decreases from 0.44 to 0.40 at 700°C due to the ALD modification. The difference in heat loss at these high temperatures can be explained by two effects: (1) the refractory aerogel conducts less heat through its solid network, which is consistent with the room-temperature thermal conductivity measurements in Table 1, and (2) there is a reduction in radiative heat transfer associated with an increase in IR absorption within the refractory aerogels. The ALD modification introduces new absorption modes at longer wavelengths due to the stretching (~11.5 μm) and vibrational (~16 μm) modes typical of alumina-silica chemistries. However, absorption at these long wavelengths is not expected to have a significant effect on radiative heat transfer within the aerogel because only a small fraction of the emissive power of a blackbody lies above 10 μm at relevant temperatures (e.g., ~10% at 700°C). Instead, the increased thermal opacity of the aged refractory aerogel is most likely due to adsorbed water, as well as surface hydroxyl groups, which absorb thermal emission within the mid-IR transparency window of pure silica aerogels (3-5 μm).

To study this effect, temperature-dependent diffuse reflectance FTIR (DRIFTS) measurements (Figure 4.4c) were used to measure the presence of water and hydroxyl groups at high temperatures. The aerogel samples were crushed up into a powder using a mortar and pestle. The aerogels were then dispersed into a potassium bromide (KBr) powder with the aerogel consisting of ~5% by mass. A Thermo Fisher Nicolet IS50 FTIR was used with Pike DiffusIR DRIFTS attachment. The DRIFTS accessory was purged with nitrogen. For the temperature-dependent measurements, the aerogel samples were held at each temperature for at least 30 minutes until the spectra remain unchanged from water desorption. The results on powdered samples show that water is still highly present up to 500°C. In contrast, water is not present in the aged silica aerogel due to surface condensation of silanol groups that occurs during annealing.[30] Notably, the refractory aerogel retains its hydrophilic nature even after prolonged aging above 700°C. This behavior is most likely due to the strong Lewis acidity of unsaturated (triply coordinated) surface aluminum sites which strongly adsorb water (-131 kJ/mol).[85] Furthermore, computational studies show that terminating

these sites with hydroxyl groups produces a more stable tetrahedral coordination.[80,86] Although high temperatures may cause eventual dehydroxylation, exposure to humid air can regenerate hydrophilic groups – a phenomenon that we observe in the refractory aerogel (Figure 4.4d).[87] This temperature-dependent water adsorption causes the refractory aerogel to absorb more IR radiation at colder temperatures (Figure 4.4c). These results are consistent with ALD literature showing that even a single cycle of ALD can significantly change the hydrophobicity/philicity of porous substrates.[88]

I further confirm the increase in mid-IR absorption via FTIR thermal emission measurements (Figure 4.4e). The aerogels were placed on the hot stage (Instec) as before (*cf.*, heat flux measurements) but with an infrared transparent KBr window instead of the copper block. Since the KBr lid cannot hold vacuum, the chamber was purged with pure nitrogen. An external port on the Fisher Scientific Nicolet iS50 FTIR was used to capture the emission. All experimental data was normalized to the response curve of a blackbody cavity (Infrared Systems Development Corporation IR-564). Emission through the silica aerogel in the 3–5 μm transparency window is nearly equal to the emission from the hot stage, confirming that the silica aerogel is almost fully transparent over that wavelength range. In contrast, the refractory aerogel suppresses emission within the 3–5 μm wavelength range. The presence of a temperature gradient ($\Delta T$~450°C) along the aerogel thickness likely allows some water to be retained in the colder regions of the refractory aerogel, which acts to block outgoing emission.

Overall, the ALD modification has a minimal negative impact (~1%) on solar transmittance because of its conformality, while having a positive impact (~10%) on thermal opacity and reducing heat losses. In particular, the Al-rich surface of the refractory aerogels has surface sites that strongly adsorb water and appear to be robust at high temperatures. This mechanism represents a new approach for selectively enhancing thermal opacity at high temperatures, which appears to be complementary to existing strategies, including the prior work on plasmon-enhanced greenhouse selectivity (PEGS) using embedded ITO nanoparticles (**Chapter 3**).[13]

### 4.2.4 Receiver Performance

As discussed in **Chapter 1**, the efficiency of a solar receiver is:

$$\eta = \alpha\tau - \frac{Q_{loss}}{CG_s} \tag{1.3}$$

To normalize the performance of selective absorbers to aerogels, selective absorbers are assumed to be used without any transparent covering ($\tau$ = 1) and aerogels are assumed to be used with blackbody absorbers ($\alpha$ = 1). Therefore, the solar absorption is simply $\alpha$ for selective absorbers and $\tau$ for aerogels.

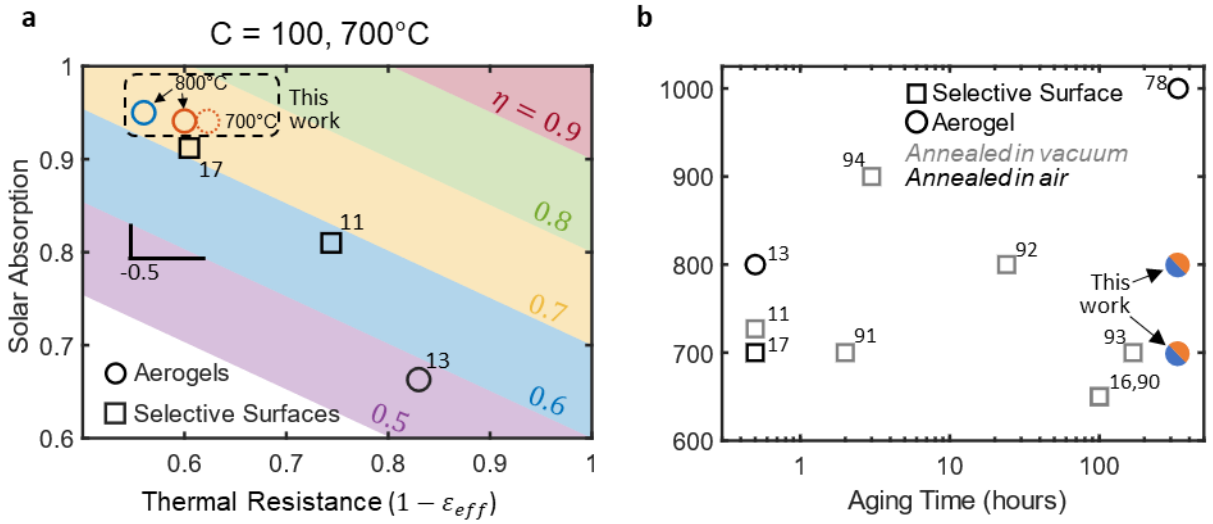


Figure 4.5. Comparison of calculated receiver efficiency at 700°C and corresponding aging conditions. (a) The refractory aerogel achieves a higher receiver efficiency at a concentration ratio (*C*) of 100 suns than all materials and surfaces tested at ≥700°C to date. (b) Aging temperature, time, and environment corresponding to the points in (a) and related high-temperature studies.

Figure 4.5a shows the receiver efficiency of selective surfaces and TIMs at a concentration ratio of 100 suns and an absorber temperature of 700°C. Materials for which the emittance measurements were performed below 700°C are excluded from Figure 4.5a because low temperature measurements can significantly overestimate the high temperature performance.[15,17,89] For context, Figure 4.5b shows the temperature, time, and environment (air vs. vacuum) used to age the various materials.[11,13,16,17,90–94] Importantly, the refractory aerogel in this work has been aged in air and for a significantly longer duration than its counterparts. The receiver efficiency of the refractory aerogel is 75% after aging at 700°C for 10

days. This efficiency is higher than all reports of systems with measured emissivity at ≥700°C to date.[11,13,17] Overall, the refractory aerogel is more transparent (94%) than selective surfaces are absorptive (<91%), leading to a higher receiver efficiency. After aggressive aging at 800°C for 10 days, the receiver efficiency of the refractory aerogel decreases to 74%, while that of its silica counterpart drops to 72%.

Further improvements to aerogel transmittance[22,95] and thermal opacity are likely to lead to even better performance. Figure 4.5a identifies a key takeaway for such future development of solar-selective materials and receivers. At 700°C, the emissive power of a blackbody is ~50 kW/m$^2$. Therefore, at a concentration ratio of 100, the incoming solar flux is approximately twice the outgoing blackbody emissive power. Increasing solar transmittance by 1% or decreasing thermal emittance by 2% will improve efficiency by ~1%. This explains why the slope of the efficiency lines in Figure 4.5a is -0.5. At concentration ratios below 50 suns, it is more important to reduce the thermal emittance, while the opposite is true for concentrations above 50 suns. The acceptable tradeoff is given by $\Delta\varepsilon_{app}/\Delta\tau \geq C/50$, where Δ represents a decrease in the corresponding property. Future work on aerogels for solar trough collectors (C~80) should thus focus on methods to reduce the thermal emittance by at least 1.6 units for each unit lost in solar transmission. Meanwhile, aerogels in lower irradiance systems can prioritize more aggressive thermal insulating strategies over solar transmittance, including *PEGS*[13] or doping of the silica network.[96] Furthermore, the thickness of the aerogel can be optimized to fit the needs of the solar thermal plant, balancing trade-offs between thermal resistance and solar transmittance. Unlike selective surfaces which may require fundamental changes to structure or patterning,[11] the refractory aerogel can be made thicker or thinner depending on the application. Alternatively, the aerogels could be stacked on top of each other to provide more insulation if desirable.[95]

## 4.3 Conclusions

This chapter presents an approach to overcoming temperature-related degradation of aerogels while preserving their extraordinary optical and heat-insulating properties, thus overcoming a major barrier to deploying aerogels in next-generation CST plants. Conformal modification of silica aerogel monoliths via

ALD significantly increases the overall percentage of aluminum (Si/Al ratio ~ 3:1) and produces an aluminum silicate phase that is likely situated near the surface. The resulting refractory aerogel is only slightly less transparent than silica aerogels (94% to 95% after aging), while demonstrating improved high-temperature stability and thermal opacity. At 800°C, the linear shrinkage rate is 0.03% per day for the refractory aerogel compared to 0.29% for the silica aerogel control, demonstrating improved structural stability. Furthermore, among selective surfaces and TIMs that have been tested at ≥700°C, the refractory aerogel can achieve the highest receiver efficiency to date. Given the stable performance at high temperatures, transparent refractory aerogel insulation has the potential to unlock the development of modular, high-efficiency solar thermal plants which could provide on-demand renewable energy at lower costs than existing approaches.

# Chapter 5 : Heat Transfer and Optical Modeling of Ambient-Pressure Aerogel-Insulated Parabolic Receivers

## 5.1 Motivation

Commercial linear receivers operate under vacuum to decrease internal convective losses and to prevent oxidation of the selective absorber (SA). Although SAs achieve excellent performance at moderate to low temperatures, they lack stability at high temperatures and air.[97,98] The vacuum in evacuated annular receivers degrades over time, which results in substantially higher heat losses – both from internal convection and degradation of the selective absorber. Ambient pressure designs have consequently gained interest in recent years, but they require air-stable SAs, which are yet to demonstrated at scale.

Another option is to use mesoporous silica (MS) aerogels to suppress thermal losses. The low thermal conductivity of MS (10 – 200 mW/m/K) enables the absorption and re-emission of thermal radiation to occur at progressively lower temperatures, thus reducing losses (Figure 5.1b and Figure 5.1c). This phenomenon of 'red-shifting' the thermal emission of the absorber allows MS to be used in conjunction with simpler, more stable non-selective, black absorbers. Since MS behaves as a blackbody for wavelengths longer than ~5 μm, its heat flux for those wavelengths is mostly independent of surface emissivity. At wavelengths shorter than 5 μm, though, MS is highly transparent which allows most surface radiation in this region to leave uninhibited. At a relatively low operating temperature of 400°C, this effect is minor as only ~4 kW/m$^2$ (~34%) of a 400°C blackbody's emission exists at wavelengths shorter than 5 μm. A 700°C blackbody, however, emits ~31 kW/m$^2$ at wavelengths <5 μm. The concentration ratio of linear receivers is around 60 suns, or 60 kW/m$^2$, meaning that a 700°C blackbody emits about half of the incident solar power at wavelengths shorter than 5 μm, emphasizing the significance of the infrared transparency of MS.

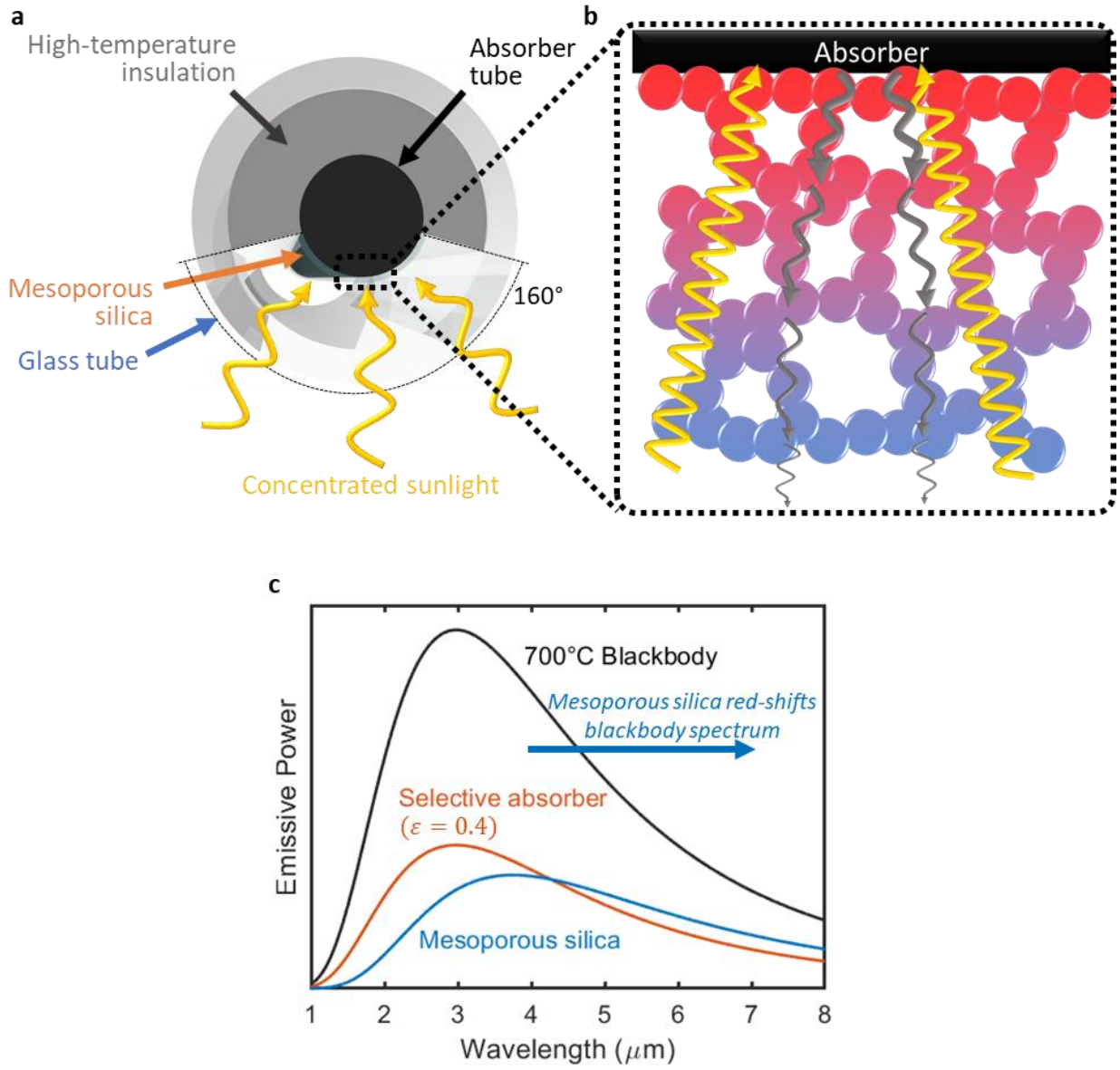


Figure 5.1. Ambient pressure aerogel-based receiver. (a) Rather than an entirely evacuated cylindrical receiver, insulation covers the unconcentrated region of the receiver tube to reduce heat losses leaving an aperture of 160°. At a concentration ratio of 50 (typical of a linear concentrator), this amounts to ~2% loss in incident sunlight for a ~50% reduction in heat losses. (b) A thin insulative layer of mesoporous silica reduces heat losses by forcing thermal radiation to undergo absorption and re-emission. (c) The absorption and re-emission produced a red-shift in emission since its surface temperature is several hundred degrees lower. This is unlike a selective absorber which uses a lower emissivity.

Prior work estimating the performance of MS-based linear receivers has focused primarily on low-temperatures and compared the performance to SAs in high vacuum.[7,99] Other modeling efforts involving MS have largely focused on the impact of MS insulating the non-incident region of an annular

receiver.[100,101] McEnaney *et al.* provided a framework to model the performance of MS at low temperatures against SAs, but for simplicity, their model analyzed a planar receiver configuration. No work to date has compared the performance of SAs to MS in a cylindrical orientation.

The goal of this chapter is to estimate the performance of MS in an ambient-pressure solar receiver design (Figure 5.1a) for linear concentrators. This design limits additional heat losses by insulating the unconcentrated region of the receiver tube.[102] As a test case, the collector performance of this receiver design for PTCs is evaluated by estimating the heat losses using an in-house heat transfer model and the optical efficiency by using a previously established framework.[103] Using correlations for non-radiative conductivity and existing infrared absorption coefficients, the thermal losses are calculated using a rigorous heat transfer model that couples the radiative transfer equation (RTE) and the heat transfer equation (HTE). The modeling suggests methods to improve the performance of MS-based receivers including optimizing the thickness and density of the MS. This chapter also provides a theoretical analysis of our prior investigation into using transparent conducting oxide (TCO) nanoparticles to selectively increase infrared absorption (**Chapter 2**).[13] Further, this chapter compares the performance of MS to SAs by using experimental solar absorptance and thermal emittance data for SAs with good stability at high temperatures. Specifically, there are two air-stable SAs under consideration – the multi-layer cermet absorber for 400 and 550°C developed by CIEMAT (Spain) and the $MnFe_2O_4$ nanoparticle paint absorber developed by Xiaoxin Wang *et al* for 700°C.[104] It is important to note that the spectral emissivity of the paint was measured at room temperature which likely underestimates its actual thermal emittance at 700°C.[15,89] This chapter shows that MS-insulated receivers are superior to selective surfaces at temperatures greater than 550°C when operated near ambient pressure. Additional improvements, such as the use of selectively absorptive nanoparticles, are required for MS to surpass SAs at moderate temperatures.

## 5.2 Modeling Selective Absorbers

The heat loss model for SAs uses a parallel heat transfer model that treats radiation and conduction/convection as independent heat transfer modes (Figure 5.2a). This is an accurate assumption

because the air annulus is almost entirely transparent to thermal radiation, and the glass tube has a relatively high thermal conductivity. Therefore, there is no coupling of radiative and conductive heat within the air annular gap or through the outer glass tube. Relevant material and heat transfer properties used in this analysis are provided in Table 5.1:

Table 5.1 Relevant properties of the receiver design.

| Property | Value |
|---|---|
| **Glass conductivity, $k_{glass}$** | 2.0 W/m/K |
| **External convection coefficient, $h$** | 15 W/m$^2$ |
| **Conductivity of high-temp insulation, $k_{insulation}$** | 33 mW/m/K |
| **Ambient temperature, $T_\infty$** | 22°C |
| **Outer radius of absorber tube, $r_{absorber}$** | 35 mm |
| **Inner radius of glass tube, $r_{glass,i}$** | 55 mm |
| **Outer radius of glass tube, $r_{glass,o}$** | 60 mm |
| **Aperture angle** | 160° |
| **Solar weighted absorptance, $\alpha$** | 0.96 (400 & 550°C)<br>0.92 (700°C) |
| **Solar-weighted transmittance of glass** | 0.97 |

For an SA-based receiver at ambient pressure, the heat transfer model is a simple resistance network (Figure 5.2a). The total heat loss in the system is determined numerically by equating the heat loss at the boundaries of each resistance medium, represented as nodes in the network.

$$Q_{losses} = Q_{participating} + Q_{c,inner} = Q_{glass} = Q_{outer} \tag{5.1}$$

Specifically, the model considers the radiative, $Q_{r,inner}$, and conductive, $Q_{c,inner}$, heat fluxes from the absorber to the glass tube, which is either occupied by vacuum or air. This is set equal to the heat flux through the glass $Q_{glass}$, and the heat flux from the glass's outer surface to the environment, $Q_{outer}$. The radiative exchange between the selective surface and the glass tube, $Q_{r,inner}$, is modeled with Equation 5.2, which describes the radiative transfer between infinite concentric cylinders with one opaque and one semi-transparent surface:

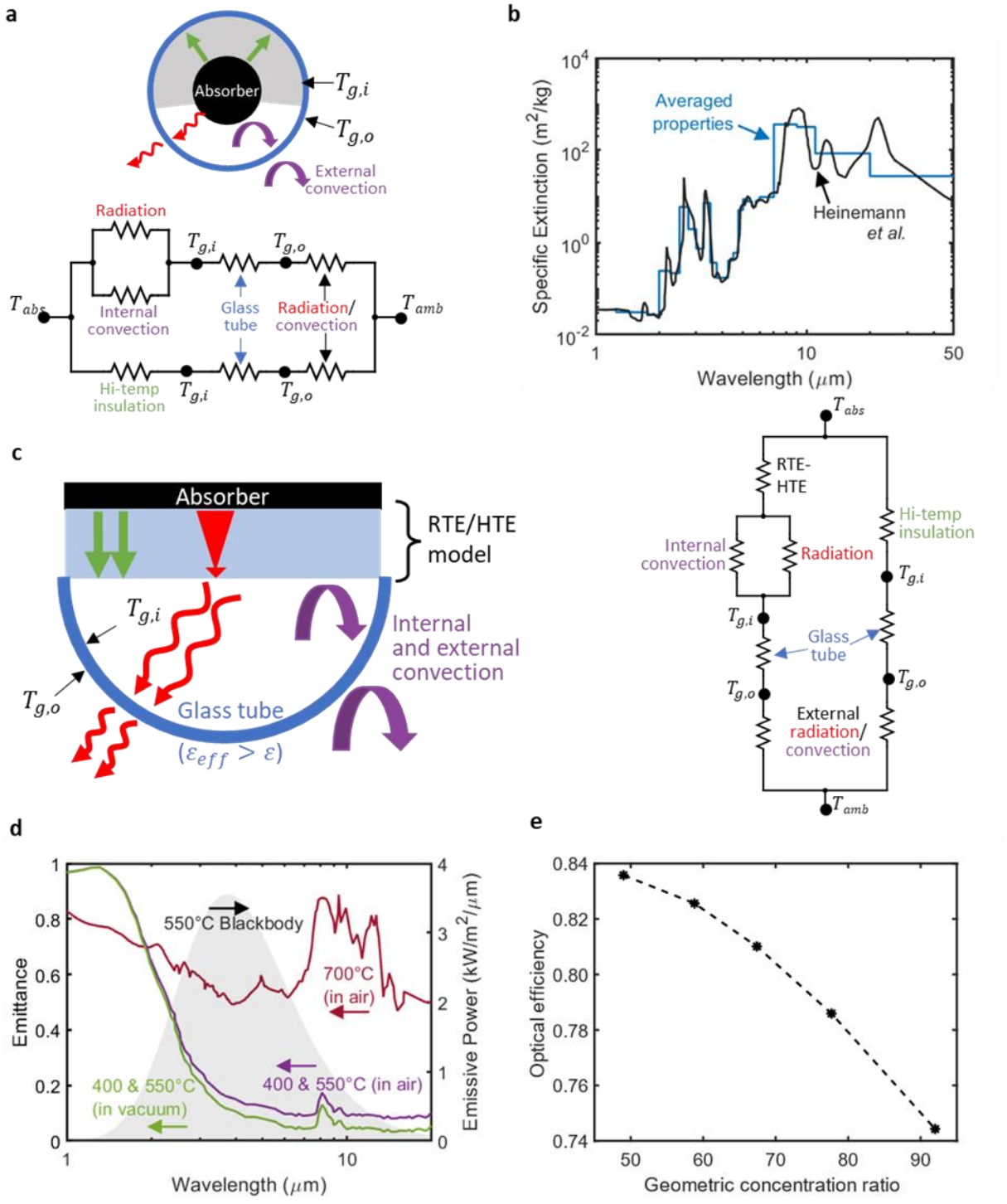


Figure 5.2. Heat loss and optical modeling. (a) The heat losses from an SA-based receiver are modeled with a simple resistance network. (b) The spectral properties of all materials involved are averaged within 25 distinct bands ranging from 1 μm to 100 μm. The figure is an example of averaging the extinction coefficients of MS. (c) Heat losses through an MS-based receiver are estimated with the same resistance network, except the heat losses in the exposed region are estimated with a rigorous RTE-HTE model that couples conductive and radiative contributions through the MS. (d) Spectral emissivities of the SAs used in this analysis. For reference, a 550°C blackbody emission spectrum is provided. (e) Optical efficiency of the mirror focusing system.

$$Q_{r,inner} = \frac{r_{glass,i}}{r_{absorber}} * \frac{\varepsilon_{glass}\sigma T_{absorber}^4 + \left(\rho_{glass} - 1\right)\sigma T_{glass,i}^4}{\rho_{glass} + \frac{r_{glass,i}}{r_{absorber}}\left(1 - \rho_{glass}\right)\left(1 + \frac{1 - \varepsilon_{absorber}}{\varepsilon_{absorber}}\right)} \tag{5.2}$$

where $\sigma$ is the Stefan-Boltzmann constant, $T_{absorber}$ is the temperature of the solar absorber, $T_{glass,i}$ is the temperature of the inner surface of the glass tube, $\varepsilon_{absorber}$ is the thermal emittance of the solar absorber, $\varepsilon_{glass}$ is the emittance of the glass tube, $\rho_{glass}$ is the reflectance of the glass tube, and $r$ is the radius of the previously defined surface (absorber and inner glass). The accuracy of the model is improved by splitting the entire thermal radiation spectrum into 25 bands where each of the spectrally-dependent properties is averaged (Figure 5.2b). All radiative properties are averaged within each band. This is especially important at high temperatures because glass is transparent at wavelengths < 3 μm. Using a gray or opaque approximation will significantly underestimate the heat losses at these short wavelengths. Equation 5.2, in fact, accounts for the heat losses that are transmitted through the semi-transparent glass tube with transmittance, $\tau_g$. Thus, the participating radiative heat flux that ultimately defines the temperature nodes of the model is provided in Equation 5.3:

$$Q_{participating} = Q_{r,inner} - \varepsilon_{absorber}\sigma T_{absorber}^4 \tau_{glass} * 2\pi r_{absorber} \tag{5.3}$$

The convective losses within the receiver annulus gap, $Q_{c,inner}$, are modeled with the Raithby and Hollands correlation for the free convection heat transfer inside concentric cylinders to compute the effective conductivity of the air, $k_{eff}$:[32]

$$Q_{c,inner} = \frac{k_{eff}\left(T_{absorber} - T_{glass,i}\right)}{\ln\left(\frac{r_{glass,i}}{r_{absorber}}\right)} \tag{5.4}$$

The next node to calculate the heat flux for is the conduction through the glass tube:

$$Q_{glass} = \frac{k_{glass}\left(T_{glass,i} - T_{glass,o}\right)}{\ln\left(\frac{r_{glass,o}}{r_{glass,i}}\right)} \tag{5.5}$$

where $k_{glass}$ is the thermal conductivity of the glass tube (assumed to be 2 W/m/K) and $T_{glass,o}$ is the temperature of the outer surface of the glass tube. Finally, the model computes heat losses from the outer surface of the glass tube using convection and radiative boundary conditions:

$$Q_{r,outer} = \varepsilon_{glass}\sigma T_{glass,o}^4 - \sigma T_\infty^4 \tag{5.6}$$

$$Q_{convection} = h(T_{glass,o} - T_\infty) \tag{5.7}$$

where $T_\infty$ is the temperature of the ambient environment (22°C) and $h$ is the convective heat transfer coefficient (15 W/m/K). The following series of equations (Equations 5.8-5.10) is solved to determine the three independent variables: $Q$, $T_{glass,i}$, and $T_{glass,o}$.

$$\boldsymbol{Q} = \frac{r_{glass,i}}{r_{absorber}} * \frac{\varepsilon_{glass}\sigma T_{absorber}^4 + \left(\rho_{glass} - 1\right)\sigma \boldsymbol{T_{glass,i}^4}}{\rho_{glass} + \frac{r_{glass,i}}{r_{absorber}}\left(1 - \rho_{glass}\right)\left(1 + \frac{1 - \varepsilon_{absorber}}{\varepsilon_{absorber}}\right)} - 2\pi r_{absorber}\varepsilon_{absorber}\sigma T_{absorber}^4 \tau_{glass} + \frac{k_{eff}\left(T_{absorber} - \boldsymbol{T_{glass,i}}\right)}{\ln\left(\frac{r_{glass,i}}{r_{absorber}}\right)} \tag{5.8}$$

$$\boldsymbol{Q} = \frac{k_{glass}\left(\boldsymbol{T_{glass,i}} - \boldsymbol{T_{glass,o}}\right)}{\ln\left(\frac{r_{glass,o}}{r_{glass,i}}\right)} \tag{5.9}$$

$$\boldsymbol{Q} = \varepsilon_{glass}\sigma \boldsymbol{T_{glass,o}^4} - \sigma T_\infty^4 + h(\boldsymbol{T_{glass,o}} - T_\infty) \tag{5.10}$$

Lastly, the transmitted (non-participating) radiation is added to get the heat losses:

$$Q_{exposed} = Q + 2\pi r_{absorber}\varepsilon_{absorber}\sigma T_{absorber}^4 \tau_{glass} \tag{5.11}$$

These estimated heat losses, however, are only for the exposed (lower half) of the solar receiver. The heat losses through the opaque region are estimated by adding up the resistances in series between the solar absorber and the ambient temperature:

$$Q_{covered} = \frac{T_{absorber} - T_{\infty}}{\frac{1}{hr_{glass,o}} + \frac{\ln\left(\frac{r_{glass,o}}{r_{glass,i}}\right)}{k_{glass}} + \frac{\ln\left(\frac{r_{glass,i}}{r_{absorber}}\right)}{k_{insulation}}} \tag{5.12}$$

where $k_{insulation}$ is the conductivity of the insulation (estimated to be 33 mW/m/K). Finally, the total heat losses are calculated with Equation 5.13 treats each of the heat loss problems in parallel:

$$Q_{total} = Q_{exposed} * \left(\frac{160}{360}\right) + Q_{covered} * \left(\frac{200}{360}\right) \tag{5.13}$$

## 5.3 Modeling Mesoporous Silica

Unlike an SA-based receiver, estimating the heat losses through a participating medium, such as MS, is a nontrivial task since it requires solving the radiative transfer equation (RTE, Equation 5.14) in conjunction with the heat transfer equation (HTE, Equation 5.15):

$$\frac{dI_{\nu}}{d\boldsymbol{s}} = -\beta_{\nu} I_{\nu} + (1 - \sigma_{\nu})\beta_{\nu} I_{\nu} + \frac{\beta_{\nu}\sigma_{\nu}}{4\pi} \int_{4\pi} I_{\nu}(\boldsymbol{s}_i) d\Omega_i \tag{5.14}$$

$$\nabla \cdot (k \nabla T) = \nabla \cdot q_r \tag{5.15}$$

The RTE is computationally expensive to solve because it is an integro-differential equation. To make the calculation tractable, the model splits the thermal radiation spectrum into the 25 bands as for the SA-based receivers and again averages the inputs for each band (Figure 5.2b). Since scattering is negligible for wavelengths above 1 μm, the scattering albedo, $\sigma_{\nu}$, is set to 0 (*i.e.*, all attenuation is due to absorption). These values are consistent with previous literature.[33]

The model solves the heat flux between each node and iterates the calculation until it converges. Here, the RTE/HTE model is solved in a planar configuration (Figure 5.3) because it is impossible to analytically estimate the heat losses in a participating medium in a cylindrical orientation when accounting for both conduction and radiation. A discussion of this is provided in Michael Modest's *Radiative Heat Transfer* textbook.[34] To account for the cylindrical orientation, the model makes two adjustments. First, the emissivity of the outer glass tube is increased by taking into account the increased area compared to a planar configuration (Figure 5.2). Equation 5.16 provides the effective emissivity of a semi-transparent boundary when accounting for increased surface area:

$$\varepsilon_{eff} = \frac{\varepsilon_{glass}}{\frac{r_{absorber}}{r_{glass,i}} + \left(\tau_{glass} + \varepsilon_{glass}\right)\left(1 - \frac{r_{absorber}}{r_{glass,i}}\right)} \tag{5.16}$$

Secondly, the model accounts for the increase in insulation area by multiplying the computed the heat losses by an area adjustment factor. Fourier's law predicts an increase in heat losses for cylindrical orientations compared to planar ones for a given thickness. The model simply multiplies its predicted heat losses in a planar configuration by the percent increase predicted by Fourier's law. Work by Perlmutter and Howell shows this approximation also works for radiation, confirming the validity of this assumption for our analysis.

The outer surface of the MS is also subject to convective losses from the air present in the annulus which is calculated with the correlation developed by Raithby and Hollands.[32] The calculations for the heat fluxes through the glass tube, and the boundary conditions are identical to the calculations for the SA-based receiver. Lastly, the model estimates the total heat losses out of the receiver the same way as for the SA-based receivers by using Equation 2.13, where $Q_{exposed}$ is the predicted heat losses from the RTE-HTE model.

The process of solving the RTE-HTE model is an iterative one with the following steps:

1. A temperature profile is guessed with a given number of nodes (usually greater than 50)
2. The RTE is solved to ultimately compute the divergence in radiative heat flux at each node

3. The HTE is solved using both the contributions of conduction and radiation at each node.
4. A new temperature profile is produced from solving the HTE.
5. The temperature profile of the glass tube is calculated from boundary conditions on each side of the glass tube
6. The process is repeated until a specified tolerance is reached.

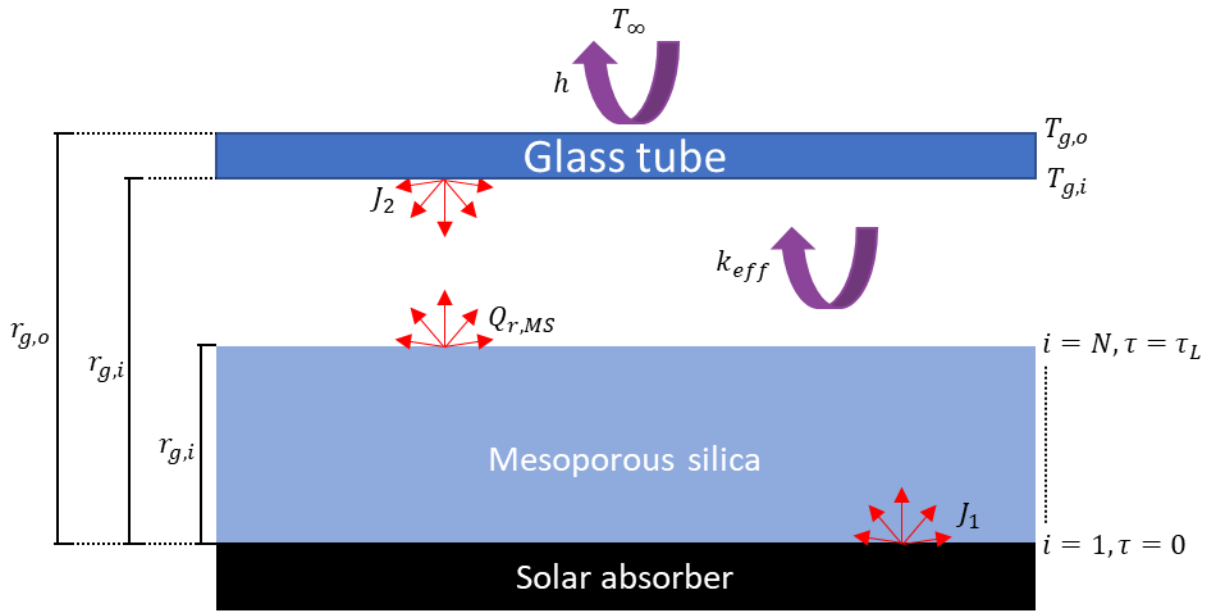


Figure 5.3. Diagram of RTE-HTE model. Our simulations model a planar mesoporous silica slab in physical contact with a solar absorber separated from a glass tube by a distance $\boldsymbol{L = r_{g,o} - r_{g,i}}$.

For the RTE, there are three equations that need to be solved in every iteration. All the following equations and steps are also provided in Chapter 14 of Michael Modest's *Radiative Heat Transfer* textbook. The first property to solve for is the incident radiation, $G$:

$$G(\tau) = 2J_1E_2(\tau) + 2J_2E_2(\tau - \tau_L) + 2\pi\int_0^{\tau} I_b(\tau')E_1(\tau - \tau')d\tau' + 2\pi\int_{\tau}^{\tau_L} I_b(\tau')E_1(\tau_L - \tau')d\tau' \quad (2.17)$$

where $J$ is the radiosity of one of the surfaces, $E_n$ is the exponential integral of order $n$, $I$ is the radiative intensity, $\tau$ is the optical thickness of the node, and $\tau_L$ is the optical thickness of the radiative band. Once G is solved for, the heat radiative flux, $q_r$, at each node is computed with Equation 2.18 which is nearly identical to Equation 2.17:

$$q_r(\tau) = 2J_1E_3(\tau) + 2J_2E_3(\tau - \tau_L) + 2\pi\int_0^{\tau} I_b(\tau')E_2(\tau - \tau')d\tau' + 2\pi\int_{\tau}^{\tau_L} I_b(\tau')E_2(\tau_L - \tau')d\tau' \quad (2.18)$$

except that each of the exponential integrals is of one order higher. Next, the divergence of radiative flux is computed with Equation 2.19:

$$\frac{dq_r}{dz} = \sum_{n=1}^{N} \kappa_n(4\pi I_{b,n} - G_n) \quad (2.19)$$

where $\kappa$ is the average absorption coefficient within each band, $n$. In our model, we broke up the thermal radiation spectrum into 25 bands ($N$ = 25, Figure 5.2b). Once the RTE is solved, the HTE (Equation 2.15) is solved with the finite difference method to generate the new temperature profile (Equation 2.20):

$$T(i) = \frac{\frac{dq}{dz}(i) * \frac{\Delta z}{k_{MS}} - T(i-1) - T(i+1)}{-2} \quad (S.20)$$

where $T(i)$ is the temperature at a given node, $\Delta z$ is the physical spacing between each node, and $k_{MS}$ is the thermal conductivity of mesoporous silica. For the node at the boundary of the hot solar absorber, the temperature is held constant. At the final node (at the air interface), a heat balance is performed on all absorbed radiation and conducted heat at the node since the finite difference method cannot be used on it.

Once the RTE-HTE is solved, the glass temperature profile is computed using the following energy balances for the hot and cold sides of the glass tube, respectively:

$$\sigma\varepsilon_{glass}\boldsymbol{T}_{\boldsymbol{glass,i}}^{\boldsymbol{4}} + k_{glass} * \frac{\boldsymbol{T}_{\boldsymbol{glass,i}} - T_{glass,o}}{r_{glass,i} * \ln\left(\frac{r_{glass,o}}{r_{glass,i}}\right)} = \varepsilon_{glass}Q_{r,MS}\frac{r_{MS}}{r_{glass,i}} + k_{eff}\frac{\left(T(N) - \boldsymbol{T}_{\boldsymbol{glass,i}}\right)}{r_{g,i}\ln\left(\frac{r_{glass,i}}{r_{MS}}\right)} \quad (2.21)$$

$$\sigma\varepsilon_g\boldsymbol{T}_{\boldsymbol{g,o}}^{\boldsymbol{4}} + h\left(\boldsymbol{T}_{\boldsymbol{g,o}} - T_\infty\right) = \varepsilon_g T_\infty^4 + k_g\frac{T_{g,i} - \boldsymbol{T}_{\boldsymbol{g,o}}}{r_{g,i} * \ln\left(\frac{r_{g,o}}{r_{g,i}}\right)} \quad (2.22)$$

where $T_{g,i}$ is the temperature at the inner (hot) surface of the glass tube, $T_{g,o}$ is the temperature at the outer (cold) surface of the glass tube, $\varepsilon_g$ is the emissivity of glass, $k_g$ is the conductivity of glass, $Q_{r,MS}$ is the radiative heat flux leaving mesoporous silica, and $T_\infty$ is the temperature of the surroundings. The left sides of the equations are energy out of the glass boundary, whereas the right sides are energy into the glass boundary. We again split up the radiative terms into 25 bands and average the glass emittance values for each band. The radiative terms are then summations of the 25 bands. Once a new temperature profile of the glass tube is calculated, another iteration of the RTE-HTE model begins with solving Equation 2.17. This process is repeated until a specified tolerance is met.

### 5.3.1 Adjusting Planar Heat Losses for a Cylindrical Receiver

Fourier's Law predicts higher heat losses for annular cylinders compared to infinite planes because the area of heat transfer increases with increasing radius. Simply multiplying by the increase in area, however, overestimates the heat losses (Figure 5.4a). An alternative way to convert planar heat losses to cylindrical is to use the ratio of cylindrical and planar heat losses (Equation 2.25).

$$q_{planar} = k * \frac{\Delta T}{r_o - r_i} \tag{2.23}$$

$$q_{cylindrical} = k * \frac{\Delta T}{r_i \ln\left(\frac{r_o}{r_i}\right)} \tag{2.24}$$

$$\theta = \frac{r_i \ln\left(\frac{r_o}{r_i}\right)}{r_o - r_i} \tag{2.25}$$

Not only is this an exact way to adjust conductive heat losses, but fortunately, it is also an accurate way to convert radiative losses from planar to cylindrical (Figure 5.4). Radiative heat losses will also increase relatively in cylindrical compared to planar. Perlmutter and Howell used a Monte Carlo model to calculate the radiative heat flux between two infinite cylinders at multiple different radii ratios. For a ratio of $r_o/r_i$ = 0.9, the increase in radiative heat flux compared to what is predicted by Fourier's Law is within 5% at all thicknesses. In this analysis, $r_o/r_i$ ranges from 0.74 (12 mm thick MS) to 0.92 (3 mm thick MS). As seen in Figure 5.4, using Fourier's Law to estimate the increase in radiative losses is likely accurate to within 5-

10% regardless of the optical thickness of the MS. Therefore, to adjust the heat losses the model predicts, a factor, $\theta$, is used to increase the heat losses due to the cylindrical orientation. It is important to note that the error in this approximation is likely within a few percent of the real value.

$$q_{predicted} = q_{RTE-HTE} * \theta \tag{2.26}$$

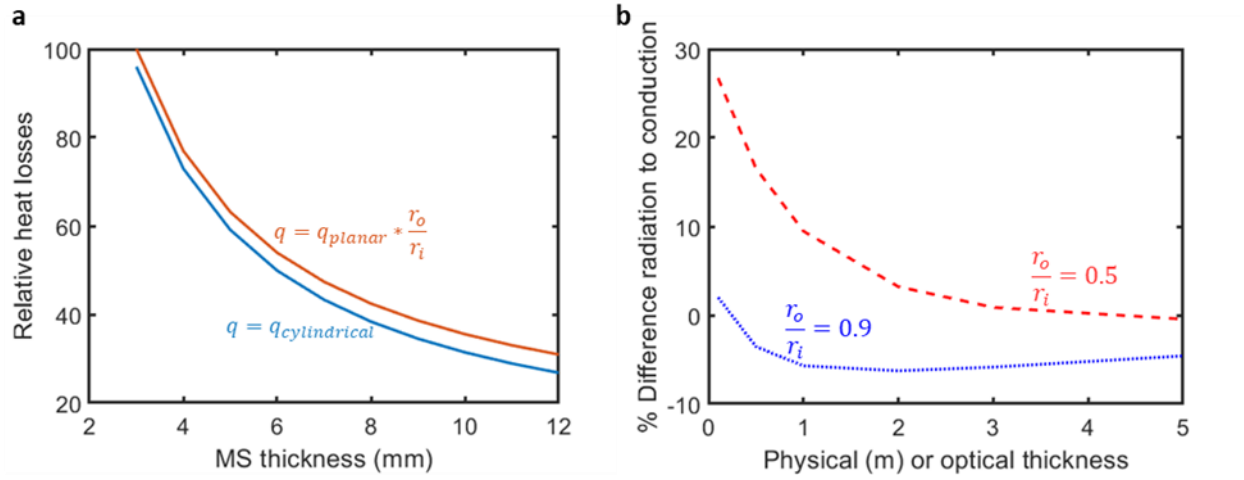


Figure 5.4. Adjusting planar heat fluxes to accurately predict cylindrical fluxes. (a) Simply multiplying the heat fluxes predicted by Fourier's Law by the increase in area overpredicts the heat losses. The error is as high as 20% at an MS thickness of 12 mm. (b) The increase in radiative heat flux for infinite cylinders is nearly the same as the increase for infinite planes (generally within 10%).

## 5.4 Solar Collector Performance

The efficiency of a solar collector, $\eta_{collector}$, is the product of the optical efficiency ($\eta_{optical}$) of the concentrating mirrors and the receiver efficiency ($\eta_{receiver}$):

$$\eta_{collector} = \eta_{optical} * \eta_{receiver} = \eta_{optical} * \left(\alpha\tau - \frac{Q_{loss}}{C G_s}\right) \tag{2.27}$$

where $\alpha$ is the solar-weighted absorptance of the absorber, $\tau$ is the solar-weighted transmittance of the insulation (glass tube and MS), $Q_{loss}$ is the thermal losses per area, $C$ is the solar concentration ratio, and $G_s$ is the standard AM1.5D incident solar power (1,000 W/m$^2$). For SAs, $\alpha$ is calculated from existing absorptance measurements, but for MS, a value of 1 is assumed since there are multiple designs for achieving near-perfect solar absorption such as carbon nanotube and plasmonic arrays. For $\tau$, it is set to

the transmittance of the glass tube (0.97) for SAs, and it is the product of the glass tube and MS transmittances for MS-based receivers.

The optical efficiency of a parabolic trough collector is ~75% because there are several sources of efficiency loss including tracking errors and slope errors.[13] These errors make it increasingly difficult to focus sunlight for longer focal lengths which are required for higher concentration ratios (Figure 5.2e). On the other hand, increasing the concentration ratio increases the receiver because heat losses constitute a smaller fraction of the incident sunlight. There is thus a tradeoff for increasing the concentration ratio.

The transmittance of MS is highly dependent on its nanostructure.[35] For wavelengths <1 μm where 72% of the solar spectrum exists, MS is non-absorptive. Rather, the pores and individual silica particles scatter light. It is therefore difficult to estimate the extinction of MS with respect to density. Previous work has estimated the transmittance of MS using experimentally determined scattering radii,[4] but this is an effective scattering radius and is therefore not predictive. Fortunately, there is little dependence on solar transparency with increasing density. As the density of MS increases, the scattering decreases as the pores shrink. On the other hand, the reflectance of MS increases with increasing density as the index of refraction approaches that of pure silica at higher densities. The decrease in scattering combined with the increase in reflectance creates minimal differences in the transparency for MS of varying density. The work from **Chapter 4** demonstrates the change in MS transparency was <1% in the range of 170 – 400 kg/m$^3$. This work assumes the trend can extrapolate to 700 kg/m$^3$, but this assumption likely fails at very high densities (>1,000 kg/m$^3$) when reflectance becomes increasingly large. To understand the performance of optimized MS, this work uses the correlated transmittance values from Zhao *et. al* to estimate the transmittance of MS for a given thickness at any density from 110 kg/m$^3$ to 700 kg/m$^3$.

## 5.5 Results: Methods to Improve the Insulation Properties of MS-based Receivers

### 5.5.1 Optimizing Density

One way to increase the infrared absorption and reduce thermal radiative losses is to increase the density of the MS. However, there is a tradeoff as increasing the density also increases the thermal conductivity

because conduction through the solid silica backbone will increase. To predict the non-radiative thermal conductivity of the MS, this chapter uses the model developed by D. Dan *et al*.[36] Figure 5.5a shows the effect of MS density on total heat losses at 700°C. The first conclusion is that there is an optimal density for minimizing the heat flux which occurs anywhere between 300 – 700 kg/m$^3$ depending on the thickness. These densities are much greater than the densities of MS typically designed for transparent insulators (<170 kg/m$^3$),[3,4,33] suggesting that future designs of MS for high temperature operation should use higher densities. Secondly, the optimal density increases with increasing MS thickness. Denser MS increases heat losses due to conduction, but a thicker layer of MS can negate some of the increased conductive losses by increasing the diffusion length. This tradeoff allows the receiver to benefit from the reduced radiative losses of denser MS while maintaining similar losses due to conduction. Although not shown for conciseness, this trend is consistent with absorber temperatures of 400 and 550°C, but at lower densities since radiation is less significant at lower temperatures.

The heat losses through MS are mostly independent of its nanostructure because conduction plays such a minor role in the overall heat losses of the receiver. Therefore, the results here can be used as a predictive guide for the future development of MS for CST applications.

### 5.5.2 Decreasing Heat Losses with TCOs

Although increasing the density and thickness of MS decreases heat losses, the infrared transparency of MS is the primary heat loss pathway. Previous methods to address the infrared transparency of MS include the use of opacifier fibers such as carbon, iron oxide, alumina, and titania.[37,38] These opacifiers, however, were broadband opacifiers that also made the MS opaque to solar radiation – thus rendering the multicomponent insulation unusable in CST applications. **Chapter 3** investigated the use of transparent conducting oxide (TCO) nanoparticles (NPs) to selectively increase infrared absorption without sacrificing solar transparency,[5] and this chapter models their idealized performance in an ambient pressure receiver design. TCO NPs scatter short wavelengths of light and absorb strongly in the infrared due to localized

surface plasmon resonances (LSPRs). Examples of TCOs are aluminum doped zinc oxide (AZO), indium tin oxide (ITO), and antimony doped tin oxide (ATO).

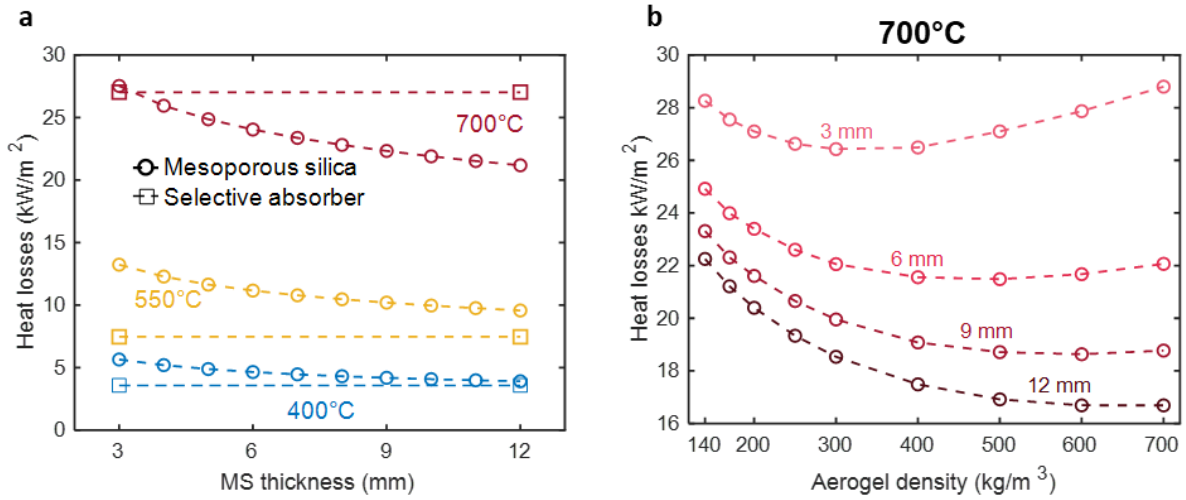


Figure 5.5. Heat loss reduction by increasing thickness and density. (a) Heat losses through an ambient pressure receiver using MS or state-of-the-art selective absorbers. Increasing the density increases the infrared opacity of the MS which significantly suppresses thermal losses at higher temperatures.

The optical properties of ideal TCOs are predicted by the Drude Model:

$$\epsilon = \epsilon_\infty - \frac{\omega_p^2}{\omega^2 - \omega\gamma i} \tag{16}$$

where $\epsilon$ is the permittivity, $\epsilon_\infty$ is the core dielectric constant, $\omega$ is the radial frequency of light, $\omega_p$ is the plasma frequency, and $\gamma$ is the damping coefficient. The only tunable parameter, the plasma frequency, is proportional to the square root of the concentration of free electrons (*i.e.* $\omega_p \propto \sqrt{n}$). The concentration of free electrons can be tuned by changing the dopant concentration (Al, Sn, and Sb for AZO, ITO, and ATO, respectively). Increasing the dopant concentration increases $\omega_p$, which in turn shifts the location of the LSPR to shorter wavelengths. Therefore, TCOs are particularly interesting for the application of CST where different temperatures and applications may require different optical properties of the TCO NPs. Figure 5.6a shows the estimated properties of the TCO NPs using Drude parameters of a typical TCO.[39,40] The theoretical TCO NP exhibits a strong absorption peak around 4.5 µm – conveniently within the infrared transparency region of MS. The TCO-loaded MS demonstrates significant reduction in heat losses as shown in Figure 5.6b. As a test case, Figure 5.6b shows an 8 mm thick, 300 kg/m$^3$ dense MS with varying

TCO NP volume loading. As expected, the heat losses decrease with increasing TCO NP loading. Unlike changing the density or thickness of the MS, however, the magnitude of the decrease is substantial. A small volume loading of 0.005% decreases heat losses by 14% at 700°C. This indicates that even slightly increasing the absorption within the transparency region of MS significantly suppresses radiative losses. The introduction of TCO NPs reduces the thermal emission from the cold side of the MS – specifically within the region in which the glass tube is transparent. Whereas native MS is mostly transparent at wavelengths <5 µm, the TCO-loaded MS absorbs the radiation from the absorber, re-emitting it at lower temperatures. Between 3 and 5 µm, where typically a significant portion of native loses thermal radiation, the 0.020% by volume TCO NP-loaded MS loses less than 10% of the losses normally associated with this band. This indicates that rather than transmitting radiation from the high temperature solar absorber, the TCO NPs enable the greenhouse effect in regions where MS is normally non-absorptive – thus reducing thermal radiative losses.

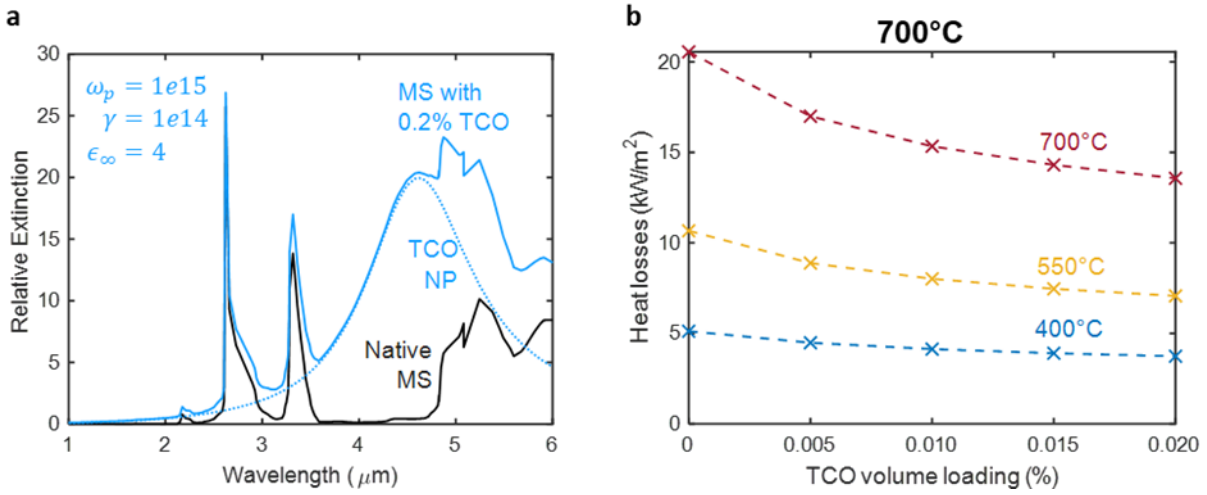


Figure 5.6. Heat loss reduction through use of TCO NPs. (a) The use of selectively transparent plasmonic nanoparticles selectively increases absorption within the transparency window of MS. (b) Heat losses through MS with respect to TCO NP volume loading.

### 5.5.3 Operation of MS-based receivers Under Vacuum

Typical linear annular receivers with SAs operate in high vacuum (<$10^{-4}$ bar) for two reasons: (i) to enable the use of higher performing SAs that are unstable in the presence of oxygen and (ii) to limit the thermal losses from internal convection. Operating at low vacuum (~$10^{-2}$ bar) could reduce the operating costs of

SA-based receivers, but it would not eliminate oxidation or the internal convective losses since the conductivity of gases is independent of pressure until it reaches the Knudsen regime at high vacuum. MS-based receivers, on the other hand, could benefit from low vacuum since the thermal conductivity of MS can be highly dependent on pressure – especially at low densities (Figure 5.7a). Conduction within MS occurs through the gas molecules in the pores and through the solid silica backbone. For densities <200 kg/m$^3$, the gaseous conductivity is the dominant mode of conduction, so operating at low vacuum decreases the conductivity of MS by >50%. At higher densities, though, the contribution from the solid silica network begins to dominate, so operating at low pressures offers little improvement in the conductivity of MS.

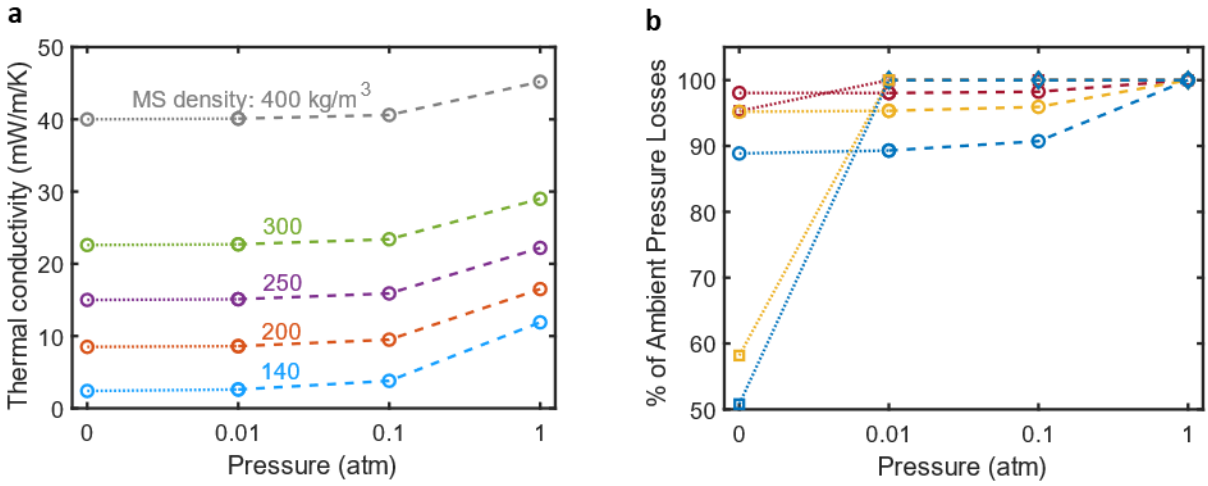


Figure 5.7. MS performance in vacuum. (a) The non-radiative thermal conductivity of MS depends greatly on the density and pressure. (b) Operating in low vacuum offers some performance gains for MS-based receivers, but SAs experience even greater improvement gains from operation in vacuum.

Since high temperatures require denser MS to suppress the larger radiative losses, operating at low vacuum offers little potential for heat loss reduction. As a proof of concept, Figure 5.7b shows the results of the optimized thickness of the SOTA MS at varying pressures and temperatures. At 700°C, the heat losses through an MS-based receiver only decrease by <2% in low vacuum. Even operating at full vacuum (zero pressure) offers no additional decrease in heat loss – indicating that internal convection plays a minor role in the overall heat losses in the high-temperature MS-based receiver. Figure 5.7b also shows a surprising conclusion for the SA-based receiver at 700C. Even without a conductive or convective resistance barrier, operating in full vacuum offers a 5% reduction in heat loss because at 700°C, internal

convection only accounts for 7% of heat losses for the SA-based receiver. This work shows that at high temperatures, radiation dominates the overall heat fluxes, so operating at lower pressures offers only negligible improvements in performance – no matter if MS or a SA is used.

At lower temperatures where conduction plays a larger role in heat losses, operating in low vacuum decreases heat losses by < 10%. Unlike at 700°C, conduction accounts for a significant portion of total heat losses at 400 and 550°C – 21% and 14%, respectively. Operating at low vacuum, which decreases the non-radiative conductivity by >30%, offers more room for improvement. Figure 5.7b also shows why 1$^{st}$ generation, vacuum tube PTC receivers operate in full vacuum. At their operating temperatures, which are < 400°C, operating in full vacuum nearly cuts the thermal losses in half. This is partially due to the higher performance of vacuum-stable SAs, but mainly because heat losses due to internal convection are eliminated.

### 5.5.4 Collector Efficiency for Heat Loss Reduction Methods

Figure 5.8 presents the collector performance of MS-based receivers for geometric concentration ratios from about 50 – 90. Depending on the absorber temperature, the most effective method for improving collector efficiency is either operating under vacuum or the use of TCO NPs. At 400°C, where conduction constitutes a larger fraction of thermal losses, there are significant performance gains from operating in vacuum. At higher temperatures, which are increasingly dominated by radiation, the use of TCO NPs offers the greatest potential for performance increases. TCO NPs offer minimal improvement benefits at 400°C because the selectivity of plasmonic nanoparticles, even the ideal ones modeled here, is too low. The decrease in solar transparency outweighs the decrease in thermal losses. This is true even for the lowest TCO NP loading analyzed in this work, which is only 0.005%. At 550°C, the optimal TCO NP loading is ~0.010% and at 700°C, it is greater than 0.015%.

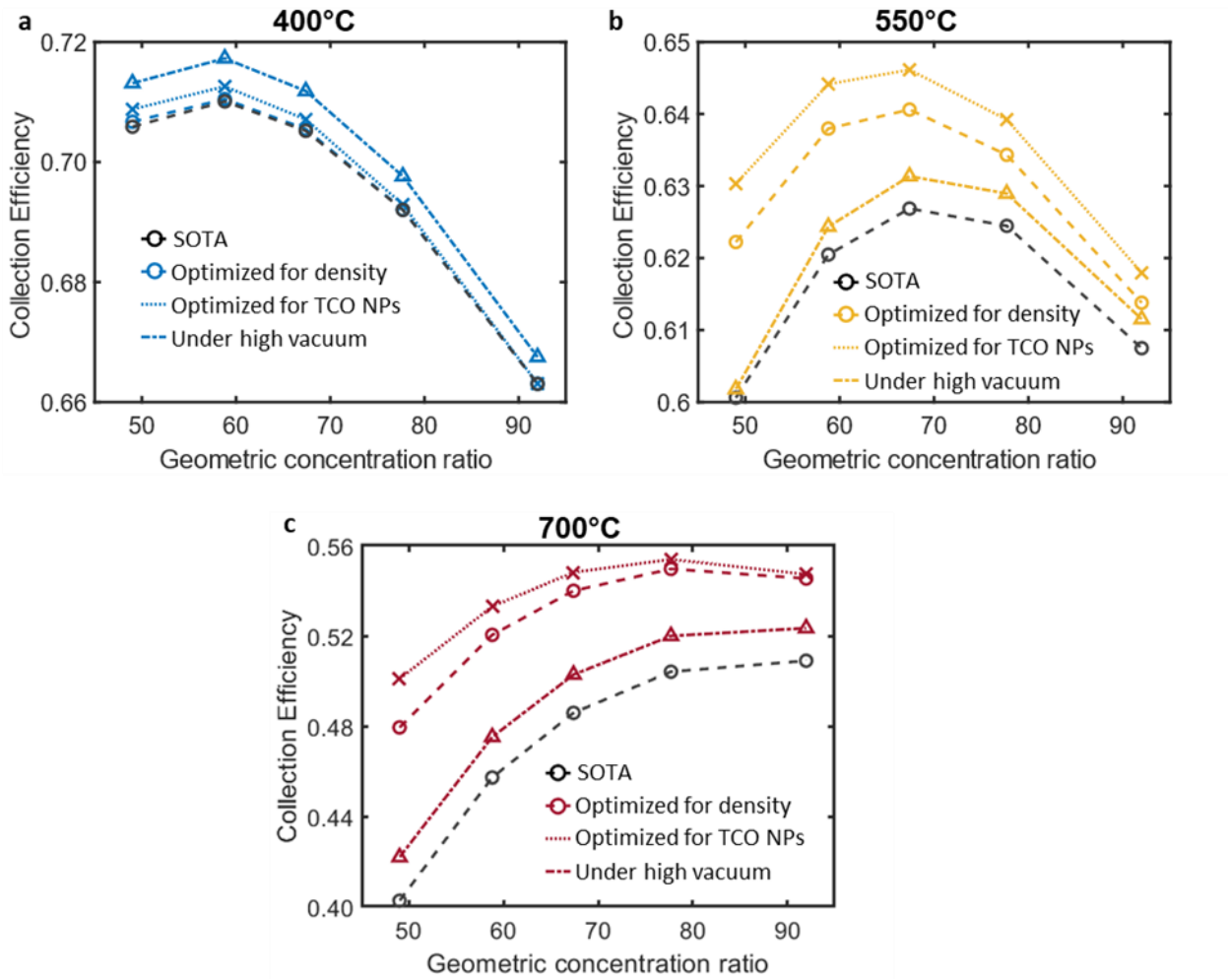


**Figure 5.8. Collection efficiency of heat loss reduction methods. (a) 400°C, (b) 550°C, and (c) 700°C.**

Optimizing density also presents an option to improve the collector efficiency by 3-6% absolute at 550 and 700°C. The increase in the infrared absorption of thicker MS decreases the radiative heat flux without any significant sacrifice to the solar transparency of MS. Supplementary Note #10 also contains more plots for the optimal densities and thicknesses of MS at each temperature. At 400°C though, there is minimal improvement for optimizing the density at 400°C because the SOTA density of 170 kg/m$^3$ is nearly the perfect density that should be used at 400°C (~200 kg/m$^3$).

## 5.6 Results: Tandem Receiver

### 5.6.1 Heat Losses for Tandem MS/SA Receiver

Finally, this last section analyzes the impact of combining native MS with SAs to minimize heat losses. The only difference in the heat transfer model is that an SA replaces a blackbody absorber for the MS receiver. From the perspective of MS-based receivers, using SAs will always reduce heat losses since MS is mostly transparent between 2 – 5 µm. The low infrared emissivity of SAs reduces the radiation transmitted straight through the MS. In essence, SAs aim to accomplish the same thing as TCO NPs – slight decreases in solar collection for large decreases in thermal losses – albeit in a different manner.

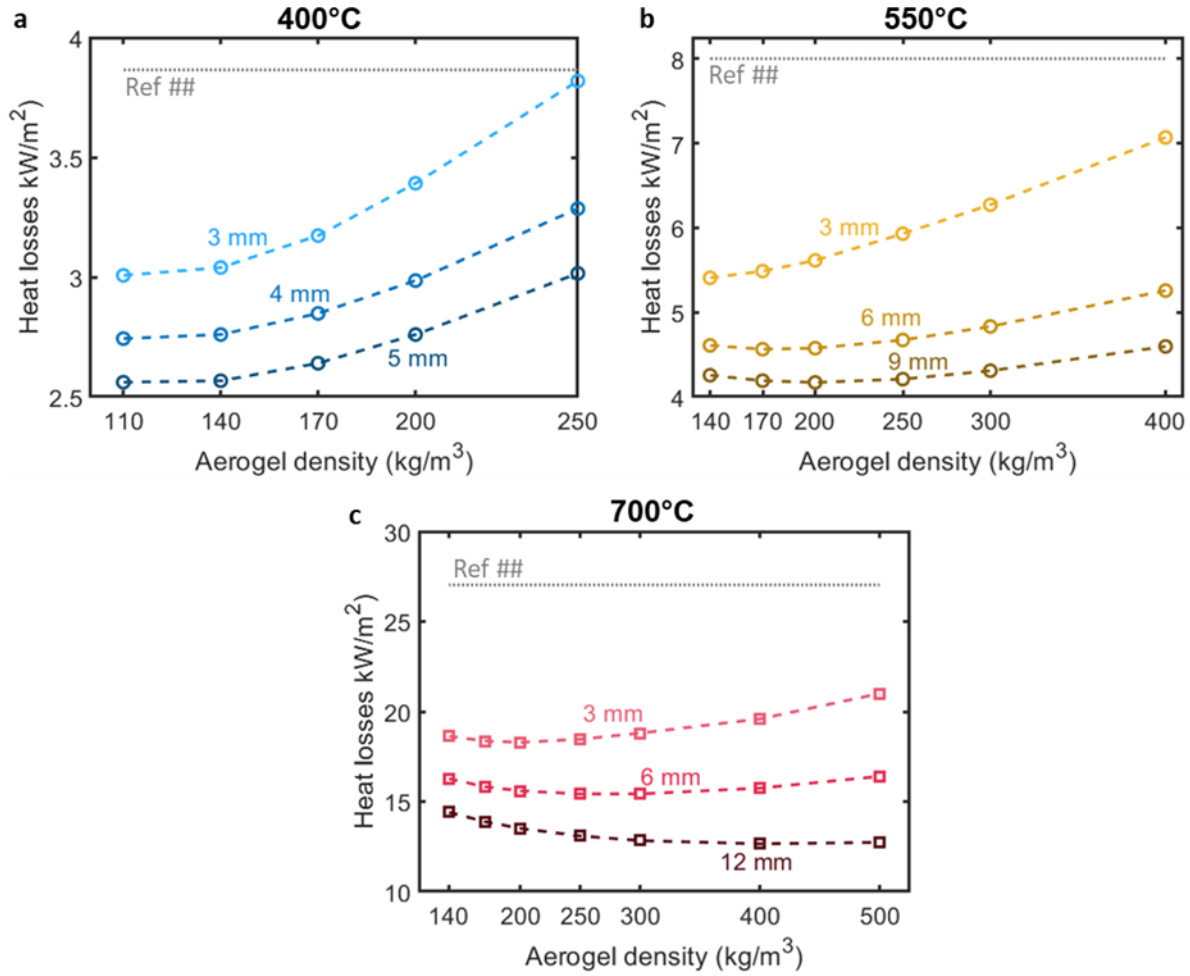


**Figure 5.9. Heat losses for tandem MS/SA receiver at (a) 400°C, (b) 550°C, and (d) 700°C.**

Interestingly though, from the perspective of SAs, the use of MS may *increase* the overall heat flux. At wavelengths greater than 5 µm, MS behaves as a blackbody because it attenuates all radiation and has a

refractive index close to 1.[41] MS only decreases heat losses at long wavelengths if the temperature drop across the MS is large enough to overcome the increase in emissivity. This is seen in Figure 5.9a. If the layer of MS is 3 mm thick and has a density greater than 300 kg/m$^3$, the heat losses are higher than the bare SA-based receiver. The temperature across the relatively thin and conductive layer of MS results in higher heat losses due to the MS's higher emissivity at wavelengths >5 μm. This is exactly how high emissivity coatings increase heat losses for industrial applications. At densities <250 kg/m$^3$, the temperature drop across the MS is large enough to reduce the overall heat losses. The radiative losses of the tandem receiver are so low in fact, that the optimal density of MS for 400°C is lower than 110 kg/m$^3$, compared to ~200 kg/m$^3$ for the standard MS-based receiver.

On the other hand, at 550°C, the tandem MS/SA receiver is more insulating than the bare SA-based receiver at all relevant thicknesses and densities because the temperature drop across the MS is sufficiently large. And compared to the MS-based receiver, the tandem receiver decreases heat losses by nearly 50% for a 6 mm thick layer of MS. At 700°C, the results are also promising, because unlike 400 and 550°C, the long wavelength emissivity of the SA is relatively high (> 0.5). This decreases the difference in long-wavelength radiative losses between the SA-based and tandem receivers. The temperature drop across the MS at 700°C is over 400°C for a 3 mm thick layer of MS – a sufficiently large enough decrease in temperature to offset the increase in emissivity. However, the emissivity of the SA at short wavelengths is still quite high (~0.7), so the decrease in heat losses in the infrared transparency region of MS is less pronounced. These two forces result in a ~40% reduction in heat losses for 6 mm thick MS using the tandem MS-SA receiver.

Another conclusion is that the optimal density for MS at each thickness shifts towards lower densities when used in conjunction with an SA. The use of an SA reduces the thermal radiative losses through the MS, making conduction a more prominent heat loss mode. The higher conductivity of denser MS then becomes a liability when radiation is not as significant. Specifically, at 400°C with a blackbody absorber, the optimal density of MS is around 200 kg/m$^3$, but with an SA-based receiver, the optimal density is < 110 kg/m$^3$. For 700°C, the optimal density decreases from ~500 kg/m$^3$ to ~250 kg/m$^3$.

### 5.6.2 Collector Efficiency for Tandem MS/SA Receiver

This section presents the collection efficiency of the tandem MS/SA receiver (Figure 5.10). Similar to the plasmonic nanoparticles, the tradeoff between decreased solar absorption and reduced heat losses may result in a lower efficiency than the original MS-based receiver with a blackbody absorber. This is evident at 400°C where in fact the presence of the SA decreases the efficiency compared to a blackbody absorber. At 550°C, though, the significant decrease in heat losses by using the tandem receiver designs outweighs the small penalty (4%) in solar absorptance. Specifically, the tandem MS/SA receiver achieves a higher efficiency than the individual SA-based receiver by >1% absolute. For 700°C, the penalty in solar absorption (8%) is too large for the decrease in heat losses to improve performance. The lack of selectivity within the infrared transparency region is too large (>70%) to justify the loss in solar absorptance. It is simply more difficult to nanoengineer selective structures that are stable at >700°C. Although the heat losses are over 25% less for 12 mm thick MS, the low solar absorptance of the SA at 700°C leads to an overall decrease in performance compared to a blackbody broadband absorber. Therefore, the only improvement in performance for the tandem receiver is for moderate temperatures around 550°C.

To maximize the improvement in the tandem MS-SA design, it is clear the solar absorptance must be maximized. The performance metrics that dictate the performance of SA-based receivers are slightly different for tandem receivers. Whereas in traditional SA-based receivers, there may be a benefit to losing absorptance for decreasing thermal emittance. For tandem receivers, the thermal emittance is much less important as the insulating layer of MS renders the emittance of the SA irrelevant for wavelengths >5 μm. The only region of importance is the surface emittance at wavelengths < 5 μm, since that is where MS is transparent. For example, a theoretical selective absorber with a solar absorptance of 0.98 and a constant thermal emittance of 0.8 performs better in the tandem design, even though the selectivity of the SA is worse. Any potential SAs for use with MS should prioritize solar absorptance which explains the prominence of blackbody, broadband absorbers for use with MS.

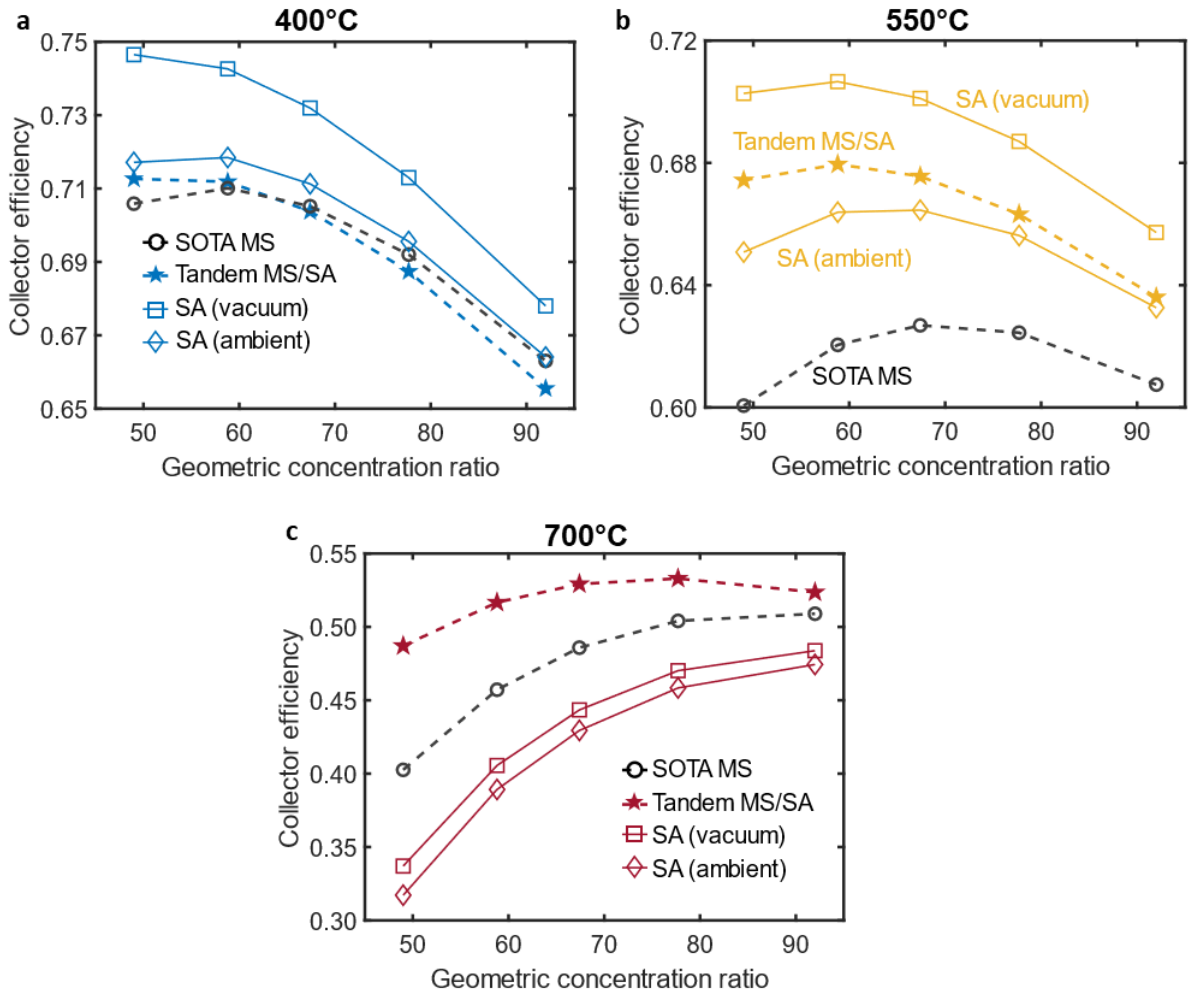


**Figure 5.10. Collection efficiency of tandem MS/SA receiver with optimized thickness and density. (a) 400°C, (b) 550°C, and (c) 700°C.**

One of the key findings of this work is that for solar receivers to operate more efficiently at elevated temperatures, it is critical to reduce thermal losses. For MS, multicomponent mesoporous insulation such as our previous work on developing refractory aerogels offers one possible pathway.[3] MS coated with a single cycle of alumina maintains hydrophilicity of the multicomponent insulation even at temperatures as high as 500°C. The presence of water at high temperatures helps close the infrared transparency gap of MS, leading to reduced radiative losses. Additional methods may focus on doping MS (e.g., phosphorus or boron) to selectively introduce vibrational modes between 2 – 5 µm, ultrathin selective plasmonic coatings, and infrared filters. As for SA-based receivers, stable paint-like coatings may lead to the highest

performance since they do not require nanostructuring. Optimizing the properties of the base coating and the absorbing nanoparticles may lead to additional improvements.

## 5.7 Conclusion

This chapter benchmarks the performance of MS-based in parabolic trough collectors at temperatures of 400, 550, and 700°C. The results show that MS-based receivers are lower performing than current state-of-the-art SA-based receivers for 550°C and below. At 700°C, however, MS performs significantly better. The chapter provides results on multiple methods to enhance the performance of MS-based receivers such as tuning the physical properties (density and thickness), incorporating selective plasmonic nanoparticles, and using MS in tandem with SAs. These results show that high receiver efficiencies are obtained by hybrid MS-SA receivers at temperatures below 550°C, and selective plasmonic nanoparticles reach the highest efficiencies for temperatures above 700°C.

# Chapter 6 : Technoeconomic Analysis of a Prototype Refractory Aerogel Linear Receiver

*Contributions to this chapter: Dr. Ali Davoodabadi developed the experimental test stand. Andrew Gayle (Dasgupta Lab) completed the ALD process. Most of the development and characterization of the prototype receiver can be found in the DOE final report, which can be found on OSTI.gov.*

## 6.1 Motivation

The goal of an aerogel-based linear receiver is to reduce the cost of generating high temperature heat. Although previous chapters have demonstrated experimental improvements on the lab-scale (~1" aerogel discs), this chapter reviews the performance of an upscaled, prototype aerogel receiver. Larger-scale demonstrations provide more confidence in the performance of the technology by accounting for various other loss mechanisms that are not as prevalent in smaller-scale experiments.

This chapter presents experimental heat loss results of a prototype linear receiver based on the design in **Chapter 5**. An opaque porous ceramic insulates the top half of the absorber tube, while aerogels insulate the bottom half that is coated with a high emissivity coating. This receiver is tested off-sun, or in "dark" conditions. The receiver is heated not by concentrated sunlight but by a resistive heater that is placed within the steel absorber tube. The heat losses are measured by calculating the power input into the resistive heater at steady state. The results from this study show that aerogels reduce heat losses compared to the receiver with no aerogels, demonstrating their insulative properties. A comprehensive technoeconomic analysis shows the potential for aerogel-based linear receivers to deliver high temperature heat cheaper than existing zero-carbon methods.

## 6.2 Designing the Receiver

The ideal design for the aerogel receiver is depicted in Figure 6.1d, where a curved aerogel hugs the solar absorber tube. This design minimizes heat losses since the area of the aerogel insulation is minimized. It also maximizes the optical efficiency since all the incident sunlight is perpendicular to the aerogel surface. In practice, however, this design is extremely difficult to fabricate since it requires curved aerogels – a nontrivial task. The same Soltrace model used in **Chapter 5** is used here to estimate the optical efficiency of a few other nonideal designs.

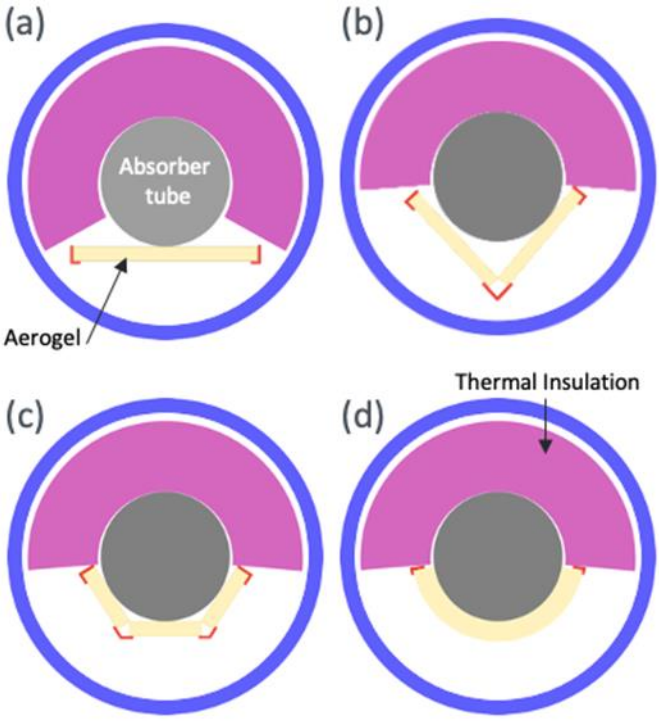


Figure 6.1. Four proposed geometries for aerogel integration into the receiver labeled as (a) flat, (b) V-shape, (c) half-hex and (d) curved (ideal).

Figure 6.1a shows the first configuration which consists of a single stack of flat aerogel tiles placed along the tube length. While this geometry is favorable because of the simplicity it offers for receiver design, achieving an 80° acceptance angle with a single flat aerogel is impractical due to the very large glass envelope it would require. Hence, this geometry was discarded.

A V-shape aerogel configuration was another candidate in which two racks of aerogel tiles are positioned alongside each other to form a V-shape geometry below the absorber tube, as shown in Figure 6.1b. While still using flat aerogels, this geometry allows for large acceptance angles. It is also important that this geometry does not make the receiver design too complicated.

Half-hex is another proposed configuration where three racks of neighboring flat aerogel tiles are positioned to form a half-hexagonal geometry below the absorber tube (Figure 6.1c). This design resembles the curved aerogel geometry more than the V-shape design and makes achieving large acceptance angles easier. However, it also adds complexity to the receiver design as the number of part increase. The required tracks to support the aerogel tiles also increase relative to the V-shape design which can result in additional shading.

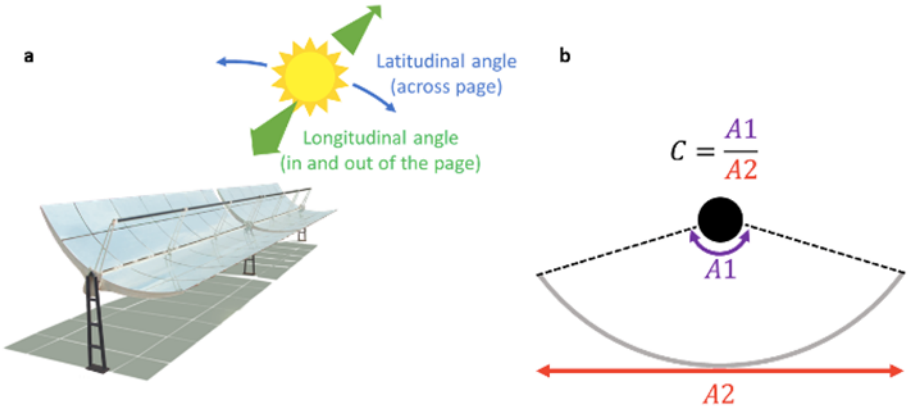


Figure 6.2. Independent variables of interest. (a) Linear receivers track across the latitudinal angle but are unable to track longitudinal angles. (b) The concentration ratio, $C$, is the ratio of the exposed area of the absorber to the projected area of the parabolic mirrors.

Figure 6.1d shows the ideal curved geometry. However, current aerogel synthesis capabilities are limited to flat aerogels, and hence, this geometry was not selected for this project. Instead, this chapter focuses its analysis on the V-shaped and half-hex designs to elucidate which is most practical and feasible given our processing limitations. The following sections analyze how the optical efficiency is affected by (i) the longitudinal angle, (ii) latitudinal angle, and (iii) concentration ratio (Figure 6.2).

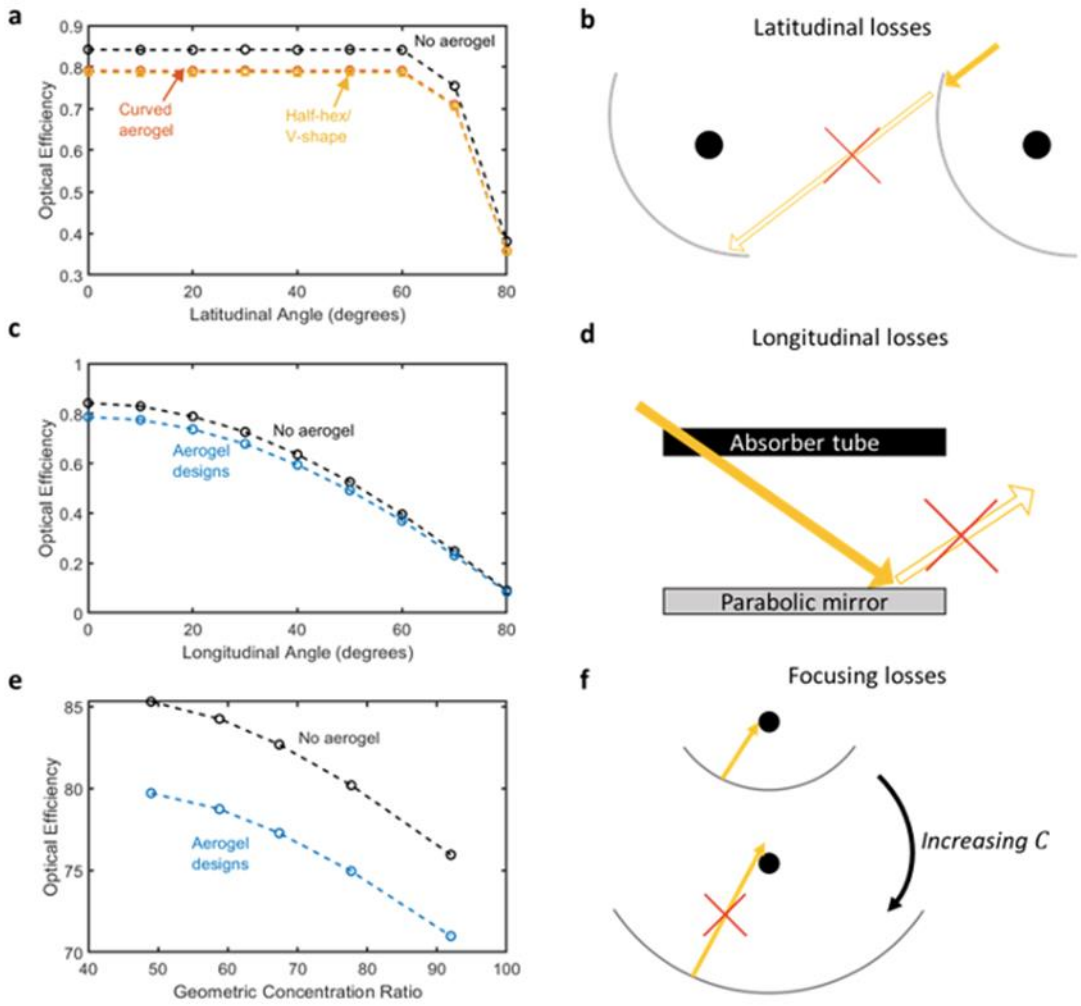


Figure 6.3. Results of the optical modeling: all aerogel designs have practically the same optical efficiency. (a),(b) Latitudinal losses only start at high incidence angles when neighboring troughs obstruct incident sunlight. (c),(d) Longitudinal losses are not only cosine losses, but also account for incident rays that miss the absorber tube. (e),(f) A ray that might be incident at a lower concentration misses at a higher one.

For linear concentrating systems, the latitudinal angle has a small impact on the optical efficiency (Figure 6.3a) because linear concentrators track the sun across the sky (*i.e.*, latitudinally). At extreme latitudinal angles, however, neighboring concentrators block sunlight from reaching the mirrors of interest (Figure 6.3b). On the other hand, the longitudinal angle has a significant impact on the optical efficiency (Figure 6.3c). At locations far from the global equator or in certain seasons of the year, the sun follows an arc that is lower in the sky. Any incident sunlight which is off-normal introduces cosine losses. Additionally, the ends of a receiver receive no concentrated sunlight due to the off-normal incidence (Figure 6.3). Lastly, the optical efficiency decreases with increasing solar concentration ratio (Figure 6.3e). Most solar

receivers are designed for an 80° acceptance angle, so the only way to increase the concentration ratio is to increase the projected area of the concentrating mirrors. Thus, the only way to increase the concentration ratio is to increase the focal length of the parabolic mirror, but a higher focal length makes it more difficult for concentrated sunlight to reach the receiver due to focusing and surface errors (Figure 6.3f).

The optical efficiency modeling also shows that the curved aerogel indeed has the highest optical efficiency of any aerogel design followed by the half-hex design. Fortunately, the aerogels are highly transparent to normal incident light (95% solar-weighted transmission), such that the cosine losses from the V-shaped and half-hex designs are minimal. Given all three designs have nearly the same optical efficiency, the V-shaped design was chosen for its combination of simplicity and performance. The next section in this chapter reviews the performance of a prototype aerogel receiver with a V-shaped aerogel design.

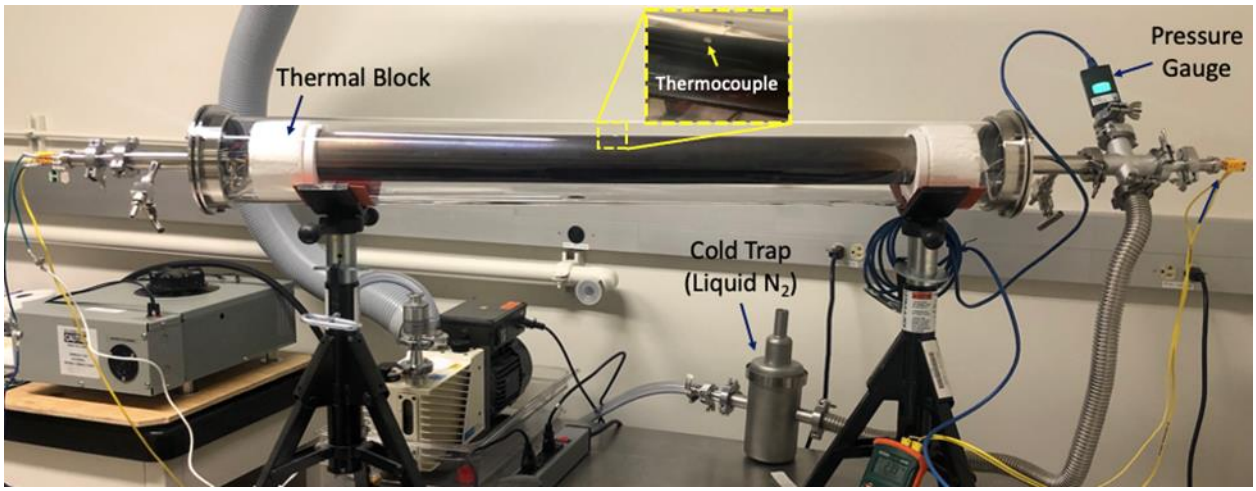


Figure 6.4. The developed PTR test stand with a 3-feet-long absorber tube for heat loss measurement experiments. Instrumentation for monitoring the temperature and pressure inside the receiver are shown.

## 6.3 Prototype Receiver Design

Figure 6.4 shows a 91 cm (36”) long, 37mm OD steel absorber tube that is placed inside of a 120 cm long, 5” OD quartz tube. One flange of the quartz tube contains the components to pull and measure vacuum. Specifically, a pressure gauge and a dual-stage rotary vane pump (Agilent, DS202) equipped with a liquid nitrogen cold trap are both connected to a T connected to the left flange. The opposite flange supports the power input into the silicon carbide resistive heater and the thermocouples used to measure the temperature at three locations throughout the absorber tube (the top and bottom of the center and the bottom of the edge). The resistive heater ($\Omega$ ~ 9.8 ohm) is powered by a variable AC voltage transformer (Variac by Staco). High temperature porous ceramic insulates both ends of the receiver to mitigate end losses, and semi-cylindrical pieces insulate the top half of the absorber tube. The bottom of the absorber tube was coated with a commercially available high emissivity paint for automotive applications (VHT Flameproof).

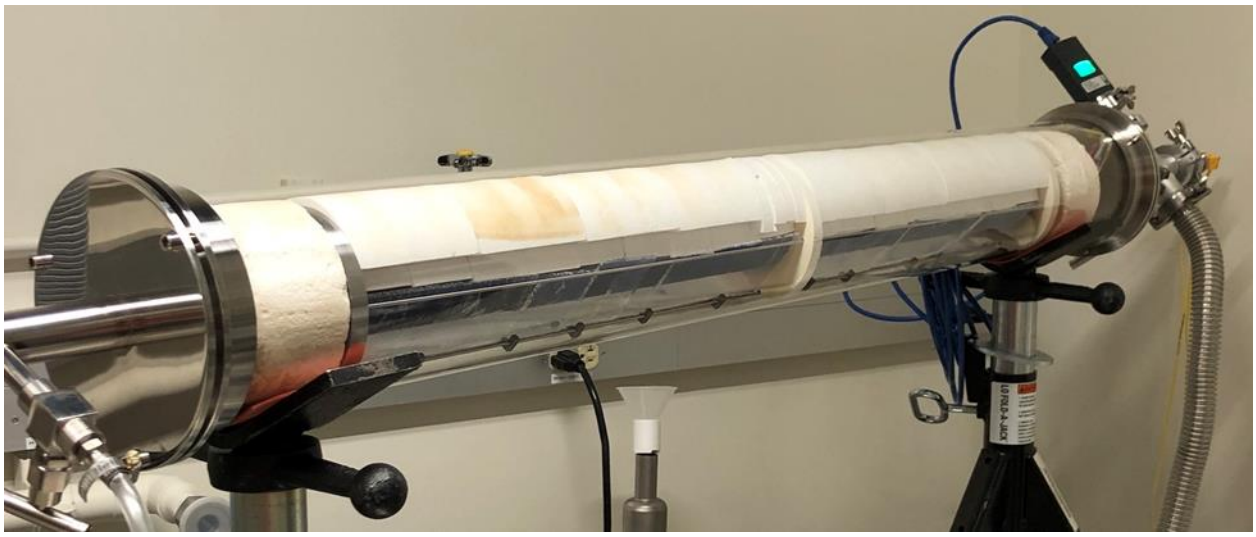

Figure 6.5. Picture of the aerogel-integrated receiver developed in this work undergoing heat loss measurement experiments.

In the final design, a series of stainless-steel tracks support the aerogels from the bottom and the sides (Figure 6.5). Three ceramic or steel track feedthroughs – two at each end and one in the middle – support the stainless steel tracks. The bottom tracks contain stainless steel ‘clips’ that support the aerogels (Figure 6.6). There are roughly 2 clips per aerogel tile to ensure that each aerogel has multiple points of support.

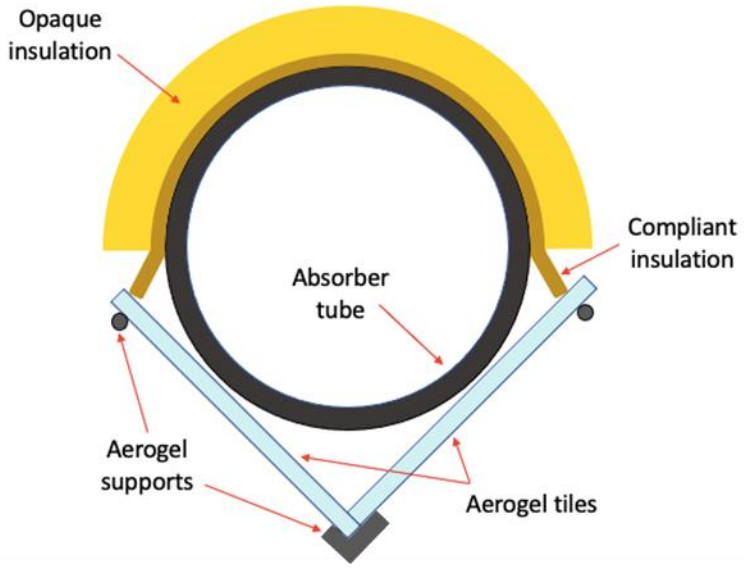


Figure 6.6. Schematic of a fully insulated absorber with opaque alumina-silica alumina insulation on top with transparent aerogels below.

## 6.4 Heat Loss Testing and Modeling

The heat losses from the receiver are measured at steady state, where the power supplied to the heater (voltage times current) equals the power dissipated in the receiver test stand and lost to the ambient. Thus, receiver heat loss ($Q_{loss}$) is obtained by calculating the net amount of power supplied to the resistive heater ($P$). Heat loss per meter of the absorber tube (W/m) is calculated by dividing $Q_{loss}$ to the length of

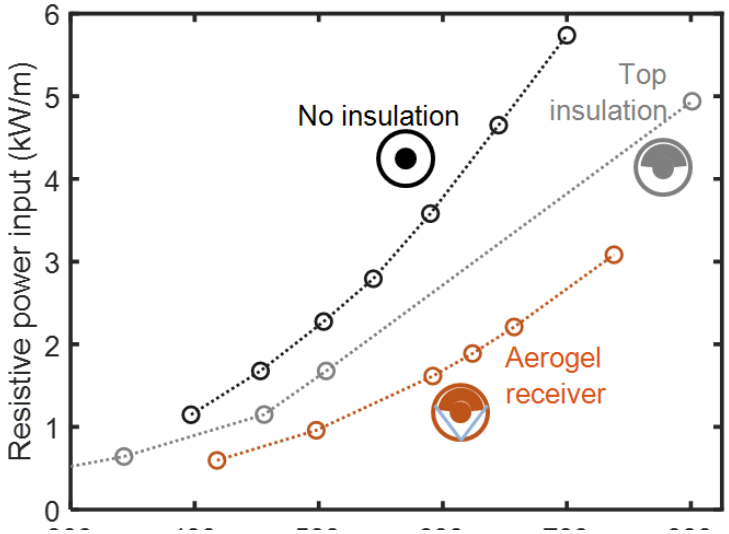


Figure 6.7. Power input with the resistive heater versus the midpoint temperature. The aerogel receiver decreases the power input by ~30% compared to the top insulation case.

the absorber tube in our test stand (3 feet). The following tests were performed in vacuum to directly compare the performance of this design to state-of-the-art evacuated receiver tubes.

Baseline experiments are run with an uninsulated absorber tube, with the setup shown in Figure 6.5. Another series of experiments are performed with only the upper half of the absorber tube being insulated (using the opaque insulation), and the final set of experiments are executed with a fully insulated absorber tube where aerogels are integrated into the receiver (setup in Figure 6.5). It is worth noting that prior to carrying out the heat loss experiments, the chamber is purged with dry air to remove any moisture and lower the operating pressure of the receiver. For the aerogel receiver tests, the receiver was held under vacuum for at least 24 hours to ensure the removal of all gas from the aerogels.

Figure 6.7 shows the results from the heat loss measurements from temperatures of 350 – 750°C. The aerogels demonstrate their impressive insulating properties by decreasing the power input into the receiver by ~30% compared to the case with just top insulation. Compared to no insulation, the heat losses decreased by more than 50% for the aerogel-integrated receiver (2,750 W/m to 5,600 W/m) at 700°C. Figure 6.7 shows the heat loss values obtained from carrying out experiments at a range of absorber tube temperatures between 350°C to 750°C.

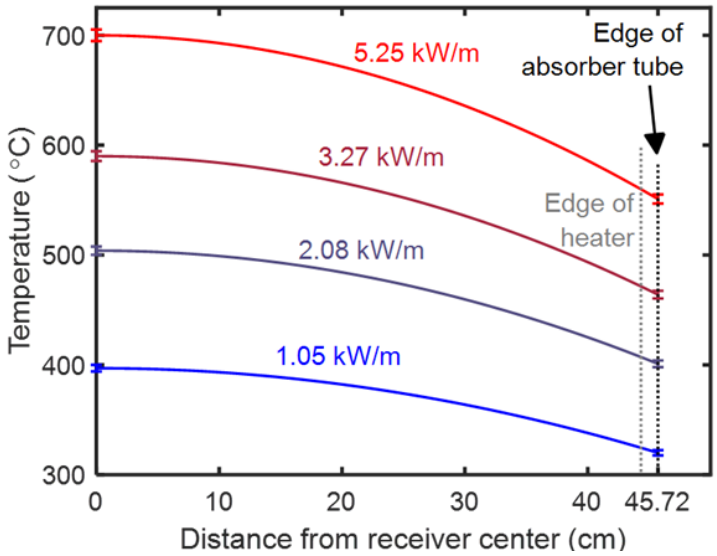


Figure 6.8. Assumed parabolic temperature profiles of the receiver experiments based on temperature measurements at the center and edge of the absorber tube. Figure only provides the temperature profile of four of the uninsulated case.

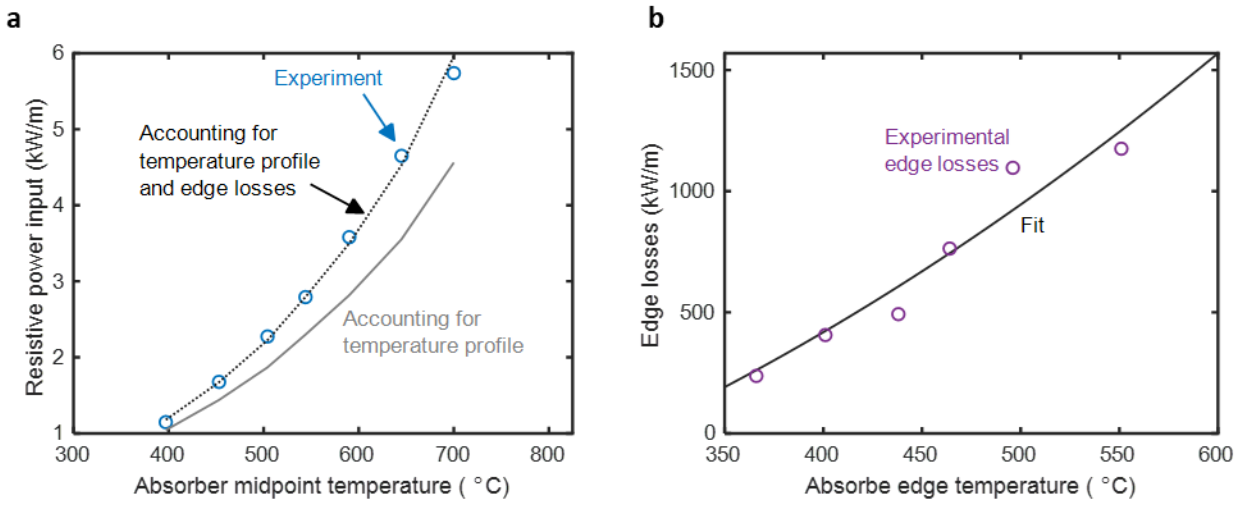


Figure 6.9. Factoring in edge losses into the heat transfer model. (a) The quadratic temperature profile is an input into the heat transfer model for the uninsulated case. As expected, the model underestimates the heat losses. (b) The difference in the predicted and experimental heat losses with respect to edge temperature. A best fit for the data provides the estimation of heat losses at a given edge temperature.

The results in Figure 6.8 are specifically defined as "resistive power input" rather than "heat losses" because there is a large temperature drop across the absorber tube, and consequently, edge losses. To account for the edge losses, the heat transfer models from Chapter 5 are used to estimate the heat losses in the experimental receiver. One of the key inputs into the model is the absorber temperature which is known not to be constant. Two thermal couples, one in the center of the absorber tube, and one at the edge, provide the two extremes. The temperature profile is then assumed to be quadratic Figure 6.8). Other inputs into the model include the thermal conductivity of the opaque insulation and emissivity of the absorber coating.

Once the temperature profile is known, the model then predicts the heat losses for the experimental setups (Figure 6.9a). As expected, the model underestimates the heat losses since the model assumes infinite 1-dimensional heat transfer. The difference in the expected and actual heat losses then provides a basis for the edge losses in the receiver (Figure 6.9b). The edge losses are mostly a function of the edge temperature of the receiver, meaning that the edge losses should be independent of the different designs. This enables the accurate prediction of edge losses for the aerogel receiver.

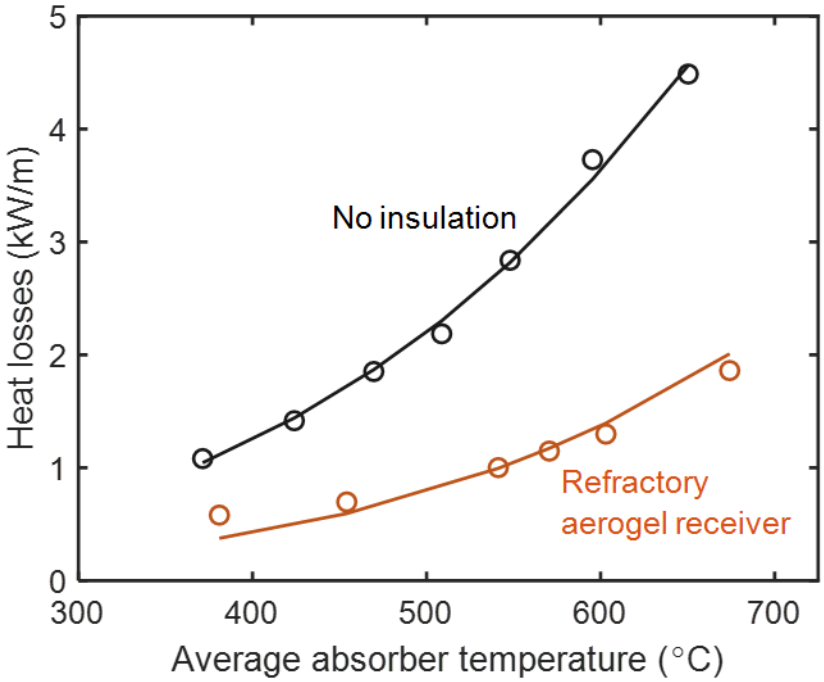


Figure 6.10. Modeled heat losses *vs.* the adjusted experimental heat losses that remove the predicted edge losses. With edge losses removed, the refractory aerogel receiver loses less than 2 kW/m at an average absorber temperature of 674°C.

Knowing the edge losses at a given absorber edge temperature, the experimental aerogel receiver heat losses are adjusted to estimate the heat losses per meter in a more realistic CST plant (Figure 6.10). The heat losses of the refractory aerogel receiver decrease to under 2 kW/m for an average temperature of 674°C, and there is a decent agreement between the model and the experimental results. Disagreement between the modeling and experimental results is likely a result of gaps in the aerogel tiles, the use of room-temperature emissivity measurements for the solar absorber at high temperatures or using an unknown temperature profile (assumed quadratic) for the absorber tube. Regardless, the model agrees well enough with the experimental data to use the model to predict how the aerogel receiver will behave in a commercial-scale CST plant.

## 6.5 Technoeconomic Analysis

To understand how this aerogel receiver impacts the performance of a CST plant, I developed an in-house technoeconomic model to estimate the performance of CST plants producing electricity or high

temperature process heat. This technoeconomic analysis (TEA) uses the fixed charge rate (FCR) method to estimate the levelized cost of electricity (LCOE):

$$LCOE = \frac{TCC * FCR + FOC}{AEP} + VOC \quad (6.1)$$

where $TCC$ is the total capital cost, $FCR$ is the fixed charge rate, $FOC$ is the fixed operating costs, $AEP$ is the annualized energy production, and $VOC$ is the variable operating costs. The unit of $LCOE$ is ¢/kWh$_e$, so the only difference for the calculation of the levelized cost of heat ($LCOH$) is that the $AEP$ is in units of kWh$_{th}$, indicating the energy is thermal energy, not electrical.

Table 6.1. Financing parameters in TEA

| Input | Value |
|---|---|
| Length of operation | 25 years |
| Project term debt fraction | 60% |
| Nominal return on investment | 13% |
| Nominal debt interest rate | 4% |
| Inflation | 3% |
| Effective tax rate | 38.75% |
| Construction interest rate | 6% |
| Depreciation | 5 year MACRS |
| Capital recovery factor | 0.061 |
| Project financing factor | 1.102 |
| Construction financing factor | 1.030 |
| Fixed charge rate | 0.069 |
| Indirect costs ($y$) | 13% |
| Contingency costs ($x$) | 10% |

The $FCR$ is based on financing parameters and has a value of 0.069 for this model based on the values in Table 6.1. Otherwise, the $FOC$ and the $VOC$ are established values by the U.S. Department of Energy

based on actual plant costs,[105] so the only values that need predicted are the $TCC$ and the $AEP$. The $TCC$ is calculated based on a cost framework developed by Henry and Prasher[106]:

$$SCC = SM\frac{C_{field}}{G_s \times \eta_{S-E}} + SM\frac{C_{receiver}}{\eta_E} + t_{storage}\frac{C_{storage}}{\eta_E} + C_{cycle} \quad (6.2)$$

where $SCC$ is the subtotal capital cost, $SM$ is the solar multiple, $C_i$ is the cost of the solar field (*i.e.*, collectors), receivers and heat exchanger system, thermal storage, and power cycle, $G_s$ is the solar incidence design point (normally 1,000 W/m$^2$), $t_{storage}$ is the hours of thermal storage, $\eta_{S-E}$ is the solar to electrical efficiency, and $\eta_E$ is the efficiency of the power cycle. The $SCC$ is converted to $TCC$ by accounting for indirect and contingency costs:

$$TCC = y(SCC + xSCC) + xSCC + SCC \quad (6.3)$$

where the first term accounts for indirect costs and the second accounts for contingency costs. The inputs to Equations 6.2 and 6.3 are provided in Table 6.2, and are mostly compiled from 2012 the Sunshot vision study[105] and a recent NREL CSP cost survey report.[107] The only property that changes is the cost of the solar receiver, which now must account for the cost of the aerogel. Aerogel industry partners have estimated a cost of $17/L, and the ALD coating process is assumed to be dominated by material costs – primarily triethylaluminum (TEA, ~$8/kg). As a conservative estimate, the handling and operating costs of coating the aerogel tiles are assumed to be twice that of the material costs. Using these cost estimates, the cost of the receiver only increases 5% when adding in the aerogel. Therefore, the cost projections for the CST plants use a value of $C_{receiver}$ that is 5% higher.

Table 6.2. CST technical inputs into TEA

| Input | Value |
|---|---|
| Site preparation | $20/m$^2$ |
| Solar field (*e.g.*, collectors) | $140/m$^2$ |

| | |
|---|---|
| Heat transfer system (*e.g.*, receivers, HEX) | $9.5/m$^2$ |
| Thermal energy storage | $15/kW$_{th}$ |
| Power cycle | $880/kW$_e$ |
| Time for storage | 12 hours |
| Power cycle efficiency | 0.47 (550°C)<br>0.51 (700°C) |
| Solar multiple | 2.8 |
| DNI design point | 1,000 W/m$^2$ |
| Annualized optical efficiency | 72.1% |

Most of the work in this thesis has focused on the performance of aerogels at a maximum design point (*e.g.*, 700°C and 100 suns). In reality, CST plants operate across a large variety of conditions as the sun rises and falls in the sky. The concentration ratio incident upon the receiver decreases when the sun is farther from solar noon because sunlight travels through more of the atmosphere. Furthermore, the temperature of the receiver decreases at night when there is no incident sunlight. As a result, the performance of a CST plant is highly dependent on how the receiver performs across the entire year, or in simpler terms, over the course of an average day.

The two remaining terms that are computed are $AEP$ and $\eta_{S-E}$ which are both a function of plant performance. The overall plant efficiency is a function of the efficiency of each of the components in Equation 6.2:

$$\eta_{plant} = \eta_{optical} * \eta_{receiver} * \eta_{storage} * \eta_{E} \quad (6.2)$$

The Solar Dynamics parabolic trough was chosen as the collector due to its large concentration ratio of 72 and high $\eta_{optical}$ of 72.1%. The thermal storage efficiency is assumed to be 95%.[108] Finally, this leaves the receiver efficiency (reproduced below) as a key output of the technoeconomic model. For the aerogel-based solar receiver, $\tau_{glass}$ is set to 97% and $\tau_{aerogel}$ is set to the experimentally determined solar-weighted transparency of 95% for the refractory aerogel. Lastly, the experimentally validated model estimates heat losses with respect to receiver temperature for a curved aerogel receiver (rather than the V-shape).

$$\eta = \alpha\tau_{glass}\tau_{aerogel} - \frac{Q_{loss}}{CG_s} \qquad (1.3)$$

To estimate the annualized receiver efficiency, the model estimates the receiver efficiency over the course of a "typical" day in the Phoenix, AZ region (Figure 6.11) where the average direct normal irradiance (DNI) is 7.5 kWh/m$^2$. One issue with parabolic trough collectors is that the heat transfer fluids may freeze at night, so the model assumes that electric resistive heaters maintain the temperature of the receivers at a minimum temperature of 200°C, which is above the melting point of chloride salts (~150°C). The temperature of the receiver only increases when the solar DNI exceeds the thermal losses of the receiver.

Furthermore, the thermal losses are averaged along the length of the solar collector loop. The temperature difference between the inlet and outlet of the loop is provided by NREL's System Advisor Model (SAM), which supplies temperature gradients for various power cycle temperatures. The receiver efficiency is then the sum of the of absorbed solar energy minus the heat lost over the course of the day, and the $AEP$ is a product of the yearly heat collected and the plant efficiency.

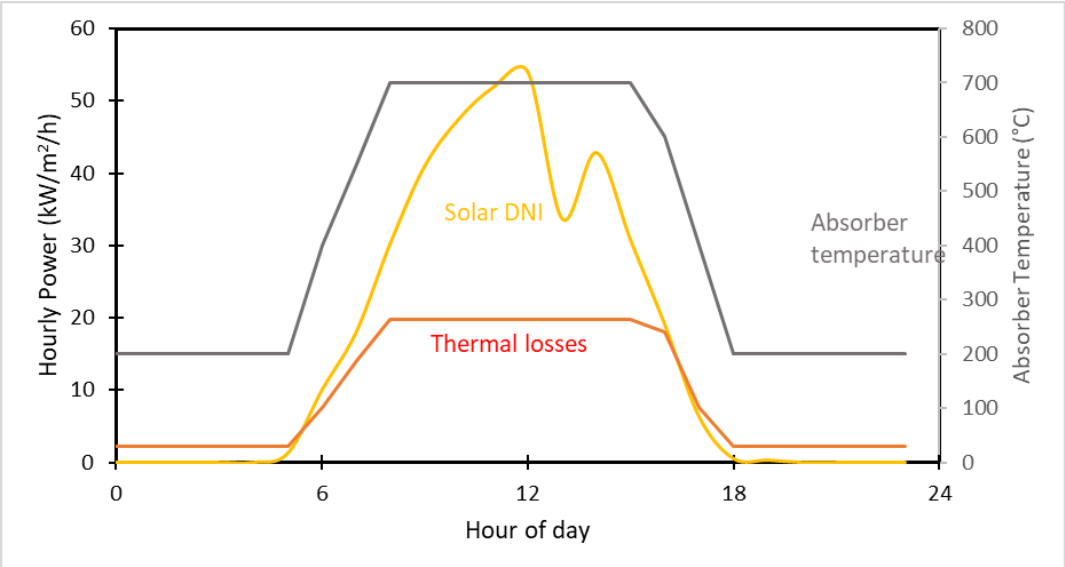


Figure 6.11. Temporal temperature and solar incidence for the receivers. The temperature of the receiver only increases when the absorbed solar DNI exceeds the thermal losses.

### 6.5.1 Model Validation and Results

To first confirm that the LCOE model is accurate, we used a variety of cost inputs and design parameters and compared the values to the 2012 Sunshot Visions report (Table 6.3). The in-house model is accurate since it estimates the LCOE of the plant designs within 1.5%, thus validating the model.

Table 6.3. Validation of In-house LCOE model

| | 2010 Trough | 2020 Trough Roadmap | 2020 Sunshot Targets (550°C tower) |
|---|---|---|---|
| **SETO values** | 20.40 | 11.60 | 6.00 |
| **In-house model** | 20.01 | 11.43 | 6.05 |

The cost results for updated the CST plants integrated with aerogel-based receivers are provided in Table 6.4, and it shows the aerogel receiver at both 550°C and at 700°C for moderate and high temperature $sCO_2$ cycles. As a baseline, Table 6.4 provides a cost for selective absorber-based receivers at 400°C. These include updated cost projections from a recent NREL CSP cost survey report. Recent cost reductions in the cost of the solar field (from \$190/$m^2$ to \$140/$m^2$) are the primary reason for the lower cost. The first takeaway from this analysis is that the refractory aerogel receiver, at both 550°C and 700°C, even with the curved aerogel shape, is costlier than the selective absorber design at 400°C. This is primarily due to the relatively high effective emissivity of the current refractory aerogels (~0.35), which are not plasmonic (*i.e.*, do not leverage PEGS). The refractory aerogel receiver performs well at peak irradiance (550°C and ~50 suns), but the heat losses at night lead to its higher LCOE. Similarly, the heat losses at 700°C are currently too high to justify using linear receivers.

However, there is some potential with tandem receivers, such as combining a non-plasmonic refractory aerogel with a state-of-the-art selective surface rather than a broadband absorber (see **subchapter 5.6** Results: Tandem Receiver). For 550 and 700°C, the same selective surfaces used in Chapter 5 are used here. Specifically, the CIEMAT absorber at 550°C and the nanoparticle pigment developed by Jifeng Liu's group at 700°C. Combining selective absorbers and aerogels leads to the lowest heat losses at night, so despite the loss in solar absorptance, the tandem receiver offers the greatest potential for higher temperature linear receivers. Specifically, the cost reduction from the 400°C baseline case to the 550°C tandem receiver is 6.3%. Integration of plasmonic aerogels or selective surfaces specifically designed for use in tandems is expected to further lower LCOE. This is a promising avenue for further investigation, beyond the scope of this LCOE study which is based on materials demonstrated at the receiver prototype scale.

Table 6.4. LCOE and LCOH of various prospective plant design

| | Selective absorber (400°C) | Refractory aerogel (550°C) | Tandem receiver (550°C) | Refractory aerogel (700°C) | Tandem receiver (700°C) | Solar PV with storage |
|---|---|---|---|---|---|---|

| | | | | | | |
|---|---|---|---|---|---|---|
| **LCOE (¢/kWh)** | 8.63 | 9.33 | 8.09 | 13.5 | 10.91 | 8.50 (battery) |
| **LCOH (¢/kWh$_{th}$)** | 1.91 | 2.10 | 1.79 | 2.96 | 2.44 | 4.33 (TES) |
| **Annualized efficiency (%)** | 21.2 | 19.9 | 21.7 | 15.8 | 18.0 | - |

Regardless of the higher costs of electricity production, the refractory aerogel receiver has the potential to offer very low-cost high-temperature heat for industrial processes. The primary way to decarbonize an industrial heating process is to use solar PV with thermal energy storage (TES), but that approach is relatively expensive at 4.33 ¢/kWh$_{th}$. In contrast, the cost of high temperature heat from tandem receivers is only 1.79 and 2.44 ¢/kWh$_{th}$ at 550 and 700°C, respectively.

## 6.6 Conclusions

The prototype linear receiver demonstrates that refractory aerogels can insulate a linear receiver, and that engineering controls enable the use of various aerogel geometries. Additionally, heat loss testing shows the impressive thermal insulating properties of the refractory aerogels. Compared to a receiver with no aerogels, the aerogel receiver decreases heat losses by ~30%. Numerical modeling confirms the validity of the experimental setup, and the edge losses in the receiver are estimated by using baseline tests with no insulation. By using the validated numerical modeling and a validated technoeconomic model, the levelized costs of electricity and heat of a next-gen CST plant, integrated with refractory aerogels, are estimated. The results of the TEA show that refractory aerogels enable the cheapest forms of carbon-neutral baseload electricity generation and high temperature process heat when paired with selective absorbers.

# Chapter 7 : Summary and Future Directions of Aerogels in CST

## 7.1 Conclusions

Silica aerogels present an alternative design for linear receivers and have the potential to supply inexpensive baseload electricity generation or high temperature heat. Current solutions to decarbonize electricity generation and industrial heating are limited by their costs or additional engineering constraints. Traditional solar PV and wind require concurrent energy storage. CST converts sunlight directly to high temperature heat, which makes it an appealing option to decarbonize industrial processes, and since thermal energy storage is fundamental to CST designs, they are inherently capable of providing baseload power.

Silica aerogels are a promising technology to enable higher temperatures and efficiencies in modular, linear CST receiver designs, but suffer from low selectivity and thermal stability. This thesis explored solutions to these two issues through the plasmon-enhanced greenhouse effect (PEGS) and thermally stabilized refractory aerogels. **Chapter 6** shows that when these two techniques are ideally combined, the result is a multicomponent aerogel capable of providing baseload electricity more cheaply than the current state-of-the-art, solar PV with battery storage.

## 7.2 Improvements in the PEGS Mechanism

As shown in **subchapter 3.4** Future Directions, the experimental demonstration of the PEGS mechanism is far lower than it should have been due to the lower-than-expected solar transmittance of the plasmonic aerogels. I theorize that the low transmittance is due to the agglomeration of nanoparticles within the aerogel matrix. It is widely known that the pH of a solution affects the agglomeration of nanoparticles,[109]

so it is expected that the aerogel reaction mixture, which contains ammonia, would affect this. One possible solution to this issue is to use nanoparticles with more chemically stable surfactants. Another solution is to increase the amount of ammonia catalyst in the aerogel reaction mixture. Although this may increase agglomeration, it also increases the reaction rate and decreases gelation time. If the amount of ammonia used gelates the aerogels within a matter of seconds, this may be fast enough to prevent significant agglomeration of the plasmonic nanoparticles.

Another avenue for improvement is the use of smaller plasmonic nanoparticles. Since scattering is the dominant attenuation mode for the particles in the solar spectrum, and scattering is primarily a function of particle size, then decreasing particle size could lead to improved solar transmittance, and improved performance.

## 7.3 Improvements in Refractory Aerogels

Although the refractory aerogels demonstrated impressive enhancements in the thermal stability of silica aerogels, given enough time, the refractory aerogels will likely densify to the same level as a native silica aerogel. To further stabilize aerogels, more thermally stable ALD coatings should be considered, such as zirconia, hafnia, or magnesium oxide. If the more stable refractory oxides can be deposited conformally and uniformly on the silica aerogel, the thermal stability could be further increased.

## 7.4 Development of Curved Aerogels

One of the experimental limitations of the prototype linear receiver in **Chapter 6** is that the V-shaped receiver design was used. This likely led to increased heat losses since the area of the aerogel insulation was ~50% larger than what a curved aerogel would have. Synthesizing and drying aerogels in a curved shape remains a challenge. Aerogels tend to slightly shrink during supercritical drying, so the shape may be difficult to predict the shape of the aerogel after shrinking from supercritical drying and other processing. If the aerogels are successfully made curved, the heat losses should be about 25% lower because of the decrease in effective radius.

## 7.5 Optimized Tandem Selective Absorbers

The TEA in **Chapter 6** uses commercially available selective absorbers that are designed to be the most efficient when used on their own. However, when paired with aerogels, the properties are suboptimal. Aerogels suffer from large radiative losses within the infrared transparency window (3 – 5 μm). Thus, selective absorbers should have preferentially low emittance in that region, whereas low emittance at longer wavelengths is unnecessary due to the high absorption of aerogels at long wavelengths. Therefore, certain structures for selective absorbers, such as photonic crystals, may be able to selectively lower emission within a small band in the infrared, without aiming for low emittance broadly in the infrared. Lastly, high solar absorptance is always a priority with solar absorber coatings. The optimal properties for a tandem selective absorber are then: (i) high solar absorptance (>98%) and (ii) low thermal emittance between 3 – 5 μm.

# References


(1) Ardani, K.; Denholm, P.; Mai, T.; Margolis, R.; Silverman, T.; Zuboy, J. *Solar Futures Study*; 2021.

(2) Turchi, C. S.; Ma, Z.; Neises, T. W.; Wagner, M. J. Thermodynamic Study of Advanced Supercritical Carbon Dioxide Power Cycles for Concentrating Solar Power Systems. *J Sol Energy Eng* **2013**, *135* (4), 1–7.

(3) Mehos, M.; Turchi, C.; Vidal, J.; Wagner, M.; Ma, Z.; Ho, C.; Kolb, W.; Andraka, C.; Kruizenga, A. Concentrating Solar Power Gen3 Demonstration Roadmap. *Nrel/Tp-5500-67464* **2017**, No. January, 1–140.

(4) Landsberg, P. T.; Baruch, P. The Thermodynamics of the Conversion of Radiation Energy for Photovoltaics. *Journal of Physics A: General Physics* **1989**, *22* (11), 1911–1926. https://doi.org/10.1088/0305-4470/22/11/028.

(5) Seraphin, B. O. *Solar Energy Conversion: Solid-State Physics Aspects*; Springer: Berlin, 1979. https://doi.org/10.1007/3-540-09224-2_2.

(6) Trotter, D. M.; Sievers, A. J. Spectral Selectivity of High-Temperature Solar Absorbers II. Effects of Interface. *Appl Opt* **1980**, *19* (5).

(7) Svendsen, S. Solar Collector with Monolithic Silica Aerogel. *J Non Cryst Solids* **1992**, *145* (C), 240–243.

(8) Zhao, L.; Bhatia, B.; Yang, S.; Strobach, E.; Weinstein, L. A.; Cooper, T. A.; Chen, G.; Wang, E. N. Harnessing Heat beyond 200 °c from Unconcentrated Sunlight with Nonevacuated Transparent Aerogels. *ACS Nano* **2019**. https://doi.org/10.1021/acsnano.9b02976.

(9) Tsakiris, G. D.; Eidmann, K. An Approximate Method for Calculating Planck and Rosseland Mean Opacities in Hot, Dense Plasmas. *J Quant Spectrosc Radiat Transf* **1987**, *38* (5), 353–368. https://doi.org/10.1016/0022-4073(87)90030-6.

(10) Modest, M. F. *Radiative Heat Transfer*, 3rd ed.; Academic Press, Inc.: San Diego, 2013. https://doi.org/10.1016/B978-0-12-386944-9.50001-7.

(11) Rinnerbauer, V.; Lenert, A.; Bierman, D. M.; Yeng, Y. X.; Chan, W. R.; Geil, R. D.; Senkevich, J. J.; Joannopoulos, J. D.; Wang, E. N.; Soljačič, M.; Celanovic, I. Metallic Photonic Crystal Absorber-Emitter for Efficient Spectral Control in High-Temperature Solar Thermophotovoltaics. *Adv Energy Mater* **2014**, *4* (12), 1–10.

(12) Berquist, Z. J.; Gayle, A. J.; Dasgupta, N. P.; Lenert, A. Transparent Refractory Aerogels for Efficient Spectral Control in High-Temperature Solar Power Generation. *Adv Funct Mater* **2021**.

(13) Berquist, Z. J.; Turaczy, K. K.; Lenert, A. Plasmon-Enhanced Greenhouse Selectivity for High-Temperature Solar Thermal Energy Conversion. *ACS Nano* **2020**, *14* (10), 12605–12613.

(14) Cao, F.; Kraemer, D.; Sun, T.; Lan, Y.; Chen, G.; Ren, Z. Enhanced Thermal Stability of W-Ni-Al2O3 Cermet-Based Spectrally Selective Solar Absorbers with Tungsten Infrared Reflectors. *Adv Energy Mater* **2015**, *5* (2), 1–7. https://doi.org/10.1002/aenm.201401042.

(15) Cao, F.; Kraemer, D.; Tang, L.; Li, Y.; Litvinchuk, A. P.; Bao, J.; Chen, G.; Ren, Z. A High-Performance Spectrally-Selective Solar Absorber Based on a Yttria-Stabilized Zirconia Cermet with High-Temperature Stability. *Energy Environ Sci* **2015**, *8* (10), 3040–3048.

(16) Jyothi, J.; Chaliyawala, H.; Srinivas, G.; Nagaraja, H. S.; Barshilia, H. C. Design and Fabrication of Spectrally Selective TiAlC/TiAlCN/TiAlSiCN/TiAlSiCO/TiAlSiO Tandem Absorber for Higherolature Solar Thermal Power Applications. *Solar Energy Materials and Solar Cells* **2015**, *140*, 209–216.

(17) Wang, H.; Alshehri, H.; Su, H.; Wang, L. Design, Fabrication and Optical Characterizations of Large-Area Lithography-Free Ultrathin Multilayer Selective Solar Coatings with Excellent Thermal Stability in Air. *Solar Energy Materials and Solar Cells* **2018**, *174* (June 2017), 445–452.

(18) Wanqing Cao; Hunt, A. J. Improving the Visible Transparency of Silica Aerogels. *J Non Cryst Solids* **1994**, *176* (1), 18–25. https://doi.org/10.1016/0022-3093(94)90206-2.

(19) Wang, P.; Körner, W.; Emmerling, A.; Beck, A.; Kuhn, J.; Fricke, J. Optical Investigations of Silica Aerogels. *J Non Cryst Solids* **1992**, *145* (C), 141–145. https://doi.org/10.1016/S0022-3093(05)80444-2.

(20) Emmerling, A.; Petricevic, R.; Beck, A.; Wang, P.; Scheller, H.; Fricke, J. Relationship between Optical Transparency and Nanostructural Features of Silica Aerogels. *J Non Cryst Solids* **1995**, *185* (3), 240–248. https://doi.org/10.1016/0022-3093(95)00021-6.

(21) Tillotson, T. M.; Hrubesh, L. W. Transparent Ultralow-Density Silica Aerogels Prepared by a Two-Step Sol-Gel Process. *J Non Cryst Solids* **1992**, *145* (C), 44–50.

(22) Strobach, E.; Bhatia, B.; Yang, S.; Zhao, L.; Wang, E. N. High Temperature Annealing for Structural Optimization of Silica Aerogels in Solar Thermal Applications. *J Non Cryst Solids* **2017**, *462*, 72–77.

(23) Henning, S.; Svensson, L. Production of Silica Aerogel. *Phys Scr* **1981**, *23* (4), 697–702. https://doi.org/10.1088/0031-8949/23/4B/018.

(24) Beck, A.; Caps, R.; Fricke, J. Scattering of Visible Light from Silica Aerogels. *J Phys D Appl Phys* **1989**, *22* (6), 730–734. https://doi.org/10.1088/0022-3727/22/6/002.

(25) Curcio, J. A.; Petty, C. C. The Near Infrared Absorption Spectrum of Liquid Water. *J Opt Soc Am* **1951**, *41* (5), 302–304.

(26) Bush, S. G.; Jorgenson, J. W.; Miller, M. L.; Linton, R. W. Transmission Near-Infrared Technique for Evaluation and Relative Quantitation of Surface Groups on Silica. *J Chromatogr A* **1983**, *260* (C), 1–12. https://doi.org/10.1016/0021-9673(83)80001-6.

(27) Jeong, A. Y.; Koo, S. M.; Kim, D. P. Characterization of Hydrophobic SiO2 Powders Prepared by Surface Modification on Wet Gel. *J Solgel Sci Technol* **2000**, *19* (1–3), 483–487. https://doi.org/10.1023/A:1008716017567.

(28) Rao, A. P.; Rao, A. V.; Pajonk, G. M. Hydrophobic and Physical Properties of the Two Step Processed Ambient Pressure Dried Silica Aerogels with Various Exchanging Solvents. *J Solgel Sci Technol* **2005**, *36* (3), 285–292. https://doi.org/10.1007/s10971-005-4662-1.

(29) Venkateswara Rao, A.; Kulkarni, M. M.; Amalnerkar, D. P.; Seth, T. Surface Chemical Modification of Silica Aerogels Using Various Alkyl-Alkoxy/Chloro Silanes. *Appl Surf Sci* **2003**, *206* (1–4), 262–270.

(30) Malfait, W. J.; Zhao, S.; Verel, R.; Iswar, S.; Rentsch, D.; Fener, R.; Zhang, Y.; Milow, B.; Koebel, M. M. Surface Chemistry of Hydrophobic Silica Aerogels. *Chemistry of Materials* **2015**, *27* (19), 6737–6745. https://doi.org/10.1021/acs.chemmater.5b02801.

(31) Venkateswara Rao, A.; Bhagat, S. D.; Hirashima, H.; Pajonk, G. M. Synthesis of Flexible Silica Aerogels Using Methyltrimethoxysilane (MTMS) Precursor. *J Colloid Interface Sci* **2006**, *300* (1), 279–285. https://doi.org/10.1016/j.jcis.2006.03.044.

(32) Du, M.; Mao, N.; Russell, S. J. Control of Porous Structure in Flexible Silicone Aerogels Produced from Methyltrimethoxysilane (MTMS): The Effect of Precursor Concentration in Sol–Gel Solutions. *J Mater Sci* **2016**, *51* (2), 719–731. https://doi.org/10.1007/s10853-015-9378-1.

(33) Aegerter, M.; Leventis, N.; Koebel, M. Aerogels Handbook (Advances in Sol-Gel Derived Materials and Technologies). In *Springer*; 2011; p 932.

(34) Li, W.; Willey, R. J. Stability of Hydroxyl and Methoxy Surface Groups on Silica Aerogels. *J Non Cryst Solids* **1997**, *212* (2–3), 243–249. https://doi.org/10.1016/S0022-3093(97)00021-5.

(35) Cui, S.; Liu, Y.; Fan, M. H.; Cooper, A. T.; Lin, B. L.; Liu, X. Y.; Han, G. F.; Shen, X. D. Temperature Dependent Microstructure of MTES Modified Hydrophobic Silica Aerogels. *Mater Lett* **2011**, *65* (4), 606–609. https://doi.org/10.1016/j.matlet.2010.11.026.

(36) Strobach, E.; Bhatia, B.; Yang, S.; Zhao, L.; Wang, E. N. High Temperature Stability of Transparent Silica Aerogels for Solar Thermal Applications. *APL Mater* **2019**, *7* (8). https://doi.org/10.1063/1.5109433.

(37) Zeng, S. Q.; Hunt, A.; Greif, R. Geometric Structure and Thermal Conductivity of Porous Medium Silica Aerogel. *J Heat Transfer* **1995**, *117* (4), 1055–1058. https://doi.org/10.1115/1.2836281.

(38) Wei, G.; Zhang, X.; Yu, F. Effective Thermal Conductivity Analysis of Xonotlite-Aerogel Composite Insulation Material. *Journal of Thermal Science* **2009**, *18* (2), 142–149. https://doi.org/10.1007/s11630-009-0142-1.

(39) Wei, G.; Liu, Y.; Zhang, X.; Yu, F.; Du, X. Thermal Conductivities Study on Silica Aerogel and Its Composite Insulation Materials. *Int J Heat Mass Transf* **2011**, *54* (11–12), 2355–2366.

(40) Dan, D.; Zhang, H.; Tao, W. Q. Effective Structure of Aerogels and Decomposed Contributions of Its Thermal Conductivity. *Appl Therm Eng* **2014**, *72* (1), 2–9.

(41) Bi, C.; Tang, G. H. Effective Thermal Conductivity of the Solid Backbone of Aerogel. *Int J Heat Mass Transf* **2013**, *64*, 452–456. https://doi.org/10.1016/j.ijheatmasstransfer.2013.04.053.

(42) Zhu, C. Y.; Li, Z. Y. Modeling of the Apparent Solid Thermal Conductivity of Aerogel. *Int J Heat Mass Transf* **2018**, *120*, 724–730. https://doi.org/10.1016/j.ijheatmasstransfer.2017.12.076.

(43) Vacher, R.; Woignier, T.; Pelous, J. Structure and Self-Similarity of Silica Aerogels. *Physical Revew B* **1988**, *37* (11), 6500–6503.

(44) Dai, Y. J.; Tang, Y. Q.; Fang, W. Z.; Zhang, H.; Tao, W. Q. A Theoretical Model for the Effective Thermal Conductivity of Silica Aerogel Composites. *Appl Therm Eng* **2018**, *128*, 1634–1645. https://doi.org/10.1016/j.applthermaleng.2017.09.010.

(45) Xie, T.; He, Y. L.; Hu, Z. J. Theoretical Study on Thermal Conductivities of Silica Aerogel Composite Insulating Material. *Int J Heat Mass Transf* **2013**, *58* (1–2), 540–552. https://doi.org/10.1016/j.ijheatmasstransfer.2012.11.016.

(46) Wang, J.; Kuhn, J.; Lu, X. Monolithic Silica Aerogel Insulation Doped with TiO2 Powder and Ceramic Fibers. *J Non Cryst Solids* **1995**, *186* (95), 296–300. https://doi.org/10.1016/0022-3093(95)00068-2.

(47) Kwon, Y.; Choi, S. Ambient-Dried Silica Aerogel Doped with TiO2. *J Mater Sci* **2000**, *35*, 6075–6079.

(48) Kuhn, J.; Gleissner, T.; Arduini-Schuster, M. C.; Korder, S.; Fricke, J. Integration of Mineral Powders into SiO2 Aerogels. *J Non Cryst Solids* **1995**, *186*, 291–295. https://doi.org/10.1016/0022-3093(95)00067-4.

(49) Hümmer, E.; Lu, X.; Rettelbach, T.; Fricke, J. Heat Transfer in Opacified Aerogel Powders. *J Non Cryst Solids* **1992**, *145* (C), 211–216. https://doi.org/10.1016/S0022-3093(05)80458-2.

(50) Lu, X.; Wang, P.; Arduini-Schuster, M. C.; Kuhn, J.; Büttner, D.; Nilsson, O.; Heinemann, U.; Fricke, J. Thermal Transport in Organic and Opacified Silica Monolithic Aerogels. *J Non Cryst Solids* **1992**, *145* (C), 207–210. https://doi.org/10.1016/S0022-3093(05)80457-0.

(51) Zeng, S. Q.; Hunt, A.; Greif, R. Theoretical Modeling of Carbon Content to Minimize Heat Transfer in Silica Aerogel. **1995**, *186*, 271–277.

(52) Lee, D.; Stevens, P. C.; Zeng, S. Q.; Hunt, A. J. Thermal Characterization of Carbon-Opacified Silica Aerogels. *J Non Cryst Solids* **1995**, *186*, 285–290. https://doi.org/10.1016/0022-3093(95)00055-0.

(53) Jeffrey Brinker, C.; Scherer, G. W. Sintering. In *Sol-Gel Science*; Academic Press, Inc.: San Diego, CA, 1990; pp 675–742. https://doi.org/10.1016/B978-0-08-057103-4.50016-7.

(54) Scherer, G. W.; Luong, J. C. GLASSES FROM COLLOIDS. *J Non Cryst Solids* **1984**, *63*, 163–172.

(55) Gallo, T. A.; Klein, L. C. Apparent Viscosity of Sol-Gel Processed Silica. *J Non Cryst Solids* **1986**, *82* (1), 198–204. https://doi.org/10.1016/0022-3093(86)90131-6.

(56) Roy, R. A.; Roy, R. Diphasic Xerogels: I. Ceramic-Metal Composites. *Mater Res Bull* **1984**, *19*, 169–177.

(57) Sacks, M. D.; Bozkurt, N.; Scheiffele, G. W. Fabrication of Mullite and Mullite-Matrix Composites by Transient Sintering of Composite Powders. *Journal of the American Ceramic Society* **1991**, *74* (10), 2428–2437.

(58) Komarneni, S.; Suwa, Y.; Roy, R. Application of Compositionally Diphasic Xerogels for Enhanced Densification: The System Al2O3-SiO2. *Journal of the American Ceramic Society* **1986**, *69* (7), C-155-C-156.

(59) Cluzel, F.; Larnac, G.; Phalippou, J. Structure and Thermal Evolution of Mullite Aerogels. *J Mater Sci* **1991**, *26*, 5979–5984.

(60) Komarneni, S.; Roy, R.; Selvaraj, U.; Malla, P. B.; Breval, E. Nanocomposite Aerogels: The $SiO_2$–$Al_2O_3$ System. *J Mater Res* **1993**, *8* (12), 3163–3167.

(61) Heinrich, T.; Tappert, W.; Lenhard, W.; Fricke, J. Synthesis and Properties of Mullite and Cordierite Aerogels. *J Solgel Sci Technol* **1994**, *2*, 921–924.

(62) Saliger, R.; Heinrich, T.; Gleissner, T.; Fricke, J. Sintering Behaviour of Alumina-Modified Silica Aerogels. *J Non Cryst Solids* **1995**, *186*, 113–117.

(63) Himmel, B.; Gerber, T.; Bürger, H.; Holzhüter, G.; Olbertz, A. Structural Characterization of SiO2-Al2O3 Aerogels. *J Non Cryst Solids* **1995**, *186*, 149–158. https://doi.org/10.1016/0022-3093(95)00045-3.

(64) Aravind, P. R.; Mukundan, P.; Krishna Pillai, P.; Warrier, K. G. K. Mesoporous Silica-Alumina Aerogels with High Thermal Pore Stability through Hybrid Sol-Gel Route Followed by Subcritical Drying. *Microporous and Mesoporous Materials* **2006**, *96* (1–3), 14–20. https://doi.org/10.1016/j.micromeso.2006.06.014.

(65) Hrubesh, L. W. Aerogel Applications. *J Non Cryst Solids* **1998**, *225*, 335–342.

(66) Kucheyev, S. O.; Biener, J.; Wang, Y. M.; Baumann, T. F.; Wu, K. J.; Van Buuren, T.; Hamza, A. V.; Satcher, J. H.; Elam, J. W.; Pellin, M. J. Atomic Layer Deposition of ZnO on Ultralow-Density Nanoporous Silica Aerogel Monoliths. *Appl Phys Lett* **2005**, *86* (8), 1–3.

(67) Baumann, T. F.; Biener, J.; Wang, Y. M.; Kucheyev, S. O.; Nelson, E. J.; Satcher, J. H.; Elam, J. W.; Pellin, M. J.; Hamza, A. V; Systems, E.; Di, V.; Re, V.; Recei, M.; October, V. Atomic Layer Deposition of Uniform Metal Coatings on Highly Porous Aerogel Substrates. *Chemistry of Materials* **2006**, *18* (26), 6106–6108.

(68) Elam, J. W.; Xiong, G.; Han, C. Y.; Wang, H. H.; Birrell, J. P.; Welp, U.; Hryn, J. N.; Pellin, M. J.; Baumann, T. F.; Poco, J. F.; Jr, J. H. S. Atomic Layer Deposition for the Conformal Coating of Nanoporous Materials. *J Nanomater* **2006**, *2006*, 1–5. https://doi.org/10.1155/JNM/2006/64501.

(69) Ghosal, S.; Baumann, T. F.; King, J. S.; Kucheyev, S. O.; WAng, Y.; Worsley, M. A.; Biener, J.; Bent, S. F.; Hamza, A. v. Controlling Atomic Layer Deposition of TiO2 in Aerogels through Surface Functionalization. *Chemistry of Materials* **2009**, *21* (9), 1989–1992.

(70) Elam, J. W.; Libera, J. A.; Huynh, T. H.; Feng, H.; Pellin, M. J. Atomic Layer Deposition of Aluminum Oxide in Mesoporous Silica Gel. *Journal of Physical Chemistry C* **2010**, *114* (41), 17286–17292.

(71) Mane, A. U.; Greene, J. P.; Nolen, J. A.; Sampathkumaran, U.; Owen, T. W.; Winter, R.; Elam, J. W. Refractory Nanoporous Materials Fabricated Using Tungsten Atomic Layer Deposition on Silica Aerogels. *Appl Surf Sci* **2012**, *258* (17), 6472–6478. https://doi.org/10.1016/j.apsusc.2012.03.063.

(72) Emmerling, A.; Gross, J.; Gerlach, R.; Goswin, R.; Reichenauer, G.; Fricke, J.; Haubold, H. G. Isothermal Sintering of SiO2-Aerogels. *J Non Cryst Solids* **1990**, *125* (3), 230–243. https://doi.org/10.1016/0022-3093(90)90853-E.

(73) Maleki, H.; Durães, L.; Portugal, A. An Overview on Silica Aerogels Synthesis and Different Mechanical Reinforcing Strategies. *J Non Cryst Solids* **2014**, *385*, 55–74. https://doi.org/10.1016/j.jnoncrysol.2013.10.017.

(74) Gayle, A. J.; Berquist, Z. J.; Chen, Y.; Hill, A. J.; Hoffman, J. Y.; Ashley, R.; Lenert, A.; Dasgupta, N. P. Tunable Atomic Layer Deposition into Ultra-High-Aspect-Ratio ( > 60 , 000 : 1 ) Aerogel Monoliths Enabled by Transport Modeling. *Chemistry of Materials* **2021**, No. 33. https://doi.org/10.1021/acs.chemmater.1c00770.

(75) ASTM Standard C71-12, 2021, " Standard Terminology Relating to Refractories, " ASTM International, West Conshohocken, PA, 2021. **2021**, 2021.

(76) Guler, U.; Boltasseva, A.; Shalaev, V. M. Refractory Plasmonics. *Science (1979)* **2014**, *344* (6181), 263–264.

(77) Dasgupta, N. P.; Mack, J. F.; Langston, M. C.; Bousetta, A.; Prinz, F. B. Design of an Atomic Layer Deposition Reactor for Hydrogen Sulfide Compatibility. *Review of Scientific Instruments* **2010**, *81* (4), 044102. https://doi.org/10.1063/1.3384349.

(78) Yang, S.; Strobach, E.; Bierman, D.; Zhao, L.; Bhatia, B.; Wang, E. N. Effect of Al2O3 ALD Coating on Thermal Stability of Silica Aerogel. *Journal of Porous Materials* **2021**, *i* (September). https://doi.org/10.1007/s10934-021-01155-4.

(79) Stoch, J.; Lercher, J.; Ceckiewicz, S. Correlations between XPS Binding Energies and Composition of Aluminasilicate and Phosphate Molecular Sieves. *Zeolites* **1992**, *12* (1), 81–85. https://doi.org/10.1016/0144-2449(92)90015-H.

(80) Sandupatla, A. S.; Alexopoulos, K.; Reyniers, M. F.; Marin, G. B. DFT Investigation into Alumina ALD Growth Inhibition on Hydroxylated Amorphous Silica Surface. *Journal of Physical Chemistry C* **2015**, *119* (32), 18380–18388. https://doi.org/10.1021/acs.jpcc.5b05261.

(81) Cai, H.; Jiang, Y.; Feng, J.; Chen, Q.; Zhang, S.; Li, L.; Feng, J. Nanostructure Evolution of Silica Aerogels under Rapid Heating from 600 °C to 1300 °C via In-Situ TEM Observation. *Ceram Int* **2020**, *46* (8), 12489–12498.

(82) Zu, G.; Shen, J.; Wang, W.; Zou, L.; Lian, Y.; Zhang, Z.; Liu, B.; Zhang, F. Robust, Highly Thermally Stable, Core-Shell Nanostructured Metal Oxide Aerogels as High-Temperature Thermal Superinsulators, Adsorbents, and Catalysts. *Chemistry of Materials* **2014**, *26* (19), 5761–5772. https://doi.org/10.1021/cm502886t.

(83) Brinker, C. J.; Scherer, G. W. *Sol-Gel Science*; Academic Press, Inc.: San Diego, CA, 1990. https://doi.org/10.1016/b978-0-08-057103-4.50006-4.

(84) Oneill, B. J.; Jackson, D. H. K.; Lee, J.; Canlas, C.; Stair, P. C.; Marshall, C. L.; Elam, J. W.; Kuech, T. F.; Dumesic, J. A.; Huber, G. W. Catalyst Design with Atomic Layer Deposition. *ACS Catal* **2015**, *5* (3), 1804–1825. https://doi.org/10.1021/cs501862h.

(85) Digne, M.; Sautet, P.; Raybaud, P.; Euzen, P.; Toulhoat, H. Hydroxyl Groups on γ-Alumina Surfaces: A DFT Study. *J Catal* **2002**, *211* (1), 1–5. https://doi.org/10.1006/jcat.2002.3741.

(86) Digne, M.; Sautet, P.; Raybaud, P.; Euzen, P.; Toulhoat, H. Use of DFT to Achieve a Rational Understanding of Acid-Basic Properties of γ-Alumina Surfaces. *J Catal* **2004**, *226* (1), 54–68. https://doi.org/10.1016/j.jcat.2004.04.020.

(87) Petrik, N. G.; Huestis, P. L.; Laverne, J. A.; Aleksandrov, A. B.; Orlando, T. M.; Kimmel, G. A. Molecular Water Adsorption and Reactions on α-Al2O3(0001) and α-Alumina Particles. *Journal of Physical Chemistry C* **2018**, *122* (17), 9540–9551. https://doi.org/10.1021/acs.jpcc.8b01969.

(88) Li, Y.; Chen, L.; Wooding, J. P.; Zhang, F.; Lively, R. P.; Ramprasad, R.; Losego, M. D. Controlling Wettability, Wet Strength, and Fluid Transport Selectivity of Nanopaper with Atomic Layer Deposited (ALD) Sub-Nanometer Metal Oxide Coatings. *Nanoscale Adv* **2020**, *2* (1), 356–367. https://doi.org/10.1039/c9na00417c.

(89) Echániz, T.; Setién-Fernández, I.; Pérez-Sáez, R. B.; Prieto, C.; Galindo, R. E.; Tello, M. J. Importance of the Spectral Emissivity Measurements at Working Temperature to Determine the Efficiency of a Solar Selective Coating. *Solar Energy Materials and Solar Cells* **2015**, *140*, 249–252.

(90) Selvakumar, N.; Manikandanath, N. T.; Biswas, A.; Barshilia, H. C. Design and Fabrication of Highly Thermally Stable HfMoN/HfON/Al2O3 Tandem Absorber for Solar Thermal Power Generation Applications. *Solar Energy Materials and Solar Cells* **2012**, *102*, 86–92.

(91) Feng, J.; Zhang, S.; Liu, X.; Yu, H.; Ding, H.; Tian, Y.; Ouyang, J. Solar Selective Absorbing Coatings TiN/TiSiN/SiN Prepared on Stainless Steel Substrates. *Vacuum* **2015**, *121*, 135–141.

(92) Nuru, Z. Y.; Kotsedi, L.; Arendse, C. J.; Motaung, D.; Mwakikunga, B.; Roro, K.; Maaza, M. Thermal Stability of Multilayered Pt-Al2O3 Nanocoatings for High Temperature CSP Systems. *Vacuum* **2015**, *120*, 115–120.

(93) Cao, F.; Tang, L.; Li, Y.; Litvinchuk, A. P.; Bao, J.; Ren, Z. A High-Temperature Stable Spectrally-Selective Solar Absorber Based on Cermet of Titanium Nitride in SiO2 Deposited on Lanthanum Aluminate. *Solar Energy Materials and Solar Cells* **2017**, *160* (September 2016), 12–17.

(94) Bilokur, M.; Gentle, A. R.; Arnold, M. D.; Cortie, M. B.; Smith, G. B. High Temperature Optically Stable Spectrally-Selective Ti1-XAlxN-Based Multilayer Coating for Concentrated Solar Thermal Applications. *Solar Energy Materials and Solar Cells* **2019**, *200* (March), 109964.

(95) Zhao, L.; Bhatia, B.; Yang, S.; Strobach, E.; Weinstein, L. A.; Cooper, T. A.; Chen, G.; Wang, E. N. Harnessing Heat beyond 200 °c from Unconcentrated Sunlight with Nonevacuated Transparent Aerogels. *ACS Nano* **2019**, *13* (7), 7508–7516. https://doi.org/10.1021/acsnano.9b02976.

(96) Yoshimaru, M.; Koizumi, S.; Shimokawa, K. Structure of Fluorine-Doped Silicon Oxide Films Deposited by Plasma-Enhanced Chemical Vapor Deposition. *Journal of Vacuum Science & Technology A: Vacuum, Surfaces, and Films* **1997**, *15* (6), 2908–2914. https://doi.org/10.1116/1.580884.

(97) Zhang, K.; Hao, L.; Du, M.; Mi, J.; Wang, J.; Meng, J. A Review on Thermal Stability and High Temperature Induced Ageing Mechanisms of Solar Absorber Coatings. *Renewable and Sustainable Energy Reviews* **2017**, *67*, 1282–1299.

(98) Xu, K.; Du, M.; Hao, L.; Mi, J.; Yu, Q.; Li, S. A Review of High-Temperature Selective Absorbing Coatings for Solar Thermal Applications. *Journal of Materiomics* **2020**, *6* (1), 167–182.

(99) Nordgaard, A.; Beckman, W. A. Modelling of Flat-Plate Collectors Based on Monolithic Silica Aerogel. *Solar Energy* **1992**, *49* (5), 387–402.

(100) Li, Q.; Zhang, Y.; Wen, Z. X.; Qiu, Y. An Evacuated Receiver Partially Insulated by a Solar Transparent Aerogel for Parabolic Trough Collector. *Energy Convers Manag* **2020**, *214* (January), 112911.

(101) Qiu, Y.; Zhang, Y.; Li, Q.; Xu, Y.; Wen, Z. X. A Novel Parabolic Trough Receiver Enhanced by Integrating a Transparent Aerogel and Wing-like Mirrors. *Appl Energy* **2020**, *279* (September), 115810.

(102) Inc., N. T. *Design and Field Test of Manufacturable Advanced Low-Cost Receiver for Parabolic Trough Solar Power*; 2018.

(103) Kincaid, N.; Mungas, G.; Kramer, N.; Wagner, M.; Zhu, G. An Optical Performance Comparison of Three Concentrating Solar Power Collector Designs in Linear Fresnel, Parabolic Trough, and Central Receiver. *Appl Energy* **2018**, *231* (June), 1109–1121.

(104) Wang, X.; Lee, E.; Xu, C.; Liu, J. High-Efficiency, Air-Stable Manganese–Iron Oxide Nanoparticle-Pigmented Solar Selective Absorber Coatings toward Concentrating Solar Power Systems Operating at 750 °C. *Mater Today Energy* **2021**, *19*.

(105) *Sunshot Vision Study*; 2012.

(106) Henry, A.; Prasher, R. The Prospect of High Temperature Solid State Energy Conversion to Reduce the Cost of Concentrated Solar Power. *Energy Environ Sci* **2014**, *7* (6), 1819–1828. https://doi.org/10.1039/c4ee00288a.

(107) Turchi, C. S.; Boyd, M.; Kesseli, D.; Kurup, P.; Mehos, M.; Neises, T.; Sharan, P.; Wagner, M. J.; Wendelin, T. CSP Systems Analysis - Final Project. *Nrel/TP-5500-72856* **2019**, No. May.

(108) SunShot Vision Study: February 2012 (Book). **2012**. https://doi.org/10.2172/1039075.

(109) Al-Gebory, L.; Mengüç, M. P. The Effect of PH on Particle Agglomeration and Optical Properties of Nanoparticle Suspensions. *J Quant Spectrosc Radiat Transf* **2018**, *219*, 46–60. https://doi.org/10.1016/j.jqsrt.2018.07.020.